UNIVERSITEIT VAN PRETORIA
UNIVERSITY OF PRETORIA
YUNIBESITHI YA PRETORIA

COMPUTATIONAL ANALYSIS OF SURFACE TENSION EFFECTS IN MICROCHANNEL FLOW BOILING WITH SELF-REWETTING FLUIDS

By

André Pienaar

Submitted in partial fulfilment of the requirements for the degree of

Master of Engineering (Mechanical Engineering)

In the

Department of Mechanical and Aeronautical Engineering

Faculty of Engineering, Built Environment and Information Technology

UNIVERSITY OF PRETORIA

Supervisor: Professor Jaco Dirker

Co-supervisors: Professor Prashant Valluri

2024

PLAGIARISM DECLARATION

Full names	André Pienaar
Student number	U17028940
Topic of work	Computational Analysis of Surface Tension Effects in Microchannel Flow Boiling with Self-Rewetting Fluids

Declaration

1. I understand what plagiarism is and am aware of the University's policy in this regard.
2. I declare that this dissertation (e.g., essay, report, project, assignment, dissertation, thesis, etc.) is my own original work. Where other people's work has been used (either from a printed source, internet or any other source), this has been properly acknowledged and referenced in accordance with the requirements as stated in the University's plagiarism prevention policy.
3. I have not used another student's past written work to hand in as my own.
4. I have not allowed, and will not allow, anyone to copy my work with the intention of passing it off as his or her own work.

Signature 

ACKNOWLEDGMENTS

I would like to thank the ThermaSMART project funded by the European Commission (778104 – ThermaSMART – H2020MSCA-RISE-2017), the University of Pretoria, and the University of Edinburgh for this once in a lifetime opportunity. It has provided me with knowledge and experiences that I would not have gained if it was not for this opportunity and that I will never forget.

I would like to thank Dr Marilize Everts, Dr Miriam Lloyd, Tersia Evans, and Jackie Gordan for all their help with the administrative work in making this project possible and for helping me get settled in Edinburgh.

I would like to thank the University of Edinburgh for allowing me to use their personal computers as well as their high-performance cluster (Eddie) to run many of the necessary numerical simulations. I would also like to thank the CHPC for giving me access to their high-performance cluster to run majority of my numerical simulations. Without either of these necessities, the simulations would not have been possible.

Thank you to Mandi Venter for the valuable experimental work you conducted on the self-rewetting fluids. Thank you also for all the assistance you provided me and for the kindness you showed me.

To Prof. Prashant Valluri, thank you for all the support, knowledge, and patience you gave me throughout this journey. Thank you especially for welcoming me into your research group and for making my time in Edinburgh the best I could ask for.

To Prof. Jaco Dirker, thank you for your continued support throughout this journey. Your advice, knowledge, and constant motivation were more than I could have ever asked for. You have given me an experience that I will forever treasure. Thank you also for never giving up on me, especially near the closing portions of this dissertation.

To my mother Linette, father Eddie, and sister Leandra; I would like to thank you for all your love and support. Even while we were all in different parts of the world, your constant support never failed. Thank you for all that you have done for me. Thank you for giving me the opportunity to start a Master's and the ability to complete it.

Lastly, thank you to my loving girlfriend Emily for all your love and support. Thank you for your constant motivation and belief in me. You were by my side every step of this journey and without you, it would have been a lot more challenging and a lot less enjoyable.

ABSTRACT

Continual developments in computing technologies have caused processors and micro-processors to reduce in size while at the same time, operating at higher power densities and increased heat flux demands. Current cooling methods are quickly becoming less effective as they struggle to remove heat at the required rates. Microchannel flow boiling is at the forefront for cooling of high heat flux applications due to its combined convection heat transfer and latent heat transfer mechanisms. However, innovation for flow boiling in microchannels is needed to keep up with the continual developments, particularly because the typical coolant fluids often tend to experience local dry-out regions. There exists a class of fluids, known as self-rewetting fluids (SRF), which possess unique surface tension characteristics that reduce the local dry-out regions. This reduction in local dry-out regions is caused by the fluid motion at the two-phase interface being driven by surface tension gradients as described by the Marangoni effect. Limited information is available to study this phenomenon and therefore any additional information regarding the heat transfer capabilities and fluid dynamics of these fluids is crucial.

In this numerical investigation, a 5% v/v 1-butanol-water solution was used as the SRF and studied in a thin horizontal channel at different heat fluxes. This was achieved by conducting two-dimensional (2D) simulations using a domain with a length of 5 mm and a height of 0.3 mm for various applied heat fluxes and an inlet mass flux of 15 kg/m²s. The numerical study investigated the flow of vapour slugs in the channel without the influence of surface wettability by not modelling any contact between vapour slugs and the wall. The results from the SRF were compared to those of water. It was found that the SRF, which has a unique surface tension gradient profile, drew the fluid surrounding the two-phase interface into the hotter region between the heated wall and the vapour slug. The water on the other hand experienced fluid being drawn out of this heated region resulting in thinner liquid films. The difference in the liquid films meant that the hotter fluid near the heated wall was evaporated in the case of water whereas it was trapped in the case of the SRF.

Due to the hotter fluid being trapped in the SRF, higher surface temperatures were recorded than in the water case. The higher surface temperatures resulted in the SRF having lower heat transfer coefficients than the water. These results were observed at all the applied heat fluxes. Interestingly, these results are opposite to what was experienced in a similar study with a 0.2wt% heptanol-water mixture as the SRF, where surface wettability was a factor. Here surface wettability refers to the vapour bubble contacting the heated surface, such as during bubble departure, which was not modelled in the current study, instead the bubble was initialised in the fluid stream. The dry-out regions formed were smaller in the case of the SRF than in the water, which caused lower heat transfer coefficients in the water due to the poor heat transfer of vapour. On the other hand, an experimental investigation of the 5% v/v 1-butanol-water mixture as the SRF yielded similar results to the current numerical study in that the SRF experienced lower heat transfer coefficients to the water for a mass flux of G = 15 kg/m^{2}s.

The numerical study observed that in the case of slug flow where surface wettability and surface dry-out is not relevant, and where a mass flux of G = 15 kg/m^{2}s is used, the self-rewetting fluid does not provide any clear heat transfer benefits over pure fluids like water.

The current work was presented at the following conferences:

- The 4th ThermaSMART Workshop titled: "Thermal Management for Net-Zero: Sustainability in Earth and Space Environments". The workshop was hosted by the University of Pretoria from the 10th – 11th August 2023 at Lagoon Beach Conference Centre in Cape Town, South Africa. The work was presented by Mr André Pienaar.
- The 76th Annual Meeting of the Division of Fluid Dynamics by the American Physical Society (APS/DFD). The APS/DFD meeting was held at the Washington Convention Center in Washington DC, United States of America from the 19th – 21st November 2023. The work was presented by Mr André Pienaar.

TABLE OF CONTENTS

LIST OF FIGURES

LIST OF TABLES

NOMENCLATURE

Please note that (-) in the Unit column indicates a dimensionless parameter.

List of Symbols

Symbol	Description	Unit
A	Area	m²
A_c	Cross-sectional Area	m²
A_{int}	Interfacial area	-
A_s	Surface Area	m²
AR	Aspect Ratio	-
a	Exponential coefficient	-
Bo	Bond number	-
b	Bubble growth rate (Exponential coefficient)	-
Co	Confinement number	-
C	Polynomial coefficients	-
c_p	Specific heat	kJ/kg.K
D	Diffusion constant	various
D_h	Hydraulic diameter	m
d	Diameter	m
$Eö$	Eötvös number	-
e	Error	-
F_{back}	Backward evaporation momentum	N
$F_{forward}$	Forward liquid inertia force	N
f	Adaption metric	-
G	Mass flux	kg/m².s
g	Gravitational constant	m/s²
H	Height	m
h_{lv}	Latent heat of vaporization	J/kg
k	Thermal conductivity	W/m.K
L	Length	m
L_h	Heated length	m
La	Laplace constant	-
M	Molar mass	kg/mol
m	Mass	kg
$\dot{m}$	Mass flow rate	kg/s
N	Normalization factor	-
n	Number of moles	Mol
p	Wetted perimeter	m
R	Instability parameter	-
Re	Reynolds number	-
r	Gradient volume weight	-
S_m	Mass source term	-
S_e	Energy source term	-
T	Temperature	K
t	Time	s
t_w	Wall thickness	m

$\dot{Q}$	Heat transfer rate	W
$\dot{q}$	Heat flux	kW/m²
U	Free-stream velocity	m/s
u	Velocity	m/s
V	Volume	m³
W	Width	m
x	Coordinate	m
y	Coordinate	m
z	Coordinate	m

List of Greek Symbols

Symbol	Description	Unit
α	Convection heat transfer coefficient	W/m².K
β	Inclination angle	°
δ	Film thickness	m
Δx	Incremental distance	m
η	Molar fraction	-
γ	Mass transfer coefficient	-
κ	Interface curvature	1/m
μ	Dynamic viscosity	kg/m.s
ω	Accommodation factor	-
Ω	Local computation flow domain	-
ϕ	User-defined scalar	-
φ	Volume Fraction	-
π	Pi constant	-
ρ	Density	kg/m³
$\dot{\rho}_{tr}$	Mass transfer rate	kg/m³.s
σ	Surface tension	N/m
τ	Artificial time step	s

List of Subscripts

Subscript	Description
0	Reference property
avg	Average property
avg, A	Area-averaged property
avg, t	Time-averaged property
c	Cross-sectional property
$cell$	Cell property
$conv$	Convection property
int	Interface property
f	Fluid property
in	Inlet property
l	Liquid phase
mix	Mixture property

out	Outlet property
s	Surface property
sat	Saturation property
$solute$	Solute property
$solvent$	Solvent property
tp	Two-phase property
v	Vapour phase
w	Wall property

List of Acronyms

Acronym	Description
CFD	Computational Fluid Dynamics
CFL	Courant-Friedrichs Lewy number
CHF	Critical Heat Flux
CLSVOF	Coupled Level-Set and Volume of Fluid
CSF	Continuum Surface Force
IC	Integrated Circuit
LS	Level-Set
LE	Leading Edge
ONB	Onset of Nucleate Boiling
PLIC	Piecewise Linear Interface Calculation
SRF	Self-rewetting Fluid
TE	Trailing Edge
UDF	User-Defined Function
VOF	Volume of Fluid

1 INTRODUCTION

1.1 BACKGROUND

Current electronics have higher than-ever cooling demands due to their rapid growth in heat flux and size reduction. This heat flux increase is mainly explained by the development of the integrated circuits (ICs), also known as chips or microchips, used in electronic devices. These IC's are made of many micro-structures such as semiconductors, transistors, resistors, diodes and capacitors which all have some resistance to the flow of electricity. From Joule's law we know that this resistance causes a conversion of energy from electrical to heat energy, thus resulting in an increase of temperature. Since the 1960s, it was observed that IC's were being produced with more and more transistors, described by "Moore's Law" as the number of transistors in an IC being approximately doubled every two years. This is demonstrated in Figure 1-1 which illustrates the rapid growth of transistor count in ICs over the years along with the maximum IC heat fluxes. There is a lot of debate on whether “Moore’s Law” is still valid, however, there is a consensus that it has slowed down. Even so, the rate at which the transistor count on ICs is increasing is still high.

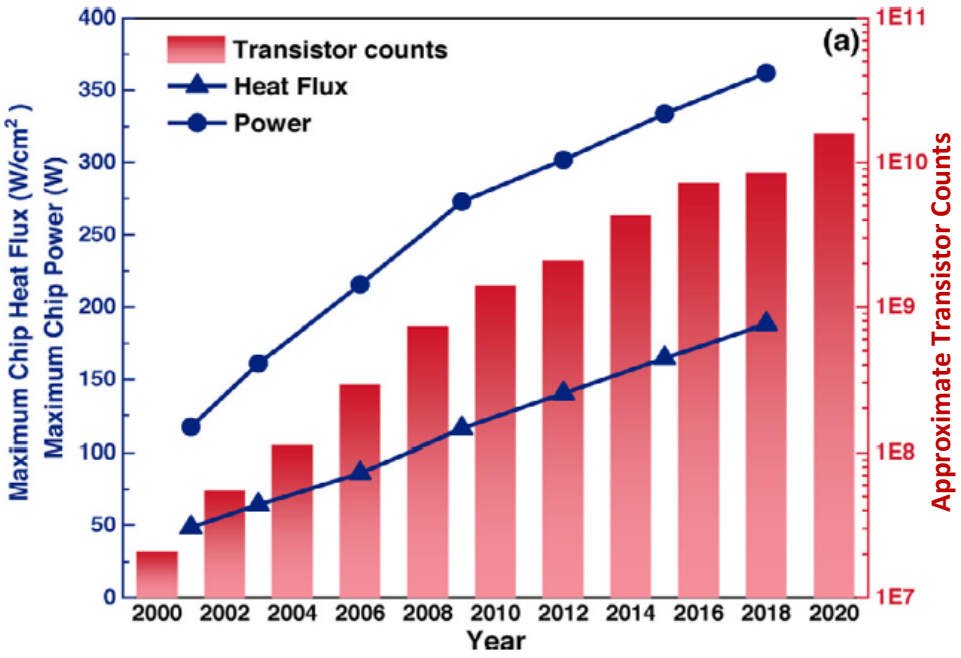

Figure 1-1: The evolution of approximate transistor count, heat flux density, and maximum chip power consumption from 2000 and 2020 [1].

According to a review conducted by Yan et al. [1], the Unites States of America Air Force Avionics Integrity Program found that temperature problems accounted for 55% of electronic equipment failures. It is therefore very important to ensure that capable cooling methods are obtained for current electronics.

Electronic cooling methods are typically grouped into passive and active cooling methods. Passive cooling relies primarily on natural convection, whereas active cooling requires an

external source of energy [1]. However, since active cooling methods generally have better heat transfer capabilities, they are most used in high-power electronic devices. The active cooling methods can then be sub-categorized into indirect and direct contact with the cooling fluid methods, as seen in Figure 1-2. This study is more focused on indirect contact cooling methods such as microchannel cooling, which is shown at the top of the third column with a red border.

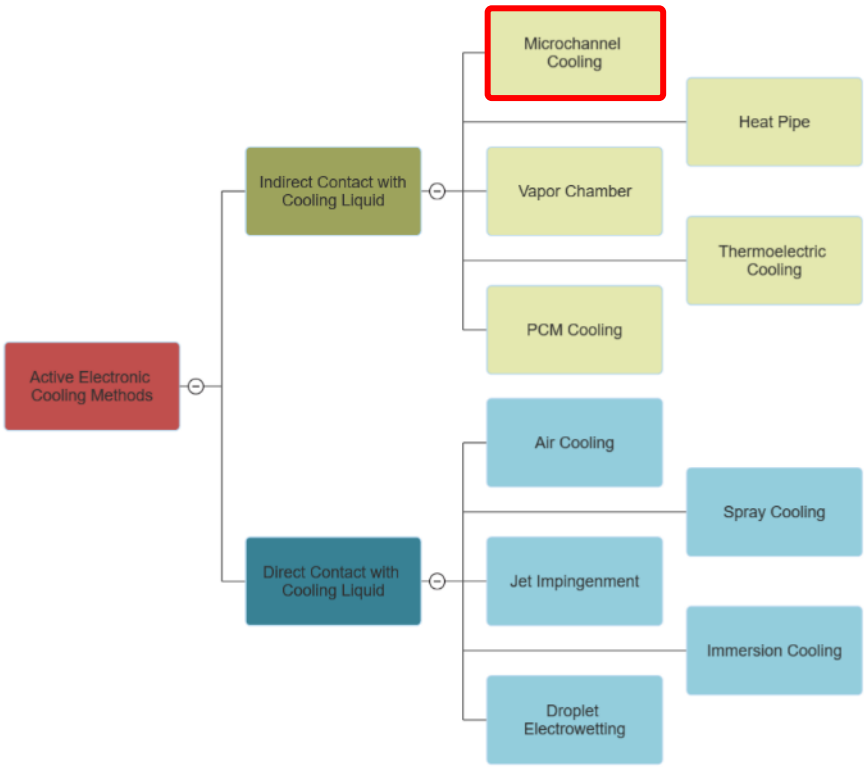

Figure 1-2: Types of active electronic cooling methods [1]. The red border indicates Microchannel flow boiling which is the focal point.

More specifically, indirect contact cooling methods, such as microchannel cooling, dissipate heat via the cooling fluid and an external heat sink. For microchannel cooling, a large amount of research has been done on the defining characteristics of microchannel heat sink geometries, such as the hydraulic diameter, material, and orientation. This study is therefore focused on the cooling fluid used in microchannel cooling, rather than the heat sink geometry.

The fluid used in microchannel cooling can be operated as a single-phase or as a multiphase coolant. In single-phase cooling, heat is transferred to and from the fluid due to a change in temperature, also known as sensible heating. On the other hand, multiphase fluids utilise latent heat transfer (or latent heating), wherein energy is absorbed or released during a phase-change with virtually no change in the fluid's temperature. Single-phase fluids have been, and still are, the most common fluid type used in microchannel cooling, with water being the most common [1]. Other fluids such as refrigerants, nanofluids and liquid metals have also been studied for their heat transfer capabilities and were found to have adequate heat transfer capabilities for most applications. However, for the current high heat flux cooling requirements of microelectronics, sensible heat energy alone is not sufficient. Rather,

a combination of both sensible and latent heat energy, as in multiphase fluids, is required. Flow boiling is used for this purpose in microchannel cooling. The latent heat component in flow boiling allows the fluid to dissipate the high heat flux from the microelectronic surface while maintaining a constant wall temperature at low flow rates. However, during boiling, normal multiphase fluids experience the issue of dry-out regions caused by bubble formations that do not detach from the heated wall. This greatly reduces the heat transfer capabilities of the multiphase fluid as the heat transfer capabilities of a vapour are much lower than those of a liquid, but this can be countered by increasing the fluid flow rate. However, a more recently developed fluid, known as self-rewetting fluids, suggests the ability to avoid this.

Self-rewetting fluids (SRFs), however, have the property of a non-linear relationship between surface tension and fluid temperature, which differs from the decreasing linear relationship of normal fluids. While SRFs also exhibit an initial decreasing trend of the surface tension with temperature, after a certain temperature which forms a 'turning point', the fluids experience an increasing trend in surface tension with temperature (think of a positive parabolic trend). Figure 1-3 illustrates the surface tension – temperature relationship for water, as the normal fluid, and for a 0.2wt% water-heptanol solution as the SRF. This effects the fluid motion at an interface, which is explained by the Marangoni effect. While the Marangoni effect describes the thermo-capillary flow in normal fluids as from a hot region to a cold region around the interface, in SRFs it describes thermo-capillary flow in the opposite direction. This allows the bubbles that are formed during boiling to detach more easily from the wall at high temperatures due to the liquid being forced underneath, thus allowing enhanced cooling.

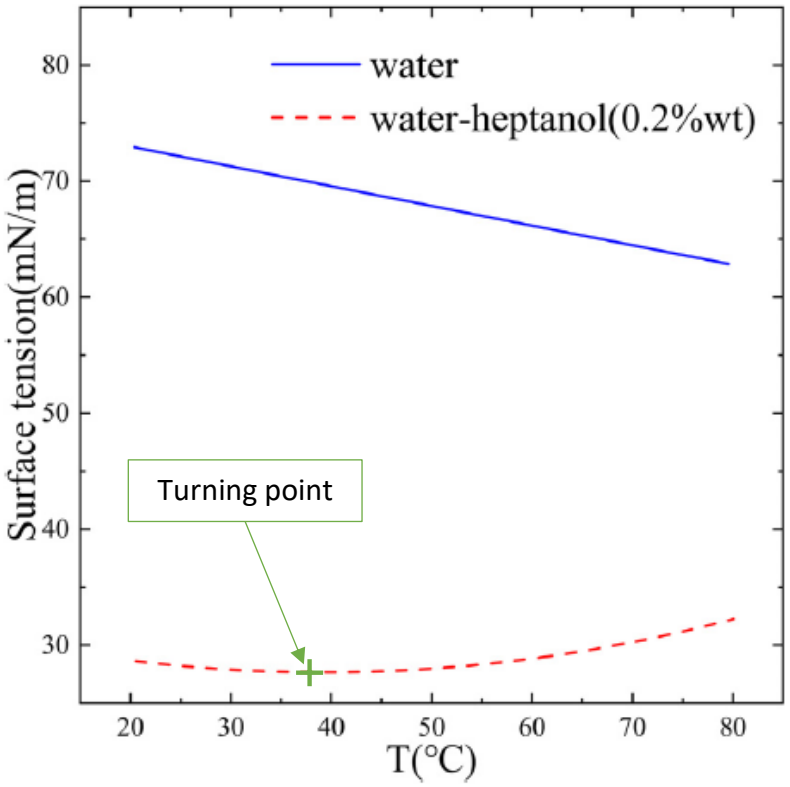

Figure 1-3: Surface tension vs temperature for 0.2wt% heptanol-water solution from Li et al. [2]

SRFs can be produced by preparing dilute aqueous solutions of high-carbon alcohols with 0.2wt% heptanol-water and 5% v/v 1-butanol-water solutions as examples. Very little research has been done on these fluids and it is therefore the aim of this study to add new and useful information on these fluids for prospective researchers and developers. Specifically, the heat transfer capabilities of these fluids in microchannel flow boiling at different heat fluxes are numerically investigated and compared to that of water. This involves investigating the bubble growth from formation to rapid expansion within the channels.

1.2 Problem Statement

Although recent research exists on studying the boiling characteristics of SRFs, little to no research regarding the heat transfer capabilities of SRFs in flow boiling applications such as microchannel cooling is available. Furthermore, of these existing studies, very few are numerical investigations. Li et al. [2], who performed a numerical investigation on the development and merging of bubbles in microchannel flow boiling with SRFs, have performed one of only three numerical studies regarding the flow boiling of SRFs in microchannels. This is common with normal fluids as well, as flow boiling remains a deeply intricate process that is still not well understood.

The heat transfer capabilities of SRFs in microchannel flow boiling have therefore not yet been numerically investigated. The heat flux and bubble growth of a 5% v/v 1-butanol-water SRF solution will thus be numerically investigated and compared to pure water.

1.3 Scope

The scope of the study is as follows:

- Develop a two-dimensional (2D) model of the microchannel in ANSYS Fluent using the Volume of Fluid (VOF) method, phase-change model, and continuum surface force model (CSF) to properly model the flow boiling characteristics and surface tension forces.
- Perform a validation study of the above model to ensure the implementation is trustworthy.
- Perform a comparison study of the heat fluxes and surface temperatures to the experimental results obtained by M. Venter [3].
- The bubble dynamics such as bubble growth, and the heat transfer capabilities should be investigated and compared between the two fluids.

1.4 Layout / Summary

The structure of the report is summarised in this chapter as follows:

Chapter 2 contains a literature study to provide a deeper understanding into microchannel flow boiling, self-rewetting fluids, and the numerical modelling methods used to model these. This is followed by Chapter 3 which describes the numerical methodology used in this study such as the governing equations and solution methods, along with a benchmarking study to verify this method. Chapter 4 discusses the test case geometry derived from experimental

investigations by addressing boundary conditions, meshing, and simulation settings. This chapter also validates the test case geometry to the mentioned experimental investigations. Chapter 5 addresses the main numerical study which investigates the effect of self-rewetting by comparing a 5% v/v 1-butanol-water mixture as the SRF to Pure water. Finally, Chapter 6 contains a conclusion of the work done in this study along with recommendations for future studies.

2 LITERATURE REVIEW

This chapter provides an in-depth literature review of the fundamentals of microchannel flow boiling such as the classification of microchannels, the various flow patterns and the factors influencing them, and flow instabilities. This is followed by a discussion on self-rewetting fluids (SRFs) and their application in flow boiling. Lastly, the available numerical investigations of microchannel flow boiling are discussed addressing their evaporation models and solution methods.

2.1 MICROCHANNEL FUNDAMENTALS

2.1.1 MICROCHANNEL CLASSIFICATION

The classification of channel sizes is an important topic as it is said that the boiling phenomena in mini and microchannels differ regarding heat transfer features, flow regimes, and boiling transition [4]. However, this is a highly debated topic with multiple different classifications identified and no consensus.

In the early developments of heat exchangers, developers aimed to enhance the convection heat transfer rate, given by equation (1), by increasing A_s.

$$\dot{Q}_{conv} = hA_s(T_s - T_f) \tag{2-1}$$

Here $\dot{Q}_{conv}$ is the convection heat transfer rate, h is the convection heat transfer coefficient of the fluid, A_s is the contact surface area, T_s is the contact surface temperature, and T_f is the fluid temperature.

However, as components reduced in size, the surface geometries were altered to ensure the rise in A_s with the addition of fins, thus creating channels. The range of the dimensions for these channels have also increased as they were used in more applications, therefore classifications were required. However, since channels do not differ only by size but also by shape, many different sets of classifications have been developed.

Mehendale et al. [5] organised the channels into four groups based only on channel dimensions such as the hydraulic diameter (D_h), which is used when performing internal flow calculations with non-circular channels and is given by:

$$D_h = \frac{4A_c}{p} \tag{2-2}$$

Here A_c represents the cross-sectional area and p the wetted perimeter.

They classified microchannels as those with $1\mu m < D_h < 100\mu m$, meso-channels as $100\mu m < D_h < 1mm$, compact passages as $1mm < D_h < 6mm$, and conventional passages as $D_h > 6mm$. Kandlikar [6] further developed these classifications by incorporating the flow considerations. They identified conventional channels and mini-channels as those having hydraulic diameters $D_h > 3mm$ and between $3mm > D_h > 200\mu m$ respectively. Microchannels and molecular nanochannels were identified as those having hydraulic diameters between $200\mu m > D_h > 10\mu m$ and $D_h < 0.1\mu m$ respectively. They then also

defined a new region, *Transitional Channels,* which have a hydraulic diameter range of $10\mu m > D_h > 0.1\mu m$ and can be subdivided into transitional microchannels and transitional nanochannels with hydraulic diameters of $10\mu m > D_h > 1\mu m$ and $1\mu m > D_h > 0.1\mu m$ respectively.

However, according to Karayiannis and Mahmoud [7], the above-mentioned classifications are not representative for two-phase flows as they are fluid specific and lack depth in flow physics and effects. For this reason, other researchers have defined the transition criterion from macro to micro scale using dimensionless parameters such as the Eötvös number ($E\ddot{o}$), Bond number (Bo), confinement number (Co), and Laplace constant (La). These dimensionless constants and microchannel classifications are discussed below:

Triplett et al. [8] defined flow microchannels as those with D_h smaller than or of the same order as La, where:

$$La = \sqrt{\frac{\sigma}{g(\rho_l - \rho_v)}} \tag{2-3}$$

Here g represents the gravitational constant, ρ_l and ρ_g are the liquid and gas densities respectively, and σ is the surface tension.

Kew and Cornwell [9] then introduced the confinement number which is derived from the Laplace constant as follows:

$$Co = \frac{1}{D_h}\sqrt{\frac{\sigma}{g(\rho_l - \rho_v)}} \tag{2-4}$$

They classified microchannels as having $Co < 0.5$. However, Ong and Thome [10] experimentally investigated the two-phase flow patterns and liquid film thicknesses of various refrigerants to better-define the macro-micro transition criterion. They observed that the transition region is a gradual transition rather than a sudden transition and should be defined by $0.3 - 0.4 \leq Co \leq 1$, where microchannels are $Co \geq 1$.

Using the linear stability analysis for stratified flows, Brauner and Moalem-Maron [11] defined microchannels as those with $E\ddot{o} > 1$, where:

$$E\ddot{o} = \frac{(2\pi)^2\sigma}{(\rho_l - \rho_v)D_h^2 g} \tag{2-5}$$

They argued that a disturbance with wavelength in the order of the channel diameter should be considered for neutral stability.

A new term known as the *convective confinement number* ($Bo^{0.5} \times Re$) was proposed by Harirchian and Garimella [12], which incorporates the cross-sectional area of the channel, fluid properties, and the effects of mass flux to indicate when a channel should be classified as a microchannel. With:

$$Bo = \frac{g(\rho_l - \rho_v)D_h^2}{\sigma} \tag{2-6}$$

$$Re = \frac{GD_h}{\mu_l} \tag{2-7}$$

where Re is the Reynolds number, μ_l is the liquid dynamic viscosity, and G is the mass flux, they proposed that microchannels are classified by:

$$Bo^{0.5} \times Re = \frac{1}{\mu_l}\left(\frac{g(\rho_l - \rho_v)}{\sigma}\right)^{0.5} GD_h^2 < 160 \tag{2-8}$$

The above-mentioned classifications can all be rewritten in terms of La for comparison. Table 2-1 below summarizes and compares the macro-micro transition criteria discussed above.

Table 2-1: Proposed macro to micro transition criteria

Author	Criterion
Triplett et al. {1999} [8]	$D_h \leq La$
Kew and Cornwell {1997} [9]	$D_h \geq 2La$
Ong and Thome {2010} [10] ($Co \geq 0.3$)	$D_h \leq 3.33La$
Ong and Thome {2010} [10] ($Co \geq 1$)	$D_h \leq La$
Brauner and Moalem-Maron {1992} [11]	$D_h < 2\pi La$
Harirchian and Garimella {2010} [12]	$D_h < \sqrt{\frac{160\mu_l La}{G}}$

Table 2-1 indicates that there is still no real consensus about the defining characteristic of the macro-micro transition in channel flow boiling. It is proposed that research be conducted for specific geometries and fluid types to obtain channel classifications based on the application.

2.1.2 Flow Boiling in Microchannels

According to [13], boiling is classified as either pool boiling or flow boiling. Pool boiling is the phase change of a stationary bulk fluid with the bubble movement mainly due to buoyancy forces. Flow boiling on the other hand is the phase change of a bulk fluid in motion caused by some external force, such as a pump. This study is focussed on flow boiling in microchannels, therefore pool boiling is not discussed any further.

Flow boiling is then classified as either internal or external flow boiling depending on whether the fluid flows over a surface or in a tube. Again, since flow boiling in microchannels specifically is the focal point, only internal flow boiling is considered and will be referred to as *flow boiling*. It is quite well known that the main heat transfer mechanisms in flow boiling are convective and nucleate boiling [7].

Nucleate boiling is the region which starts at the formation of bubbles in the fluid, includes the rapid increase in bubble concentration, and ends when a vapour layer forms over the heated surface (also known as the transition boiling region). In this region, heat is removed via the individual bubbles through evaporation as well as convective flow as the bubble

formation and motion increases. It is said that Nucleate boiling is dominant when an increase in the heat transfer coefficient correlates to an increase in heat flux and system pressure but is independent of the vapour quality and mass flux.

Convective boiling on the other hand is the heat removal by forced convection such as in single-phase forced convection but with an increased gas velocity and rate of thin liquid film evaporation. Convective boiling is said to dominate at high vapour qualities when the flow becomes annular (discussed in the next section) and the nucleation process supresses.

However, as the tube dimensions reduce in size to microchannels, these heat transfer mechanisms are no longer the only mechanisms. Much research has been conducted into defining the heat transfer mechanisms, yet, just as with the channel classification, there is no consensus [14]. It is the belief of Cheng and Xia [14] that this is due to the heat transfer mechanisms and flow patterns being studied individually instead of together. It is therefore more important and helpful to consider the flow patterns in the next section when discussing the heat transfer mechanisms.

2.1.3 Flow patterns

In flow boiling, the vapour generated is confined within the channel and thus moves along with the surrounding fluid. As the vapour content increases, the interaction between the liquid and vapour, which have different thermophysical properties, results in different flow patterns. As mentioned previously, these flow patterns together with the heat transfer mechanisms in microchannel boiling should be investigated to better understand the dominant flow boiling heat transfer mechanisms. This is particularly important for microchannels as the bubble size and dynamics have a larger impact on the heat transfer mechanisms than in conventional channels as the vapour quality is larger.

Halon et al. [15] classify the four main flow patterns in small-scale channels as: bubbly, slug, churn, and annular flow. These flow patterns were observed during an experimental investigation on the two-phase patterns during the flow boiling of R245fa in a microchannel array with the patterns sketched in Figure 2-1. These flow patterns also all have transition patterns between them as the flow progresses, such as the churn-annular pattern. Each of the flow patterns are described below.

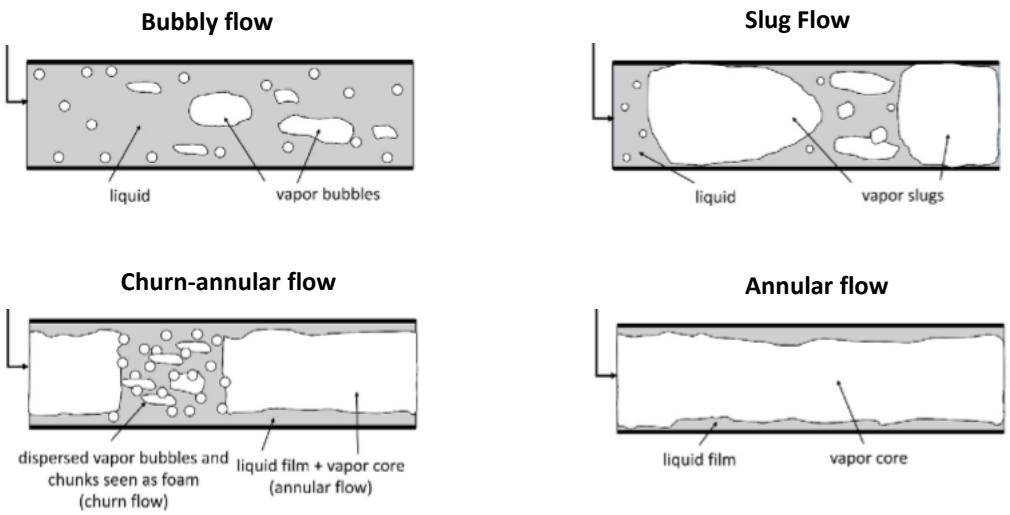

Figure 2-1: Sketches of microchannel flow boiling patterns by Halon et al. [15].

During flow boiling, the subcooled liquid is heated via forced convection until bubbles form on the channel surface [13]. These bubbles, with length smaller than the channel diameter [15], then detach from the channel surface and form part of the main fluid stream, giving a bubbly appearance to the fluid and hence the name Bubbly flow.

As the fluid is heated further, these bubbles grow and eventually coalesce to form larger slugs of vapour. According to Halon et al. [15], these slugs have lengths greater than the channel diameter. This is caused by the restriction of the channel diameter, causing the bubbles to grow along the axial direction. It is said that up to half of the volume in the channel is occupied by vapour during slug flow [13]. According to Bordbar et al. [16], Slug flow is also commonly referred to as Taylor flow, segmented flow, plug flow, bubble train flow, and intermittent flow. Additionally, this flow generally has a thin lubrication layer between the vapour slug and the channel wall determined by the fluid viscous and surface tension forces [16]. However, under specific conditions (such as wettability issues between the fluid and channel wall) these vapour slugs may be in contact with the wall, thus causing dry-out and reduced heat transfer.

As the slugs grow, they eventually begin to distort and break into smaller bubbles trailing behind the slug [17]. This is caused by an increased velocity difference due to the decrease in fluid density which results in the slugs becoming aerated, forming a chaotic flow pattern known as Churn flow. In Figure 2-1, the region of small bubbles and slugs in the churn-annular flow sketch represent the chaotic churn flow pattern. It is important to note that the flow inside the channel is a combination of large, distorted slugs and smaller bubbles, and not just small bubbles.

With continued heating, the vapour quality of the fluid continues to increase until the vapour slugs and bubbles in the chaotic churn flow coalesce into a single vapour core through the channel. This is caused by an increased shear force along the bubble interface above the buoyancy force, forcing the liquid to flow only in the annular region between the vapour core and the channel wall. According to Guo et al. [18] annular flow appears early at low vapour qualities, thus making it the dominant flow regime in microchannel boiling. They also state

that annular flow is hydrodynamically unstable (turbulent) due to instabilities at the phase interfaces.

For data analysis purposes, the flow regimes are often separated into two classifications namely intermittent flow (I) and annular flow (A). In both bubbly and slug flow, vapour exists in the fluid in the form of bubbles or slugs, and both share nucleate boiling as the primary heat transfer mechanism. These shared characteristics allow them to be classified together as intermittent flow [15]. On the other hand, Halon et al. [15] consider churn and annular flows to both be inertia driven flows with similar thermal behaviour and forced convective heat transfer being dominant in both. Additionally, it is often noted that churn and annular flow regimes occur in an alternating fashion and are therefore together classified as annular flow.

As mentioned before, understanding the different flow regimes is crucial in finding the heat transfer mechanisms in flow boiling, specifically in microchannels. The flow classifications for data analysis mentioned above allow the flow patterns to be grouped and presented as flow pattern maps. These maps are obtained experimentally and show the distribution of flow patterns in flow boiling depending on factors such as channel geometry, mass flux, vapour quality, heat flux, and saturation temperature. These maps indicate the transition lines between the intermittent and annular flows which are important in understanding the dominant heat transfer mechanisms.

2.1.4 FACTORS INFLUENCING FLOW PATTERN TRANSITION

There are multiple factors which can influence the transition between the flow patterns previously discussed such as mass flux, heat flux, saturation temperature, and channel size. These factors were investigated in many experiments such as those conducted by Halon et al. [15], Revellin et al. [19], Charnay et al. [20, 21, 22], Kubo et al. [23], Yang et al. [24], and Keepaiboon and Wongwises [25] which are briefly discussed below to help better understand their influences.

Halon et al. [15], Charney et al. [20], Kubo et al. [23], and Revellin et al. [19] experimentally investigated the two-phase flow boiling patterns of R245fa in: (1) 1 mm rectangular channels with and without 0.5 mm inlet restrictions, (2) 3 mm circular channels, (3) 1.04 mm and 0.55 mm semi-circular channels, and (4) 0.5 mm and 0.8 mm circular channels respectively. In addition to the above study, Revellin et al. [19] investigated the two-phase flow boiling of R134a in 0.5 mm and 0.8 mm circular channels, and Keepaiboon and Wongwises [25] investigated this in a single D_h = 0.68 mm rectangular channel. Lastly, Yang et al. [24], in a smooth horizontal tube with an inner diameter of 6 mm, experimentally investigated the two-phase flow of R1234ze(E).

INFLUENCE OF MASS FLUX

Halon et al. [15] observed that as the mass flux is increased, the transition from intermittent to annular flow occurs at lower vapour qualities. According to Revellin et al. [19], this is explained by the rate of bubble coalescence, which is the dominant factor in intermittent/annular transition. As the mass flux is increased, the rate at which bubbles

coalesce increases, causing transition at lower vapour qualities. The experiments conducted by Revellin et al. [19], Charnay et al. [21], and Kubo et al. [23] reached similar conclusions to those mentioned above. The consensus from these investigations indicate that the channel geometry and saturation temperature do not play a significant role in the influence of the mass flux on the transition to annular flow.

INFLUENCE OF HEAT FLUX

It can be said that as the heat flux increases, the vapour quality at transition from intermittent to annular flow increases [15]. This is because as the heat flux increases, the local pressure decreases and the local enthalpy increases, causing the local vapour qualities to increase. This means that as the heat flux increases, transition occurs at a higher vapour quality, however, not necessarily at a later position along the channel's length. Rather, a higher heat flux causes transition to occur sooner along the length of the channel as it results in an increase of bubble departure size and frequency. This again was observed by other studies such as Charney et al. [20] [22], which further solidify the observation.

INFLUENCE OF SATURATION TEMPERATURE

Across the experimental investigations, it was noted that as the saturation temperature increased, the transition vapour quality increased, meaning that transition occurred at higher vapour qualities. This can be explained by the fact that increasing saturation temperature results in a decrease in bubble departure diameter due to a drop in surface tension, which reduces the rate of bubble coalescence and ultimately, the formation of annular flow [15]. This therefore indicates that increasing the saturation temperature causes transition to be delayed both in vapour quality and in location along the channel. Using photos captured from a high-speed camera, Keepaiboon and Wongwises [25] confirmed these findings.

2.1.5 FLOW INSTABILITY

Flow instability is an important topic in microchannel flow boiling due to the detrimental influence it has on system cooling performance. It is said that instability causes the system parameters such as mass flow rate, temperature, and pressure to oscillate drastically [7]. A review study by Karayiannis and Mahmoud [7] mention that these fluctuations have been recorded as high as $36K$ for wall temperature, $60kPa$ for pressure drop, and $992.4kg/m^2s$ for mass flux. Prajapati and Bhandari [26] attempted to provide a state-of-the-art review of flow boiling instabilities in microchannels and found that bubble dynamics such as bubble clogging, rapid bubble growth, and flow reversal, as well as parallel channel interaction and oscillating flow are major causes to trigger instabilities.

QUANTIFYING INSTABILITIES

According to Prajapati and Bhandari [26], a definitive quantification of the transition from stable to unstable flow boiling is still required. This is because there exist many different criteria explaining this transition. It has been proposed that the Bond number, Bo, described in equation (2-6), is a valid parameter to quantify instabilities in microchannels. It is said that instability usually occurs for small Bo, especially when it is less than unity [27]. Lee et al. [27] then proposed a parameter, R, as an instability criterion which considers the force balances

on the liquid-vapour interface at the upstream end of a bubble. Figure 2-2 shows a model of this instability as shown by Lee et al. [27] which is then followed by the description of parameter R in equation (2-9).

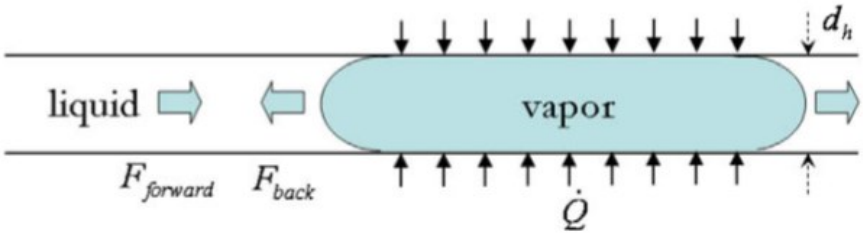

Figure 2-2: Flow instability model obtained from Lee et al. [27]

$$R = \sqrt{\frac{F_{back}}{F_{forward}}} \tag{2-9}$$

where F_{back} is the evaporation momentum of the bubble moving backwards (upstream) and $F_{forward}$ is the liquid inertia force moving forward towards the bubble (downstream). $F_{forward}$ and F_{back} can be described by:

$$F_{forward} = \frac{G^2 A}{\rho_l} \tag{2-10}$$

$$F_{back} = \frac{1}{4\rho_v A}\left(\frac{\dot{Q}}{h_{lv}}\right)^2 \tag{2-11}$$

Here A is the area, $\dot{Q}$ is the total heat supplied, and h_{lv} is the latent heat of vaporization. It was then concluded that the flow is said to be stable if R is less than unity [26]. Other criteria have been defined based on the exit vapour quality and Reynolds number, and on the heat and mass fluxes ($\dot{q}$ and G). As mentioned before, more effort is required in the identification of instability criteria for flow boiling due to the many different criteria currently defined.

BUBBLE DYNAMICS

As mentioned above, the instabilities caused by bubble dynamics can be described in three stages, namely: Bubble clogging, rapid bubble growth, and flow reversal, as shown in Figure 2-3.

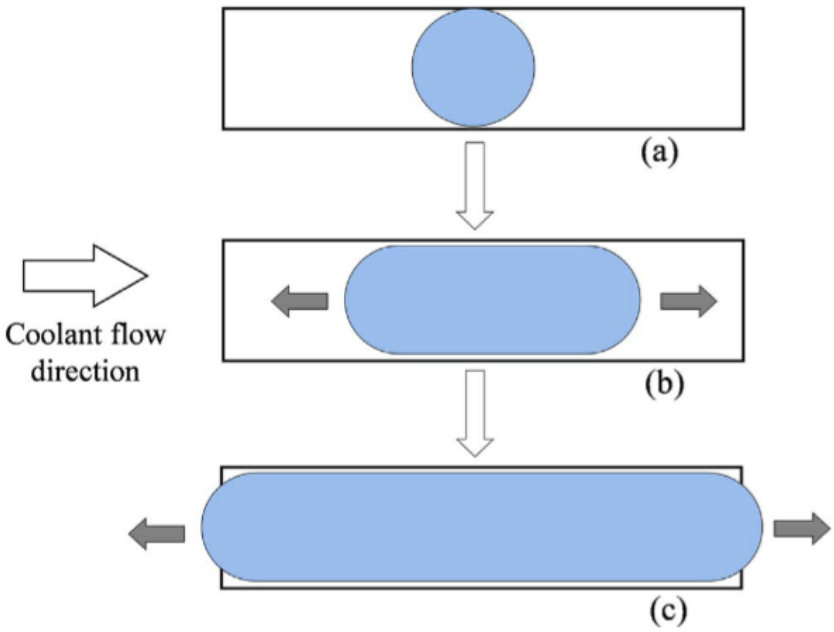

Figure 2-3: The three phases of bubble development: (a) bubble clogging, (b) rapid bubble growth, and (c) flow reversal. [26]

It can be said that bubble dynamics starting with bubbles clogging the confined channels can cause severe flow boiling issues. After the start of nucleation, bubbles rapidly begin to grow until they reach the size of the channel diameter, thus clog the channel. Once this occurs, the bubbles grow laterally (upstream and downstream) into a vapour slug as described in the flow patterns section. These slugs, as in full annular flow, contain a thin liquid film between them and the channel wall surfaces wherein thin film evaporation occurs. During this rapid growth, it has been observed that the bubbles remain stationary for a short period of time experiencing small axial oscillations, which cause the evaporation in the thin liquid film to result in the formation of dry patches [7]. The dry patch causes a spike in the wall temperature and ultimately an early critical heat flux (CHF) [26].

Another detrimental effect of rapid bubble growth is flow reversal. As the bubble stretches upstream, flow reversal is induced resulting in flow instabilities which further deteriorate the heat dissipation process [26]. According to Prajapati and Bhandari [26], studies conducted by others such as Steinke and Kandlikar, found that this flow reversal usually occurs in parallel microchannels and result in the dry-out condition discussed above.

OSCILLATING FLUID PARAMETERS

It is common that during flow boiling, oscillations in parameters such as temperature and pressure occur. These oscillations are due to flow instabilities caused by bubble dynamics as discussed before, resulting in dry-out and wetting [26]. However, under certain conditions these oscillations may become self-sustained which can cause flow instabilities and thus a reduction in the cooling capabilities.

Qu and Mudawar [28] investigated the fluid flow instabilities and pressure drop in a two-phase microchannel heat sink with water as the working fluid. They found that once the heat

flux was increased above the incipient boiling value (the point where the onset of nucleate boiling occurs), a significant increase in vapour production in the microchannels occurred resulting in a severe pressure drop oscillation. As the vapour generation increases, the flow resistance in channels increases. This causes the flow rate to reduce inside the channels which ultimately increases the upstream pressure. Once the pressure is large enough, all the vapour is pushed out of the channels. If this periodic behaviour becomes self-sustained, severe flow oscillation occurs and, as mentioned before, pre-mature CHF occurs. However, Qu and Mudawar [28] found that this drastic pressure drop oscillation can be mitigated by throttling the flow upstream.

Another study by Kuang et al. [29], where the flow boiling of ammonia in mini channels was investigated, observed oscillations in both temperature and pressure. They observed that temperature oscillations occur in-phase with the pressure oscillations. This is because due to the slowing of the vapour bubble (discussed above), the annular region is full of liquid. This liquid evaporates which subsequently increases the wall temperature and decrease the liquid film thickness. Then as the vapour bubble is forced out of the channel, new sub-cooled liquid enters the channel and cools the wall.

PARALLEL CHANNELS

It is well known that equal mass flow rate is required in each channel for parallel channel heat sink design. If this is not the case, once the flow from each channel combines at the outlet, instabilities occur [26]. As mentioned earlier, rapid bubble growth often results in flow instabilities in microchannels. For a parallel channel configuration, the bubble growth in each channel is not the same which results in instabilities and flow oscillations. This is caused by pressure oscillations across the channels resulting in uneven mass flow rates. Many investigations have been conducted to reduce the onset of flow instabilities in parallel channels. Prajapati and Bhandari [26] discuss the investigations done by other researchers and mention that header design may present promising reduction in parallel channel instabilities. Additionally, they also mentioned that a study conducted by Megahed [30] found that cross-link channels allow for more uniform flow and temperature distribution. However, they also found that this caused the pressure drop to increase significantly.

2.1.6 SURFACE AFFECTS

It is important to understand surface affects, such as surface characteristics and surface wettability, on microchannel flow boiling. This is because channel fabrication is easily altered and enhanced compared to fluid properties for optimum heat transfer.

SURFACE CHARACTERISTICS

It is said that surface characteristics, such as the surface microstructure, significantly impact the local heat transfer rate in microchannels [7]. However, the effects have not rigidly been quantified due to inconsistent results. Karayiannis and Mahmoud [7] believe that this is because many researchers rely on the average surface roughness to represent the surface which fails to fully capture the surface structure in relation to boiling. They suggested that

studies be conducted on the flow boiling heat transfer of a surface with a specific microstructure and then compared to the same surface with varied structure.

Alam et al. [31] experimentally investigated the effects of surface roughness on flow boiling in silicon micro-gap heat sinks. They used deionized water at 91°C in three different micro-gap heat sink sizes with various average surfaces roughness values. They observed that the surface roughness greatly influenced the boiling incipience and that the nucleation site density for bubbles increased as the surface roughness increased. This resulted in increased bubble coalescence into vapour slugs. However, it was noted that the surface roughness effect was not clearly influenced by the micro gap dimensions. Furthermore, it was also observed that lower wall temperatures were required for the onset of nucleate boiling (ONB) using rougher surfaces. Alam et al. [31] claimed that a rise in surface roughness caused the local heat transfer coefficients to increase, however Karayiannis and Mahmoud [7] suggest that this may not be true and that their observation could be explained by experimental uncertainty.

Mahmoud et al. [32] experimentally investigated the surface effects in flow boiling of R134a by using two differently manufactured stainless steel tubes. The one tube was welded which gave a smooth surface, whereas the second was seamlessly cold drawn giving a comparatively rough surface. They concluded that the different tubes experienced completely different flow boiling characteristics. The seamless cold drawn tube experienced nucleate boiling as the primary mechanism for heat transfer whereas the welded tube did not illustrate a clear dominant mechanism. Additionally, the welded tube experienced large fluctuations in the heat transfer coefficients, whereas the cold drawn tube experienced a uniform heat transfer rate through the tube. They attributed this to the different inner surfaces of the two tubes caused by their manufacturing processes. The welded tube has a smoother surface with few random nucleation sites, which possibly explain the large fluctuations in heat transfer coefficient, whereas the cold drawn tube has a rougher surface with more nucleation sites resulting in nucleate boiling. It was also observed that the first bubbles were observed at lower heat fluxes in the cold drawn tube than in the welded tube due to the earlier ONB with the increased surface roughness.

Surface roughness remains a broad topic with little consensus on its true meaning. Surface roughness parameters such as Ra, lack the ability to capture morphological surface features such as gaps and microcavities which facilitate the entrapment of vapour embryos necessary for nucleation. Because of this, two studies with differing surface characteristics may have identical surface roughness parameters but differing boiling characteristics. More research is required to better quantify the impact of surface roughness on heat transfer during flow boiling in microchannels.

Surface Wettability

Surface wettability, due to contact angle, is another surface affect that has not received much attention. Figure 2-4 represents a schematic drawing from Karayiannis and Mahmoud [7] defining the contact angle used to describe surface wettability. Wettability can be described as a fluids ability to spread over a surface, where the contact angle between the fluid and the

surface is measured as demonstrated in Figure 2-4. It is expected that surface wettability will influence the heat transfer processes in microchannel flow boiling, however, according to Karayiannis and Mahmoud [7], not enough research has been conducted to form rigid conclusions on its effects.

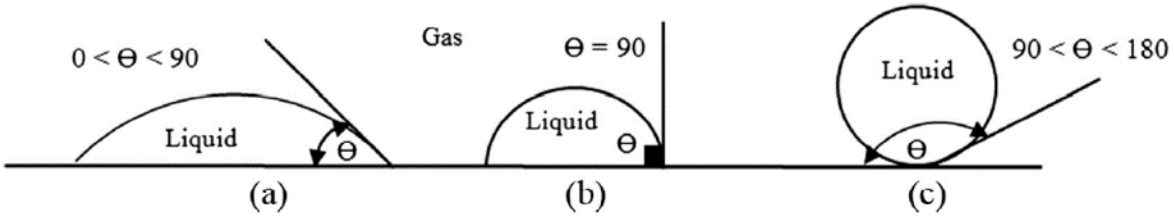

Figure 2-4: Schematic drawing of surface wettability defined by contact angle by Karayiannis and Mahmoud [7]; (a) wetting surface (hydrophilic), (b) non-wetting surface, and (c) highly non-wetting surface (hydrophobic)

From Figure 2-4 it can be noted that a wetting surface is known as hydrophilic with a contact angle between 0° and 90°, whereas a non-wetting surface is known as hydrophobic with a contact angle between 90° and 180°. An experimental investigation by Liu et al. [33], studied the microchannel flow boiling characteristics of water using various surfaces ranging from very hydrophobic to super-hydrophilic. The surfaces were made by plasma trench on a silicon wafer where the hydrophilic surface experienced a 36° contact angle, and the hydrophobic surface was made with a thin layer of low surface energy material providing a contact angle of 103°. They observed that the cyclic flow processes related to nucleation, bubble growth, and coalescence only occurred on the hydrophilic surface. The hydrophobic surface was not suitable for nucleation, instead lead to a severe superheat of the liquid with a sudden bubble growth once formed. For a super-hydrophilic surface with nanowire arrays, they observed a large nucleation of bubbles resulting in many small bubbles. Liu et al. [33] partially attributed this to the many nucleation sites created by the nanowire arrays which may skew the data. Additionally, the larger number of small bubbles mean that cyclic motion mentioned earlier is not generated and thus bubble growth and coalescence is not readily achieved.

Choi et al. [34] investigated the flow boiling behaviours in hydrophobic and hydrophilic microchannels. They used water in a single rectangular channel comprised of photosensitive glass which is initially a hydrophilic surface with a contact angle of 25°. To represent the hydrophobic surface, the surface was coated with octadecyltrichlorosilane with a contact angle of 105°. The vapour quality, heat flux, and mass flux were also altered in the investigation. They observed that the hydrophobic surface experienced larger heat transfer than the hydrophilic surface due to an increased nucleation rate, except for at the lower mass flux condition. They also observed that only a few bubbles nucleated and merged in the hydrophilic channel resulting in a stable liquid film around the bubble whereas the hydrophobic channel experienced many bubbles which merged and resulted in an unstable liquid film around the bubble. Furthermore, nucleation was observed in the liquid film of the hydrophobic case with a delay in dry out occurring which both attributed to its enhanced heat transfer results. Lastly, a larger two-phase pressure drop was observed in the hydrophilic channel which was attributed to the dissipation of moving triple-lines.

According to Karayiannis and Mahmoud [7], from previous studies such as the two discussed above, some concluding remarks on the effect of surface wettability on heat transfer can be made. Firstly, bubble size at boiling incipience is larger in non-wetting surface than in wetting surfaces. This means that slug flow develops immediately at boiling incipience in non-wetting surfaces. Secondly, this results in earlier boiling in non-wetting surfaces than wetting surfaces. Lastly, partial dry out is delayed (in terms of vapour quality) in non-wetting surfaces.

2.2 Self-Rewetting fluids (SRFs)

Surface tension is the elastic force that acts at a liquid-vapour interface due to the liquid having larger attracting forces than the vapour. Due to surface tension forces, the interfacial surface has the tendency to reduce to its smallest possible surface area. These forces are also responsible for the resistance of lower density substances from penetrating the higher density substance. As surface tension decreases due to a reduction in the liquid attractive forces, the interfacial tendency to reduce in size decreases, meaning that the interface is more inclined to stretch and break up, causing the liquid to evaporate.

As mentioned before, normal two-phase fluids experience a decrease in surface tension with an increase in temperature which results in delayed bubble departure. This delayed bubble departure results in increased dry-out regions and thus reduced CHF. A more recently studied fluid type, known as a self-rewetting fluid (SRF), has the unique property of a non-linear dependence of surface tension with temperature in which the surface tension rises again after a certain temperature. These fluids are liquid solutions, with majority of those studied being alcohol-aqueous solutions. An example of a SRF investigated in literature is the $0.2wt\%$ heptanol-water solution studied by Li et al. [2], with the surface tension and fluid temperature relationship illustrated previously in Figure 1-3. The increased surface tension at higher temperatures allows the bubbles to depart more easily from the surface due to an intensification of the thermal Marangoni effect, which is referred to as the Marangoni effect.

The Marangoni effect, or thermo-capillary convection, can be described as the mass transfer along an interface between two phases due to a surface tension gradient. This surface tension gradient exists because of local variations in the fluid temperature. In normal fluids, as the temperature increases, the attractive forces in the liquid decrease resulting in a lower surface tension force. This means that the liquid repels the vapour with a reduced intensity. If a temperature gradient exists along the interface, the difference in attractive forces cause tangential interfacial forces to form which act towards the larger attractive forces i.e. from the hotter region to the colder region. However, due to the increasing nature of the surface tension in SRFs, the introduced tangential interfacial forces cause this thermo-capillary flow to be in the opposite direction. This explains why in normal fluids, as higher heat fluxes are applied and surface temperatures increase, less fluid is drawn to flow in between the bubble and the channel wall causing the dry-out region. On the other hand, in SRFs, the fluid is drawn to flow towards the higher surface temperature region and consequently wedge in between the bubble and the channel wall. It should be noted that, in addition to the thermal Marangoni effect described above, there also exists a solutal Marangoni effect for fluid mixtures such as the SRFs. The solutal Marangoni effect instead explains the movement of the interface due to the formation of a concentration gradient at the liquid surface which is caused by the

depletion of the more volatile component near the nucleation site. With this, it is said that the most important properties of SRFs are the fluid concentration and solute [35] and should therefore be investigated.

2.2.1 Flow Boiling Of SRFs

Few researchers have investigated flow boiling of SRFs. This section aims to identify those that have and what has been learnt from them.

Wu [35] studied the application of SRFs in a loop heat pipe and the effect they had on heat transfer performance. They used SRFs of various concentrations and solutes, such as butanol, pentanol, and hexanol, to identify the best SRF by measuring their surface tensions. According to Wu [35], the surface tension reversal trend becomes less obvious as the carbon chain in an alcohol becomes longer. Therefore, the above-mentioned solutes (butanol, pentanol, and hexanol) were used. Additionally, Wu [35] also stated that literature suggests that the saturation concentration is the preferred concentration. Therefore, concentrations for each solute around their saturation concentration were investigated and compared. They found that concentrations of 6% butanol, 2% pentanol, and 0.3% hexanol were the best for each concentration with the surface tension trend most prominent at each. From these they then found that the 6% butanol solute had the largest increase in surface tension after the reversal point. Then comparing this solute-aqueous solution to water in a loop heat pipe, they found that the critical heat load was 2.5 times larger, and the thermal resistance decreased by roughly 60%. Their results indicate the potential of using SRFs in high heat flux cooling applications.

Sitar and Golobic [36] experimentally investigated flow boiling of water, 2% and 6% aqueous-butanol solutions, and pure butanol in parallel array microchannels. The microchannels were fabricated in a silicon wafer with heating applied via an electric heater to the bottom of the external wafer surface. The measured heat flux and measured maximum temperature on the external wafer surface results are represented in Figure 2-5. It can be noted that larger measured heat fluxes corresponded to larger measured maximum surface temperatures. Additionally, it should be noted that the decreasing heat flux label refers to method in which the experiments were conducted. Heating was applied until boiling occurred in all the microchannels, thereafter the heat flux was gradually decreased, and the results were captured as this would allow only the working fluid characteristics to affect the temperature measurements [36]. Sitar and Golobic observed that the introduction of n-butanol solutions into the microchannels allowed for longer cooling due to the reduction/delay of dry-out regions. This, as explained before, was due to the unique surface tension properties of these fluids leading to an intensified Marangoni effect. In terms of cooling capability, they observed that both the 2% and 6% n-butanol solutions lowered the maximum measured temperature by approximately 10 K and 30 K compared to the pure water and pure butanol respectively, shown in Figure 2-5. Further observations made using high-speed visualization techniques gave a deeper insight into this. They observed that the two 2% and 6% n-butanol solutions had thicker annular liquid regions during the annular flow which allowed for improved wettability of the microchannel walls, and thus enhanced the heat transfer and lowered wall temperatures.

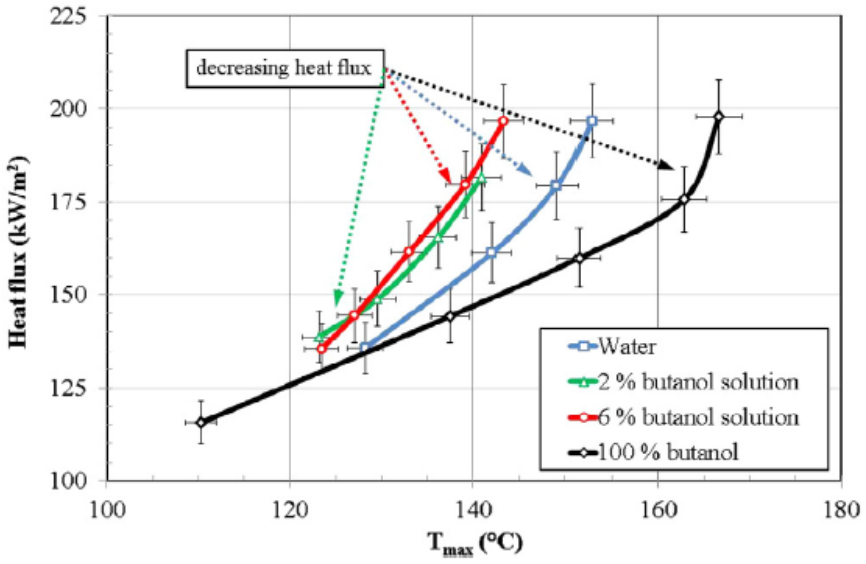

Figure 2-5: Heat flux vs maximum temperature observed by Sitar and Golobic [36] using various water-butanol solutions in 25 x 25 µm array microchannels.

Hosseinzadeh et al. [37] experimentally and numerically investigated the effects of aqueous solutions on heat transfer characteristics in two-phase closed thermosyphons. They considered solutions of pure water, 0.6% water-hexanol, 2% water-pentanol, and 6% water-butanol and compared their results. They found that the 6% water-butanol solution resulted in the highest thermosyphon efficiency and lowest thermal resistance. The water-butanol outperformed the pure water by 9% when altering the input power. Additionally, it was observed that the 6% water butanol solution enhanced the heat transfer coefficients at both the evaporator and condenser by approximately 18% when manipulating the filling ratio. Interestingly, from the numerical investigation it was found that the addition of butanol to the water resulted in a change in boiling regime. It was observed that the butanol solution experienced higher rates of boiling (more bubbles released from the wall) which lowered the wall temperatures, reducing thermal resistance and increasing thermosyphon efficiency. Also, the butanol solution caused dropwise condensation to occur rather than film-wise condensation as detected by the water solution. Dropwise condensation increases the condensation rate due to increased vapour contact region, consequently reducing the condenser wall temperature resulting in reduce thermal resistance and increased thermosyphon efficiency as mentioned above.

In another study conducted by Sitar et al. [38] the onset of nucleate boiling of SRFs was investigated in an array of 50 x 50 μm microchannels. Experimental analysis comparisons were made of the flow boiling of pure water and four SRFs namely, 6% aqueous-butanol, 2% aqueous-pentanol, 0.2% aqueous-hexanol, and 0.15% aqueous-heptanol. Contrary to the above studies, some of the pitfalls of using SRFs in microchannel boiling were encountered. When using the SRFs, Sitar et al. [38] observed a delayed ONB of up to 57 K for the 6% aqueous-butanol solution. This means that higher temperatures were reached before phase change occurred with SRFs compared to water. Once boiling occurred, it was also noted that the water solution outperformed the SRFs despite the large surface tension gradient of the

SRFs. Furthermore, upon visualization of the boiling phenomenon it was noticed that the SRFs experienced abrupt and oscillatory boiling in a misty two-phase flow. Sitar et al. [38] attribute these shortcomings mainly to the lack of accurately sized nucleation cavities and smooth contact surfaces. They therefore suggest that these pitfalls be addressed at the fabrication design stage of the microchannel to ensure that the benefits of SRFs are obtained.

2.3 Computational Modeling of Flow Boiling in Microchannels

2.3.1 Introduction

The high rate of current technological advancements mean that experimental investigations are becoming more accurate and adjustable. The advancements have resulted in vastly improved data capturing technologies such as high-speed and high-resolution infrared cameras which allow researchers to visualize boiling phenomena more closely. These technologies have been mentioned in many of the experimental investigations discussed throughout this literature review. Despite the advancements in these technologies, the data capturing process using these methods can be very memory demanding and the post-processing can be very time consuming. Furthermore, the accuracy required to predict the exact fluid states of flow boiling in microchannels is still lacking due to the small nature of these channels. Instead, numerical methods, such as computational fluid dynamics (CFD) simulations, enable researchers to model the complex physics of flow boiling and illustrate the fluid state in these small channels. Figure 2-6 shows an example of how accurately experimental visual results can be produced with a numerical model.

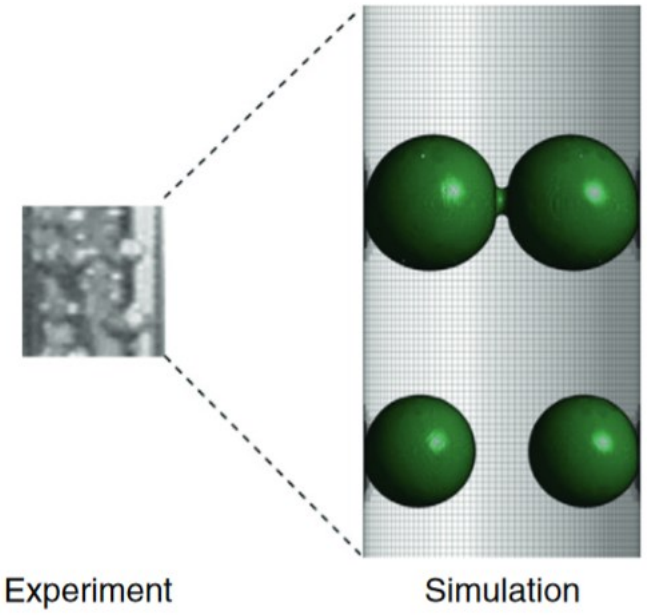

Figure 2-6: An example of the accuracy of experimental results compared to a numerical model obtained from Liu et al. [41]

Numerical models can provide a better understanding of the physical phenomena that occurs during flow boiling at very small scales. However, it is very possible for numerical models to be inaccurate. This is due to the multiple algorithms, model parameters, and boundary

conditions used to solve a numerical model. For these reasons it remains important to validate numerical models against well-trusted analytical, numerical or experimental results. Validation allows the researcher to quantify and ultimately reduce, the errors that occur from the numerical model.

When it comes to creating a numerical model, many decisions are to be made. Firstly, the domain investigated should be defined. This includes deciding whether to perform a two-dimensional (2D) or three-dimensional (3D) analysis. It is often also suggested that symmetry be used when modeling domains as this will reduce the domain size and consequently reduce the solution time [37]. Next, the domain boundary conditions should be defined to ensure that the correct physics is modelled over the domain. Lastly, before algorithms and solvers are selected, the domain needs to be divided into a grid-like structure, also known as meshing. The importance of meshing should never be understated, especially in heat transfer and complex fluid flow applications such as flow boiling. In meshing, nodes are the points which define the grid lines, dividing the domain into many mesh elements. The algorithms solve the model physics at each of these nodes to model the physical phenomena occurring. Therefore, the finer the mesh (the more mesh nodes and elements) the higher the resolution and the more accurate the results. Meshing also allows one to divide the domain finely in areas of high interest, such as around a bubble, and coarsely in areas which are not as important. This can also reduce computational time as the number of elements drive the computational time.

Lastly, the algorithms, or solvers, are chosen based on the required application. Many different algorithms exist for various applications and thus literature should be studied to select the most suitable algorithms. For this study, the model should be able to accurately model bubble physics, confined flow motion, and fluid heat transfer. Additionally, the model should also be able to alter the surface tension to model SRFs. These are further discussed below by comparing numerical investigations concluded by others.

2.3.2 Modelling methods

Literature suggests that Eulerian-based interface capturing methods such as the volume of fluid (VOF) method and the level-set (LS) method are mostly used for the analysis of two-phase flow [39]. The VOF method is described as a region-following scheme with minimum storage requirements [40]. Here, a function F is defined for a single cell in a mesh such that when it has a value of unity, then the cell is said to be full of fluid. When F is zero, the cell contains no fluid, and when F is between zero and unity, the cell contains at least one free surface. Additionally, according to Hirt and Nichols [40], the normal direction to the boundary lies in the same direction in which F changes the fastest. Using both F and the normal direction, the VOF creates a line which cuts the cell and approximates an interface. According to Liu et al. [41], the VOF is a one-fluid algorithm with good mass-conservation nature but poor interface reconstruction and surface tension calculation due to inaccurate interface curvature estimations. On the other hand, the LS method is better at estimating interface curvatures and calculating surface tension as it is a smooth function, however it has poorer mass conservation. This observation of the LS method is worsened when the interface experiences stretching or tearing.

As surface tension is very important at the small scale of microchannels, improvements to these methods were required. One improvement is to combine them to create a new algorithm. By combining the methods, a coupled level-set and volume of fluid method (CLSVOF) was developed by Sussman and Puckett [42]. CLSVOF solves both LS and VOF methods using VOF to linearly reconstruct the interface at each time increment, and LS to calculate the surface tension. This enhances the algorithms mass conservation and curvature estimation significantly, but unfortunately increases the complexity. The integration of the VOF and LS methods is commonly implemented in applications involving microchannel flow boiling. According to Sussman and Puckett [42], they proved that, in the relevant applications, their CLSVOF method performed as well or better than the LS and VOF methods. Another method which combined the level-set method with the volume of fluid method, known as VOSET, was developed by Sun and Tao [43]. This VOSET method is a simpler approach to combining the LS and VOF methods than the CLSVOF method. It calculates the LS geometrically based on the reconstructed interfaces, removing the need to solve the advection equations. This removes the need for high-order schemes while still capturing the accuracy of the LS method [44].

Guo et al [39] mentioned another improvement proposed by Malik et al. for a 2D system and by Hernandez et al. for a 3D system, which is the addition of a height function method. It has been shown that when in combination with the convection continuum surface force (CSF) model, the VOF method suffers from what is known as the spurious currents problem caused by its lack in surface tension modelling capabilities [39]. The CSF model represents surface tension as a continuous effect across an interface by using body forces, instead of defining it as a boundary condition value at the interface. However, these effects have been minimized by the PRESTO! (PRessure STaggering Option) scheme provided by ANSYS Fluent which calculates a staggered pressure field and reduces the mismatch between the pressure gradient and the surface tension force. The height function method was developed to replace the CSF model for application in the VOF method in annular flow modelling. Guo et al. [39] modified and implemented the height function method into ANSYS Fluent by using User-Defined Functions (UDFs). They found the height function method to be a robust and effective approach in calculating the interface for orthogonal meshes. Furthermore, they found that this method could provide 2nd order accuracy and could successfully simulate annular flow with large curvature waves.

2.3.3 EXISTING NUMERICAL SIMULATIONS

Ling et al. [45] conducted a 3D direct simulation of rectangular microchannel flow boiling using the VOSET method. They studied the growth and merger of bubbles as well as their impact on the heat transfer. The interface reconstruction was conducted using a piecewise linear interface calculation (PLIC), and the linear equations were solved using the Bi-conjugate gradient stabilized (BI-CGSTAB) method. From their investigation, Ling et al. [45] concluded that the bubble growth obtained from their simulation compared well with experimental data in literature. Figure 2-7 shows the simulated growth of a single vapour bubble by Ling et al. [45]. At t = 0.0 ms, the initial small vapour bubble is represented on the bottom channel wall. This bubble expands outwards until initial confinement within the width (t = 0.7 ms) of the

channel which causes the bubble to grow upwards and towards the channel outlet (to the right). At t = 0.9 ms, the bubble becomes confined vertically as well, this means that the bubble can only expand upstream and downstream, thus elongating into a vapour slug. Finally, at t = 1.2 ms it can be noted that rapid expansion along the channel length is occurring with a vapour slug fully formed. Figure 2-7 reiterates the capabilities of CFD simulations for use in better understanding the flow characteristics for micro applications such as flow boiling in microchannels.

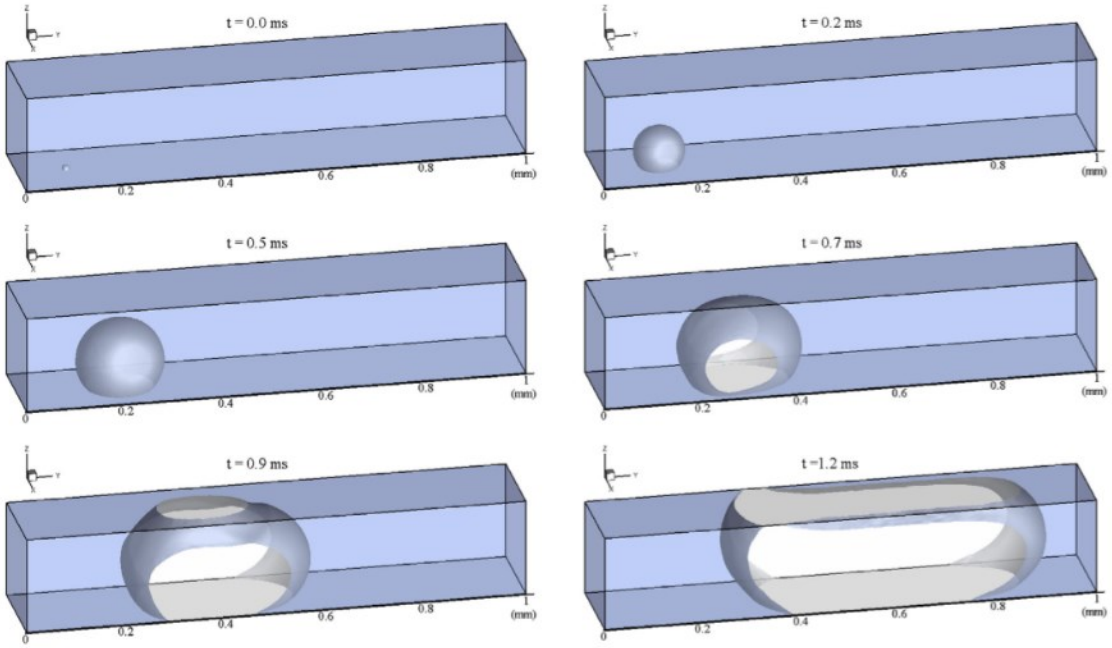

Figure 2-7: Numerical simulation modelling the development of an individual bubble within a microchannel conducted by Ling et al. [45]

In a different study conducted by Liu et al. [41] the interaction and coalescence of multiple bubbles during flow boiling in vertical microchannels were considered. Here the CLSVOF method was used to reconstruct the two-phase interface, and a non-equilibrium phase model was used to calculate the interface heat flux. Two perpendicular and symmetric boundaries were defined at the center of the tube allowing for a domain reduction and only a quarter of the tube being simulated. Additionally, they conducted a single-phase steady state laminar simulation and used the results as the initial conditions for the multiphase simulation. A constant wall heat flux was applied with no-slip condition and the inlet boundary condition was obtained from the single-phase simulation which used a uniform velocity and temperature boundary condition. Validation sets proved that the phase change model, surface capturing model, and coalescence models performed well. Furthermore, a mesh independency study was conducted and proved to be successful.

As mentioned earlier, Li et al. [2] were one of very few to have performed a numerical investigation of microchannel flow boiling with SRFs. More specifically, they performed a 3D numerical investigation on the bubble growth and merger of these fluids in microchannels. They used a 0.2% water-heptanol solution as the SRF. The VOF method and Hardt's phase

change model [46] were extended to OPENFOAM to capture the two-phase interaction and to reveal the evaporation characteristics during this phase change. The Hardt's phase change model is an evaporation model developed to be largely independent of an interface-capturing scheme, such as the LS method. Furthermore, it was developed specifically to study microscale evaporation phenomena but has not been limited to it. Additionally, a CSF model was adopted in OPENFOAM to model the surface tension accurately. Regarding the investigation conducted by Li et al. [2], as a validation case, a single bubble growth in a microchannel using pure water was conducted and the results were compared to experimental results obtain by Mukherjee et al. The validation results, shown in Figure 2-8, show that the model by Li et al. [2] agreed well with the experimental results. The agreeability of the results by Li et al. [2] with the experimental results further indicate the capabilities of the VOF method and Hardt's phase change model for use in the current numerical study.

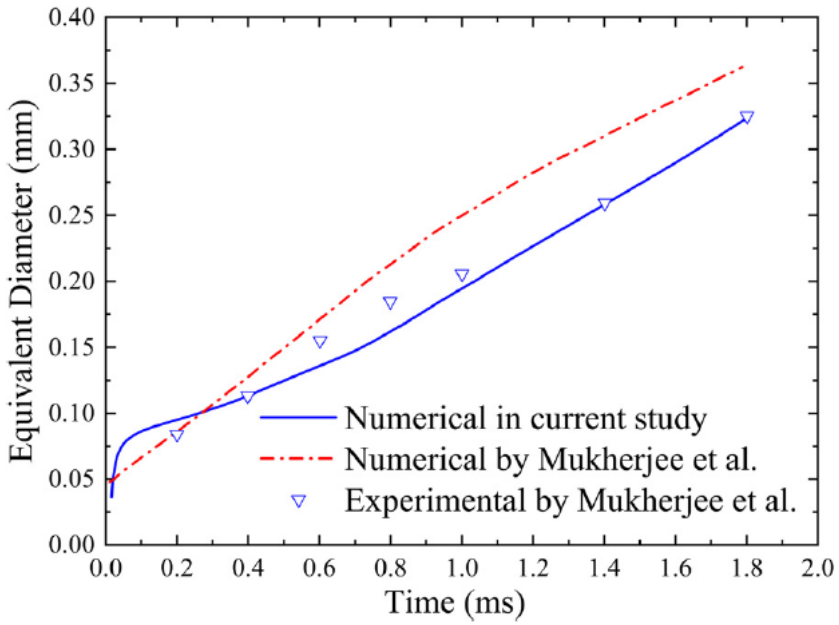

Figure 2-8: Li et al. [2] validation of a single bubble growth in comparison to the results from Mukherjee et al.

2.4 CHAPTER SUMMARY

This literature review stared by discussing the fundamentals of microchannel flow boiling. The wide variety of microchannel classifications were discussed and illustrated just how much work still needs to be done on these channels. Thereafter, the dominant heat transfer mechanisms were discussed in conjunction with the flow patterns as observed by multiple different experimental investigations. Since the flow patterns are important in understanding the heat transfer mechanisms, the factors influencing the flow patterns such as heat flux, mass flux, saturation temperature and channel geometry, were discussed. Thereafter, additional microchannel flow boiling influences such as flow instability and surface affects were discussed to indicate the importance of selecting the correct channel materials and configurations.

A brief discussion on self-rewetting fluids (SRF) provided to provide a better understanding of what these fluids are chemically, as well as why they promise to provide heat transfer benefits. This means that the Marangoni effect is discussed in detail to better understand how surface tension impacts thermos-capillary flow.

Lastly, the modelling of microchannel flow boiling in computational fluid dynamics (CFD) packages were discussed. The modelling methods, boundary conditions, and solution methods were discussed to indicate their importance in obtaining accurate and trustworthy results. Existing microchannel flow boiling numerical investigations were highlighted to better understand which combination of modelling methods would be most appropriate for the current study.

In the next chapter, the numerical method used is extensively discussed. The governing equations, evaporation model, and adaptive mesh refinement model used are discussed to illustrate how the numerical study was performed. Furthermore, benchmarking tests were included in this section to verify that the numerical model was implemented correctly.

3 NUMERICAL METHOD AND BENCHMARKING

This chapter discusses the numerical methods used in ANSYS Fluent 23R1 for the current study by considering the governing equations, evaporation model, and discretization methods. It also discusses how the evaporation model and adaptive mesh refinement code were implemented using a user-defined function (UDF). This is then followed by the discretization methods and solution procedure which illustrate the steps taken to run the simulations and ensure convergence. Finally, the benchmark tests used to verify the implementation of the UDF are discussed.

It should be clear by now that surface tension is a crucial factor in this study. This is true for both flow boiling in microchannels and for self-rewetting fluids (SRF). Gravity and surface tension are three-dimensional (3D) forces and therefore require 3D simulations to accurately investigate their effects. However, 3D simulations are very computationally demanding as the require many mesh elements to be solved and stored. To cope with this obstacle, all the simulations were run as two-dimensional (2D) studies. Although 2D simulations may not provide the same level of accuracy as the 3D simulations, they are still able to provide important details. Three-dimensional studies were attempted; however, the necessary computing time was not available. Adaptive mesh refinement was applied which tracks the two-phase interface and refines the cells in this region, while coarsening the cells further away. This reduces the overall number of mesh elements.

An in-house code previously developed by Potgieter [47] for accurately simulating microchannel flow boiling was used for the current study. This made use of the ANSYS Fluent 23R1 CFD software package, which is a well-known and trusted package. The code was dependent on the volume of fluid (VOF) method for modelling multiphase flows and worked in conjunction with the continuum surface force (CSF) method. The code was implemented into Fluent as a user-defined function (UDF) to provide the modified Schrage evaporation model (also referred to as Hardt's phase-change model by Li et al. [2]). This was developed after noticing that Fluent only offered the Lee evaporation model which was shown to be more suitable for macro-scale applications. The code, or UDF, also implemented the adaptive mesh refinement for the bubble interface.

3.1 GOVERNING EQUATIONS

In numerical simulations, a set of partial differential equations, known as the Navier-Stokes equations, are solved to describe the motion of viscous fluids.

As mentioned previously, the VOF method considers the two phases as distinct fluids that do not interpenetrate, maintaining a well-defined interface between them. Each region of the domain is assigned a value of either zero or unity, indicating the volume fraction (φ) of the respective phases. The VOF method then uses these two fluids to obtain a set of single-fluid properties such that only one set of governing equations is solved. The single-fluid properties are calculated as weighted averages using φ with the following expression where density is used as an example property:

$$\bar{\rho} = \rho_l \varphi + (1 - \varphi)\rho_v \tag{3-1}$$

Here ρ can represent other fluid properties such as k, c_p, or μ. The superscript bar denotes the use of the single-fluid approach. With all properties calculated in the same manner, this means that for each iteration, only one set of conservation equations need to be solved.

To ensure mass conservation within the system, the first partial differential equation, the continuity equation, is employed. This equation states that the mass inside a system can neither be created nor destroyed, and is represented by the following expression:

$$\frac{\partial \rho}{\partial t} + \nabla(\rho \tilde{u}) = 0 \tag{3-2}$$

Here $\tilde{u}$ as the velocity vector and ∇ is the gradient operator.

Equation (3-2) says that the rate of mass change within a cell (the first term) and the rate of mass entering and exiting the cell (the second term), should balance each other out. It can be expanded into 2D as follows:

$$\frac{\partial \rho}{\partial t} + \rho\left(\frac{\partial u_x}{\partial x} + \frac{\partial u_z}{\partial z}\right) = 0 \tag{3-3}$$

Similar to mass, momentum conservation is also required. The following equation enforces the conservation of momentum:

$$\rho\left(\frac{\partial \tilde{u}}{\partial \tilde{t}} + \tilde{u}.\tilde{\nabla}\tilde{u}\right) = -\tilde{\nabla}P + \mu\tilde{\nabla}^2\tilde{u} + \rho g + F_\sigma \tag{3-4}$$

$$F_\sigma = \frac{\sigma\bar{\rho}\kappa_l\nabla\varphi_l}{\frac{1}{2}(\rho_l + \rho_v)} \tag{3-5}$$

Here P is the pressure and F_σ represents any additional forces, which in this case is the surface tension force. The CSF method is used to model the surface tension force is with Hardt and Wondra [46] defining this with $F_\sigma = \sigma\kappa\nabla\varphi$. Here κ is the interface curvature, σ is the surface tension, and $\nabla\varphi$ is the volume fraction gradient. ANSYS Fluent implements this using equation (3-5). The terms on the left of equation (3-4) guarantee that the momentum contained in the cell is balanced with the momentum that exists the cell via fluid motion. On the right-hand side, other factors such as the surface tension force, viscous dissipation, pressure, and gravitational head are included, all of which can influence the momentum of a cell.

The third partial differential equation is the conservation of energy. It regulates how heat is transferred between cells and is represented by:

$$\rho c_p\left(\frac{\partial T}{\partial t} + \tilde{u}.\tilde{\nabla}T\right) = k\tilde{\nabla}^2T + \tilde{\nabla}h_{lv}\dot{m} + S_e \tag{3-6}$$

Here S_e represents any additional energy source terms defined by the user. Like the momentum equation, the left-hand side of the expression ensures that the energy stored within the cell as well as the energy passing through the cell via mass flow is conserved. The terms on the right of the equation represent the energy transfer via conduction and the

isothermal energy transfer due to phase change, shown by $\tilde{\nabla} h_{lv} \dot{m}$. Here h_{lv} represents the latent heat of vaporization with units J/kg, therefore the term $\tilde{\nabla} h_{lv} \dot{m}$ can be shown to describe the energy transferred via a phase change (boiling).

In addition to the Navier-Stokes equations, two less-common equations are required to properly model microchannel flow boiling. The first being the volume fraction advection equation which is used in the VOF method, and the second being the standard advection equation which allows us to implement additional models via a user-defined function (UDF). The volume fraction advection equation is another form of the continuity equation which guarantees that the volume fractions in each cell is conserved, and is used to track the interface between the two phases with the following form:

$$\frac{1}{\rho}\left[\frac{\partial}{\partial t}(\varphi\rho) + \nabla.(\varphi\rho\tilde{u})\right] = \frac{1}{\rho}\left[S_m + \dot{\rho}_{tr,lv} - \dot{\rho}_{tr,vl}\right] \tag{3-7}$$

Here the subscripts in $\dot{\rho}_{tr,lv}$ and $\dot{\rho}_{tr,vl}$ represent the mass transfer from the liquid phase to the vapour and vice versa, and S_m represents the mass source term for each phase and is zero by default. Although $\dot{\rho}_{tr,lv}$ and $\dot{\rho}_{tr,vl}$ account for the mass transfer between the two phases, numerous mass transfer models exist for applications such as evaporation and condensation. The source term allows for implementation of the various mass transfer models making the current form of Equation (3-7) a general form.

The volume fraction entering and exiting the cell is governed by the advection equation, shown by the terms on the left of the equation. In contrast, the terms on the right conserve the volume fraction throughout condensation, evaporation, and any other relevant source terms. In this study, the mass source term is used to implement an evaporation model by Hardt and Wondra [46] by means of a UDF which is discussed later. ANSYS Fluent only solves Equation (3-7) for the secondary phase, which in our case is the vapour phase, and instead solves the primary phase, liquid, using the constraint:

$$\sum_{v=1}^{n} \varphi_v = 1 \tag{3-8}$$

The motion of an arbitrary user-defined scalar quantity, ϕ, is monitored by the standard advection equation, which is expressed as follows:

$$\frac{\partial \phi}{\partial t} + \nabla.\phi\tilde{u} = \phi\nabla.\phi \tag{3-9}$$

This equation serves both the mesh refinement and mass transfer models, which are implemented using a UDF and will be discussed later.

ASSUMPTIONS:

Several assumptions were made to simplify the equations above. Both liquid and vapour phases were considered as viscous ($\gamma \neq 0$), immiscible, and incompressible (constant ρ). The interfacial surface tension was modeled using the CSF method wherein surface tension was defined as a continuous body force applied across the interface in place of a boundary value

condition at the interface. Also, due to the low Reynolds number (Re) used throughout the study ($Re \approx 30$), flow was assumed to be laminar, and no turbulence models were included.

Applying the assumptions, the equations above can be simplified as follows:

$$\nabla(\tilde{u}) = 0 \tag{3-10}$$

$$\bar{\rho}\left(\frac{\partial \tilde{u}}{\partial \tilde{t}} + \tilde{u}.\tilde{\nabla}\tilde{u}\right) = -\tilde{\nabla}P + \bar{\mu}\tilde{\nabla}^2\tilde{u} + \bar{\rho}g + \frac{\sigma\bar{\rho}\kappa_l\nabla\varphi_l}{\frac{1}{2}(\rho_l + \rho_v)} \tag{3-11}$$

$$\bar{\rho}\bar{c_p}\left(\frac{\partial T}{\partial t} + \tilde{u}.\tilde{\nabla}T\right) = \bar{k}\tilde{\nabla}^2T + \tilde{\nabla}h_{fg}\dot{m} + S_e \tag{3-12}$$

$$\frac{\partial \phi}{\partial t} + \nabla.\phi\tilde{u} = \phi\nabla.\phi \tag{3-13}$$

$$\frac{1}{\bar{\rho}}\left[\frac{\partial}{\partial t}(\varphi\bar{\rho}) + \nabla.(\varphi\bar{\rho}\tilde{u})\right] = \frac{1}{\bar{\rho}}\left[S_m + \dot{\rho}_{tr,lv} - \dot{\rho}_{tr,vl}\right] \tag{3-14}$$

Since the two phases were considered incompressible, Equation (3-2) reduced to (3-10) by setting $\frac{\partial \rho}{\partial t} = 0$. Equation (3-4) was re-written as Equation (3-11) by substituting Equation (3-5) into the surface tension force. The rest of the equations remain mostly unchanged except that the fluid properties were re-written with a bar superscript (i.e. $\rho \rightarrow \bar{\rho}$) indicating that the single-fluid properties are used, which are obtained using Equation (3-1).

These equations are crucial for maintaining solution stability across all time steps and for achieving reliable results.

3.2 User-Defined Function

The UDF used was developed for ANSYS Fluent by Jarryd Potgieter [47], a previous student at the University of Pretoria. It implements a modified Schrage evaporation model by Hardt and Wondra [46] as well as a mesh refinement function. These two models are briefly described below.

3.2.1 Mass Transfer Model (Evaporation Model)

For the current study where we are interested in both the growth of bubbles in a channel as well as their heat transfer capabilities, modeling the interface of the bubble and the mass transfer to and from the bubble is very important. We have discussed the governing equations behind the VOF multiphase method, which is a surface-tracking technique, above and thus we will now discuss the mass transfer model.

The mass transfer model is crucial as it models the evaporation that takes place and will therefore simulate the growth of the bubble in the channel. Unfortunately, this very important model is extremely difficult to implement correctly. This is because boiling processes such as coalescence, nucleation, condensation, and evaporation are not well understood, even less so at the micro-scale. For that reason, approximations and correlations based on experimental results are often used to simulate the mass transfer [48].

According to Mudawar and Kharangate [48], three mass transfer models are primarily used in two-phase schemes. These are the Lee model, the Rankine-Hugonoit jump condition, and the Schrage model. All three models have been thoroughly discussed by previous students such as Potgieter [47], who showed that a modified Schrange model would be best suited for microchannel flow boiling. This is because the Rankine-Hugonoit jump condition does not account for kinetic energy contributions, and the Lee model is known to cause phase change across the entire liquid domain at the micro scale.

The Schrage model on the other hand, is grounded in the kinetic theory of gases which establishes a relationship between the mass transfer across the interface and the temperature and pressure of the phases. It does this by using an accommodation coefficient, ω. This coefficient quantifies the proportion of high-energy molecules that pass through the interface in relation to the overall number of high-energy molecules impacting it. The mass flux proposed by Schrage is expressed as follows:

$$\dot{\rho}_{tr} = \frac{2\omega}{2-\omega}\sqrt{\frac{M}{2\pi R}}\left[\frac{P_v}{\sqrt{T_{v,sat}}} - \frac{P_l}{\sqrt{T_{l,sat}}}\right] \tag{3-15}$$

Here $\dot{\rho}_{tr}$ is the mass transfer rate, M is the molecular mass, R is the ideal gas constant, and $\omega = 1$. The accommodation coefficient has a lot of uncertainty with a value for water ranging between $10^{-3} < \omega \leq 1$ [46]. A value of unity is selected as it represents an ideal case and is said to result in the fastest evaporation rate since each excited molecule impacting the interface also crosses the interface (evaporates). Kunkelmann [49] suggested that accommodation coefficients between 0.5 and 1 have numerically been shown to have insignificant influence on the results. By using a value of one for this study, it removes the influence of user defined variables, such as the accommodation coefficient, when comparing the evaporation rate between the self-rewetting and non-self-rewetting fluids and therefore places more emphasis on the effects of fluid properties such as surface tension.

This model was then simplified by Tanasawa [50] by suggesting that, for small interfacial temperature differences, the temperature difference present at the interface has a linear relationship with the mass flux that cross it. Additionally, Tanasawa also assumed that both $T_{l,sat}$ and $T_{v,sat}$ are equal and remain constant. The mass flux can then be described by:

$$\dot{\rho}_{tr} = \frac{2\omega}{2-\omega}\sqrt{\frac{M}{2\pi R}}\left[\frac{\rho_v h_{lv}(T - T_{sat})}{T_{sat}^{3/2}}\right] \tag{3-16}$$

With the mass transfer rate calculated, the volumetric mass source term is obtained in relation to the interfacial area using:

$$S_{m,v} = -S_{m,l} = \dot{\rho}_{tr} A_{int} = \dot{\rho}_{tr}|\nabla\varphi| \tag{3-17}$$

Here $S_{m,v}$ and $S_{m,l}$ are the vapour and liquid mass source terms respectively. The interfacial area, $A_{int} = |\nabla\varphi|$, can be expressed as the magnitude of the volume fraction gradient.

Unfortunately, the assumption that $T_{l,sat}$ and $T_{v,sat}$ remain constant is not suitable for boiling of mixtures due to the presence of a concentration gradient. This limitation is common among several existing models used for mixture modelling and should be addressed in future work.

Furthermore, Tanasawa's model is not well-suited for handling phase changes at the micro or nano scale. The is because, at small scales, the interfacial curvature can generate noticeable Laplace pressures, and the Van der Waals forces acting at the solid-liquid interface can become significantly large, resulting in a phase imbalance with negative volume fractions. This challenge was addressed by Hardt and Wondra [46], who developed a model wherein the source term is smeared. This model conserves the overall interfacial mass transfer while restricting the vapour and liquid source terms to their respective domains of pure vapour and pure liquid.

Figure 3-1 illustrates how Kunkelmann [49] applied the Hardt and Wondra technique to smear the source and sink terms, followed by the procedure for incorporating this smearing into the current model.

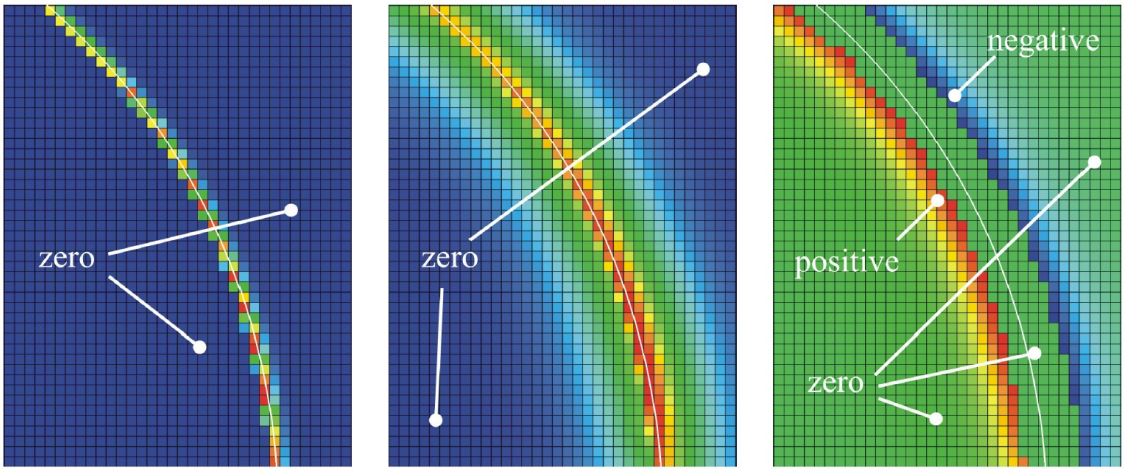

(a) $S_{m,0}$ (b) $S_{m,1}$ (c) S_m

Figure 3-1: Representation of the smearing source term around the two-phase interface by Kunkelmann [49].The white curves illustrate the two-phase interface (φ = 0.5). The colour scale indicates the mass source term values. (a) The initial sharp source term before smearing across the interface; (b) The initial sharp source term after smearing across the interface; (c) The final source term represented along the pure phase lines.

Figure 3-1 illustrates the smearing of the source term with $S_{m,0}$ and $S_{m,1}$ representing the initial and smeared source terms respectively. The colour scale used indicates the value of the source term with red indicating a positive source term and blue indicating a zero-source term in Figure 3-1 (a) and (b). In Figure 3-1 (c), the colour scale extends to include a negative source term represented by blue, green representing a zero-source term, and red a positive source term. This is done to separate the two phases with the positive source term used for the vapour phase and a negative source term used for the liquid phase.

1. Figure 3-1(a) illustrates the initial sharp source term, $S_{m,0}$, which is described by:

$$S_{m,0} = N_0 \dot{\rho}_{tr} \varphi |\nabla \varphi| \tag{3-18}$$

Here N_0 is an initial normalization factor and $\dot{\rho}_{tr}$ is obtained using (3-16) above. The presence of φ in Eq. (3-18) is to ensure that only the liquid field values of the interface determine the evaporation mass transfer. The normalization factor is obtained using:

$$N_0 = \frac{\int_\Omega |\nabla\varphi| d\Omega}{\int_\Omega \varphi |\nabla\varphi| d\Omega} \tag{3-19}$$

Where Ω represents the local computational flow domain.

2. Smearing of the initial source term across the interface is then performed such that a portion of the source term exists on either side of the interface as illustrated in Figure 3-1(b). This smearing is done by solving a steady diffusion equation given by:

$$S_{m,1} = S_{m,0} + (D\Delta\tau)\nabla^2 S_{m,1} \tag{3-20}$$

Here D is the diffusion constant and $\Delta\tau$ is an artificial time step. The diffusion constant is manually altered by the user to control the width of the smearing which is directly related to the square root of two factors, namely the chosen diffusion constant and the simulated artificial time step ($\sqrt{D\Delta\tau}$). Selecting a diffusion constant that is too small could result in the mass transfer occurring too rapidly while a value that is too large would result in mass transfer far away from the interface. Because of this, the diffusion constant needs to be altered with respect to the mesh size. For a domain with three mesh refinement levels, Potgieter [47] defined the diffusion constant by dividing the fluid density by a value of 500 ($D = \frac{\rho}{500}$) for each phase. As discussed in Chapter 3.2.2, three levels of mesh refinement were used in this study and therefore the same definition for D was implemented. To maintain equivalence between the smeared source term field $S_{m,1}$ and the initial sharp source term field $S_{m,0}$ after smearing, Neumann boundary conditions are imposed on all boundaries of the domain. This is important as the smearing should not alter the source term scalar quantity, only spread it across cells along both sides of the interface.

3. This step acts as a cropping step to remove any source terms in the smeared interface region. The source terms in any cells near the interface that contain a mixture of phases (where $0 < \varphi < 1$) are set to zero. This distributes the source terms into only the pure vapour or liquid regions. This step is important as it means that the interface is transported via the velocity field only and does not affect the source term field. The final source term implemented into ANSYS Fluent, S_m, is shown in Figure 3-1(c) with the conditions:

$$S_m = \begin{cases} N_v(1-\varphi)S_{m,1} & if\ \varphi < 0.001 \\ N_l\varphi S_{m,1} & if\ \varphi > 0.999 \\ 0 & if\ 0.001 \leq \varphi \leq 0.999 \end{cases} \tag{3-21}$$

where N_l and N_v are the normalization factors which guarantee that the initial source term matches with the volume integral of the source terms for the liquid and vapour phases. These normalization factors are expressed by:

$$N_v = \frac{\int_\Omega S_{m,0} d\Omega}{\int_\Omega (1-\alpha) S_{m,1} d\Omega} \tag{3-22}$$

$$N_l = \frac{\int_\Omega S_{m,0} d\Omega}{\int_\Omega \alpha S_{m,1} d\Omega} \tag{3-23}$$

4. During the implementation of the source terms, mass is removed from the liquid phase and injected into the vapour phase. This does not account for the total enthalpy in the region remaining constant, which causes heat being applied to the liquid and heat being removed from the vapour. A source term is incorporated into the energy equation which considers the enthalpy of formation and addresses the issue above by using:

$$S_e = -S_{m,0} h_l + N_v(1-\varphi) S_m c_{p,v} T - N_l \varphi S_m c_{p,l} T \tag{3-24}$$

Potgieter [47] performed two simulations investigating the importance of the above steps. He observed that missing any of the steps would result in a breakdown in the interface, causing a vapour region to form along the heated wall.

3.2.2 Adaptive Mesh Refinement Model

As mentioned in Chapter 2.3, to solve any numerical problem, the domain first needs to be divided into smaller, grid-like sub-domains known as meshing. The points where these grid lines meet are known as the nodes, and the sub-domains formed by the grid lines and the nodes are known as the mesh elements or cells. ANSYS Fluent solves the necessary equations such as the mass transfer model and the Navier-stokes equations discussed above, at the cell centres. These results are then interpolated to the nodes for a smoother visualization. Since the physics is solved at an elemental level using theoretical formulations and approximations, dividing the domain into smaller, and therefore more, elements means that the results can in theory converge to the exact solution. This is because the properties are constant over an element, and increasing the number of elements allows for more variation in the global properties, resulting in more accurate depictions of flow fields or temperature gradients etc. It Is therefore important to have a fine enough mesh, however not too fine as this drastically increases the required computation power and time.

Meshes, or grids, can be divided into two categories, namely structed and unstructured grids. Structured grids are characterized by a systematic arrangement of node connections, with quadrilateral elements employed in two-dimensions (2D) and hexahedra (such as cuboids) in three-dimensions (3D). An example of a structured grid in 2D is illustrated below in Figure 3-2.

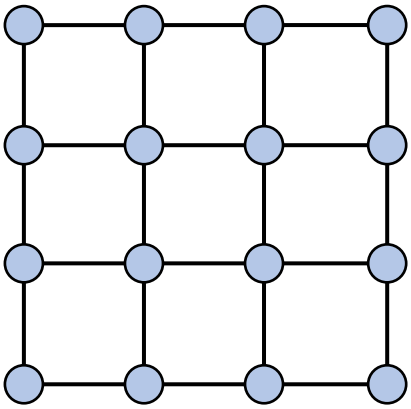

Figure 3-2: Illustration of a structured grid in 2D.

Unstructured grids, however, do not have a general structure in how the elements are connected. They therefore consist of triangular elements in 2D and tetrahedra in 3D. In this study, only structured grids were used, and thus unstructured grids are not discussed.

Having structure in the way that the elements are connected allows the domain to be easily defined by 2D or 3D arrays. This simplifies the algorithms required to order the elements and identify neighboring elements. However, if fine mesh elements are required in a particular region, then using a structured grid drastically increases the overall number of elements, which mentioned previously, is unwanted. In contrast, unstructured grids have the advantage of accommodating complex geometries, but at the expense of algorithm simplicity. If fine mesh elements are required in a region, the unstructured grid can more easily accommodate this change in cell volume without drastically increasing the overall mesh element count.

One way to accommodate the poor scaling of structured grids is to apply mesh refinement. Mesh refinement divides the elements into smaller, equally sized sub-elements. This means that for regions where small mesh elements are required, such as at an interface, the large elements in the region are refined into many smaller elements and the elements away from this region are not altered, as shown in Figure 3-3. This helps to prevent a drastic increase in the number of mesh elements required. However, when simulating a moving interface, mesh refinement will result in all the interfacial elements being refined as the interface moves, which may cause majority of the domain to end up being refined. To counter this, a criterion is usually implemented which coarsens elements that have been refined and are no longer required to be. This process is referred to as adaptive meshing.

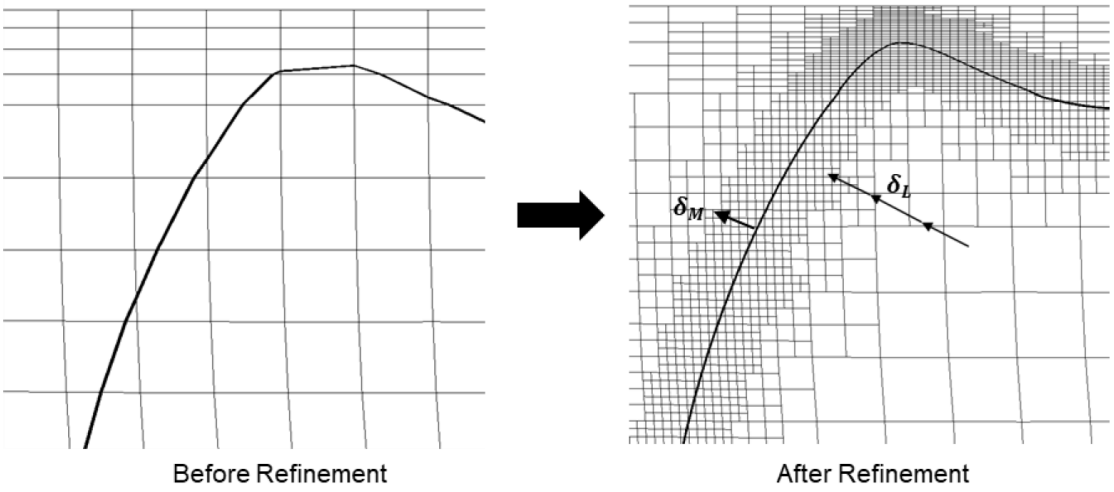

Figure 3-3: Mesh refinement illustration by Potgieter. [47] δ_M is the number of refined cells, and δ_L is the number of refinement levels.

Adaptive meshing considers both the projected error relative to the individual cell size and the specific area's gradient. For 2D, the predicted error is obtained using the following expression:

$$|e_{cell}| = (A_{cell})^{\frac{r}{2}}|\nabla f| \tag{3-25}$$

Here e is the associated error, ∇f is the Euclidean norm of the adaption metric gradient, r is the gradient volume weight, and A_{cell} is the area of the cell. From Equation (3-25) it should be noted that the gradient and cell area influence the expected error. Additionally, the gradient cannot be altered without influencing the solution. Since the objective of adaptive meshing is to minimize this error, the most effective solution is thus to reduce the cell area. ANSYS Fluent uses many different variables as the criterion for reducing this error such as temperature, pressure etc. However, the two-phase region is the focal point of this study and therefore the volume fraction, specifically the volume fraction gradient, is implemented as the parameter. As mentioned in Section 3.2.1, the mass transfer is smeared over a few cells on both the liquid and vapour side of the interface. To assist with this smearing, the user-defined function (UDF) ensures that the mesh refinement produces enough refined elements on either side of the interface. Potgieter [47] found that the optimal quantity of refined elements along both sides of the interface which will ensure accurate predictions of the heat transfer coefficient and bubble interface was at least four. An example of the refined cells is illustrated by the δ_M arrow in Figure 3-3 which shows four to five small cells on either side of the interface (solid black curve). Additionally, Potgieter found that the ideal number of refinement levels before becoming too computationally expensive is three, which is illustrated by the δ_L arrow in Figure 3-3.

Other than mesh count, it is also important to consider the mesh quality. Mesh quality is a way of ensuring that the physics are modelled accurately between the cells. Properties such as skewness and cell aspect ratio (AR) are often used to quantify the mesh quality. These properties are applicable for both structured and unstructured grids as they address how well

the data is shared over the elements. For example, long elements ($AR < 1$) or tall elements ($AR > 1$) may result in important physics being missed and assumed constant. It is therefore desirable that the aspect ratio be 1. In boundary layers near walls where inflation layers are often used, large aspect ratios arise. It is generally believed that a good quality mesh has an aspect ratio lower than 5 for at least 90% of its cells. The skewness tests how different the current cell is to an equilateral cell with the same volume [51]. For structured meshes with square or rectangular elements, the skewness would be zero.

3.3 DISCRETIZATION METHODS AND SOLUTION PROCEDURE

The discretization methods refer to how the functions in the solution space are divided. So far, the spatial discretization of the governing equations has been discussed above by looking at meshing. However, some variables in these equations are temporal derivatives and not just spatial derivatives. Therefore, specific schemes are required to solve both the temporal and spatial derivatives in the governing equations.

Firstly, the specific solver should be selected for the simulations. Here the pressure-based solver was selected over the density-based solver due to the low flow rate and incompressibility of the study. The PRESTO! (PREssure STaggered Option) scheme was implemented to calculate the pressure field by utilizing a discrete continuity balance which calculates the local face pressure at each cell.

Once the continuity equation is satisfied, the PISO (Pressure-Implicit with Splitting of Operators) method is implemented to couple the velocity and pressure fields. This is a predictor-corrector scheme which reformats the continuity equation and ensures the balancing of both the momentum and continuity equations.

The spatial gradients are computed utilizing second-order techniques. The gradient of the volume fraction is determined using a second-order implicit approach whereas second-order upwind schemes are employed for the momentum and energy equations. As previously discussed, the VOF interface is represented as a normal unit, and as a value between 0 and 1. The advection equation is used to propagate the VOF interface before it is constructed as a sharp interface. The compressive scheme is utilized to reconstruct the sharp interface by obtaining the volume fractions across all cell faces during each propagation step. This high-resolution second order scheme incorporates spatial gradients, donor values, and cell face values to reconstruct the VOF interface. Furthermore, the VOF model incorporates an implicit body force in the momentum equation that considers the pressure gradients and interactions between the two phases.

A first-order implicit time-stepping technique is used to progress the simulation in time. At each time-step the momentum, continuity, volume fraction, energy, and other scalar equations are calculated and iterated until a convergence criterion is met. All equations, except for the energy equation, adhere to a convergence criterion of 1E-04, whereas the energy equation is subject to a criterion of 1E-06. The time step size is obtained using the Courant-Friedrichs Lewy number (CFL) [52] which is defined by the following equation for one-dimension (1D):

$$CFL = \frac{u\Delta t}{\Delta x} \tag{3-26}$$

However, for applications in higher dimensions such as two-dimensional (2D) and three-dimensional (3D) studies, the simulation progresses in numerous dimensions meaning that the time step size is influenced by these various dimensions. The CFL number for various dimensions is defined by:

$$CFL = \Delta t \left(\sum_{i=1}^{n} \frac{u_i}{\Delta x_i} \right) \tag{3-27}$$

Here Δt is the time step size, u is the velocity, and Δx is the spatial step length. The subscript $i = 1, 2, \dots, n$ indicates the specific dimension. The CFL number relates the propagation of information to the spatial and temporal discretization of the numerical method. Typically, in flow boiling cases where small disturbances in the flow matter, a $CFL < 1$ is required to guarantee that the solution is accurately represented, and that the solution remains stable. A CFL value of unity means that the information will cover the entire length of the element per time-step. It should then be clear that selecting a CFL number that is too small will result in the solution taking longer to solve, while a CFL number that is too large may result in crucial information being missed or solution stability being jeopardized. A $CFL = 0.25$ was initially selected based on the work done by Potgieter [47] however, this was later adjusted by selecting a fixed time step size to obtain the desired solving time while still ensuring stable and trustworthy results. This step size resulted in a CFL number ranging from 0.0016 to 0.47.

The following steps were performed during the initialization process:

1. First, a steady-state, single-phase case is performed to initialize the velocity, pressure, and temperature profiles.
2. Next, a transient case is performed which patches an initial bubble into the domain.
3. The bubble temperature, pressure, and velocity are then initialized. To account for surface tension forces, the pressure inside the bubble is set marginally higher than the surrounding fluid pressure. The saturation temperature is used for the bubble temperature and the bubble velocity is set to a constant value based on the surrounding fluid.
4. All equations are turned off which is followed by a single iteration. This helps to start the calculation process and ensure stability.
5. Activated one at a time, the adjust functions are resolved with a single iteration. This guarantees that the scalar variables are initialized with an initial value for use in the solution procedure. If this is not followed or a value does not exist, then ANSYS Fluent flags an error, and the initialization procedure needs to be reinitiated.
6. The final three scalar variables are initialized once all the adjust functions are activated and the scalar equations are initiated. This is accomplished by applying the energy and mass source terms, followed by solving a single iteration.
7. Finally, the relevant equations are reactivated, such as the volume fraction, momentum, energy, and scalar equations. This finalizes the initialization process which is then followed by the solution being calculated.

During the solution process, the following procedure is used by ANSYS Fluent 23R1 and the UDF:

1. In each iteration, the adjust functions are calculated in the order of implementation in the UDF.
2. Next, the smeared source term is computed, yielding the energy and mass source terms.
3. The momentum equation is then solved.
4. The velocities are then updated by solving the mass continuity equation.
5. The equation for the volume fraction is evaluated.
6. The solving of the energy equation is performed.
7. The mesh adaption and the mass transfer terms are then obtained by solving the scalar equations.
8. The domain properties are then revised.
9. And then the residuals for the convergence criteria are checked. If these are not met, the next iteration begins, and the process starts again at Step 1. Once the criterion is met, the solution is said to be sufficiently converged, allowing the solution process to advance to the next time-step.

3.4 Benchmark Tests

Benchmark tests are necessary to verify that the evaporation model implemented by the UDF performs as it should. To investigate whether the UDF is working as expected, an axisymmetric case that was also considered by Potgieter [47], Magnini et al. [53], and Ferrari et al. [54] was performed. The domain used is illustrated in Figure 3-4 below.

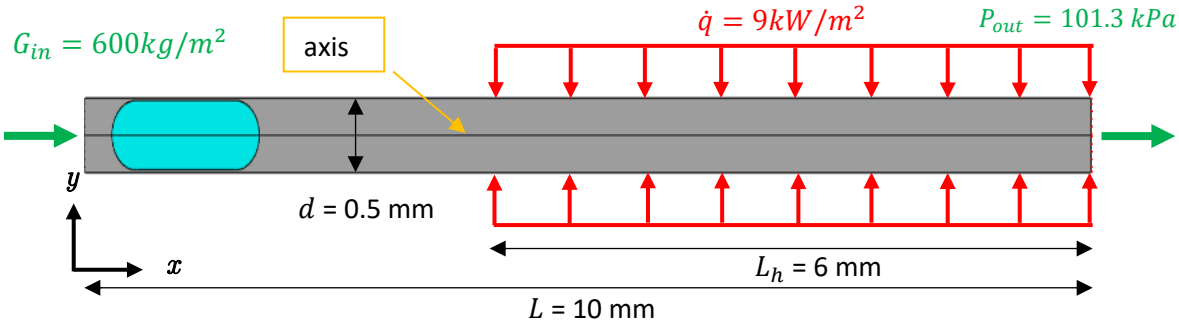

Figure 3-4: Axisymmetric domain with vapour slug initiated near inlet.

The case uses a 10 mm long axisymmetric domain with a diameter d = 0.5 mm, a 4 mm long adiabatic region and a 6 mm long heated region. The heating is applied using a constant heat flux of 9 kW/m². A uniform mass flux of 600 kg/m² was used at the inlet while a standard pressure outlet was used for the outlet. A steady state simulation is conducted, as described by the initialization steps in section 3.3, which obtains the temperature and velocity profiles required to run the transient simulation. A vapour slug is then patched into the adiabatic region 0.5 mm from the inlet with a 1.5 mm by 0.464 mm cylindrical body and semi-circular end caps. A transient simulation is run using adaptive time stepping for a total flow time of

12.5ms. The working fluid used is refrigerant R113 and its properties are illustrated in Table 3-1 below.

Table 3-1: Fluid Properties of R113 (from Potgieter [47])

Property	***Symbol***	***Dimensions***	***Value***
Saturation Temperature	T_{sat}	K	323.15
Saturation Pressure	P_{sat}	kPa	109.7
Latent heat of Vaporization	h_{lv}	J/kg	143 500
Density (Liquid)	ρ_l	kg/m^3	1 502
Density (Vapour)	ρ_v	kg/m^3	8
Viscosity (Liquid)	μ_l	Pa.s	477 x 10^{-6}
Viscosity (Vapour)	μ_v	Pa.s	10.4 x 10^{-6}
Conductivity (Liquid)	k_l	W/m.K	63.2 x 10^{-3}
Conductivity (Vapour)	k_v	W/m.K	9.62 x 10^{-3}
Specific heat (Liquid)	$c_{p,l}$	J/kg.K	943
Specific heat (Vapour)	$c_{p,v}$	J/kg.K	695
Surface tension	σ	N/m	14.4

The fluid properties remain constant during the entire simulation. In each of the studies, the vapour slug location is tracked throughout the simulation with Figure 3-5 below illustrating our results at four timestamps; 0 ms, 3 ms, 8 ms, and 12.5 ms.

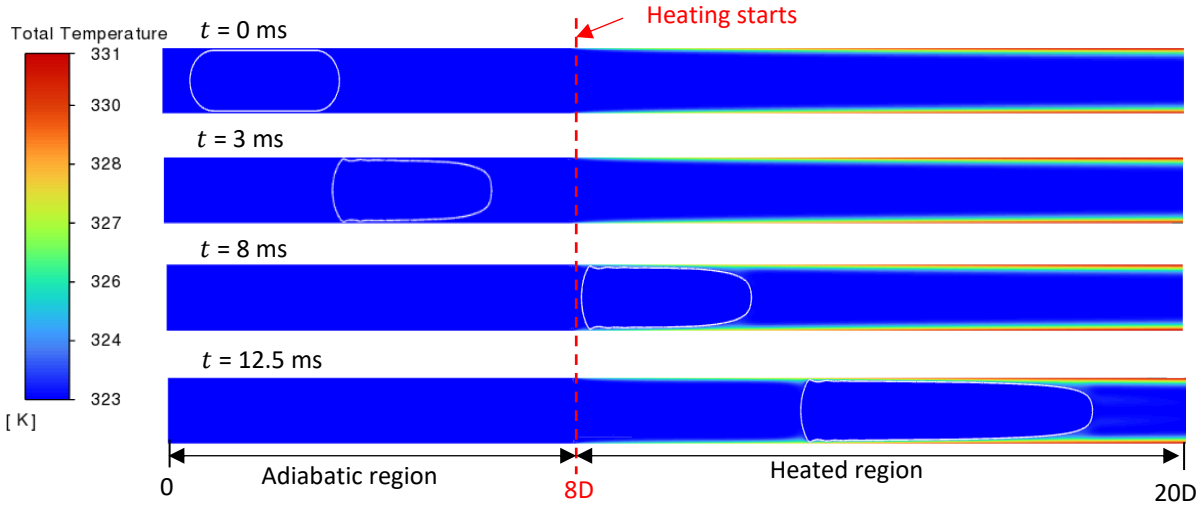

Figure 3-5: Temperature distribution and bubble location (indicated by the white line) at different flow time intervals.

The four timestamps show the bubble in its initial position, before it enters the heated region, once it's completely in the heated region, and at the end of the simulation. The vapour slugs stretched into a bullet-like shape as expected from literature. The bubble growth through the domain matched well with the studies conducted by Potgieter [47], Magnini et al. [53], and Ferrari et al. [54] as shown in Figure 3-6 below.

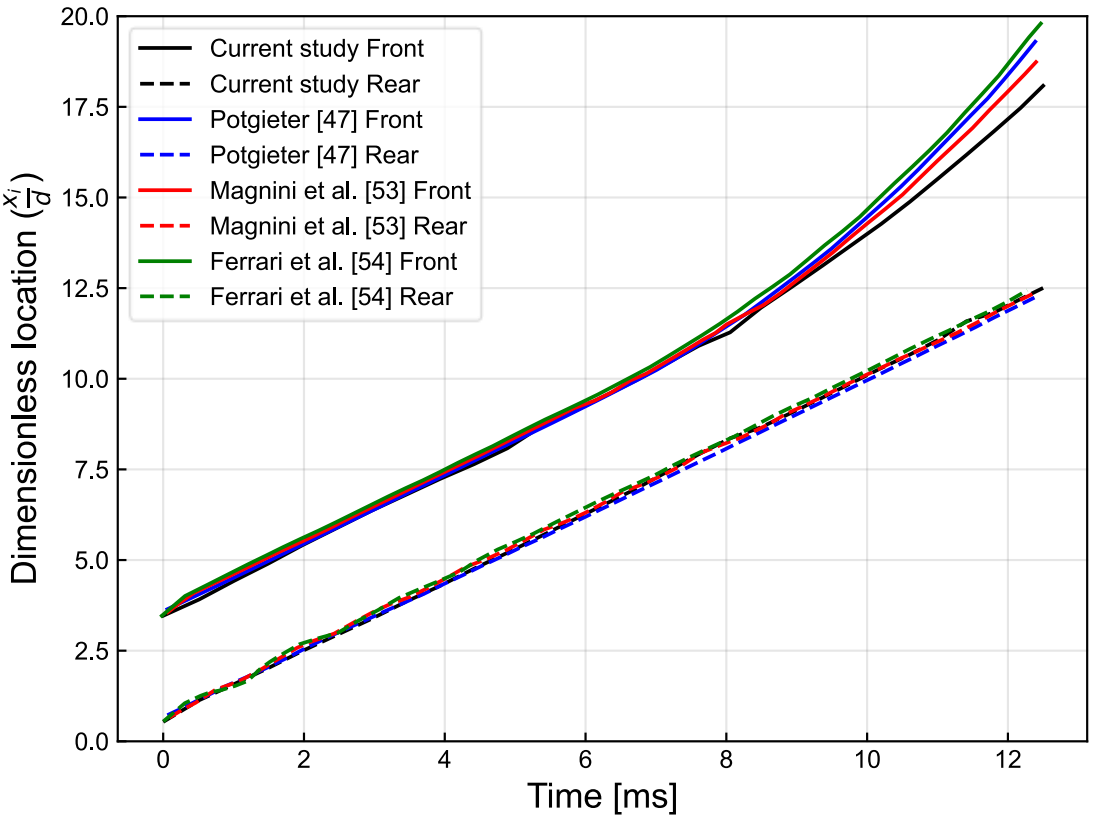

Figure 3-6: Bubble evolution along the channel length throughout the flow analysis.

The front and rear bubble locations are non-dimensionalised by dividing them by the channel diameter ($\frac{x_i}{d}$). The rear of the bubble for the current study matches well with all the other studies, however the front of the bubble grew slower than the other cases. The front of the bubble at the end of the simulation was 3.5% shorter than Magnini et al. [53], 6.3% shorter than Potgieter [47], and 8.7% shorter than Ferrari et al. [54]. With the complex nature of two-phase flow modeling, errors below 10% are desired thus deeming the current results acceptable.

Additionally, the heat transfer coefficient on the heated walls of the domain at t = 12.5 ms was compared. The results are illustrated in Figure 3-7 below.

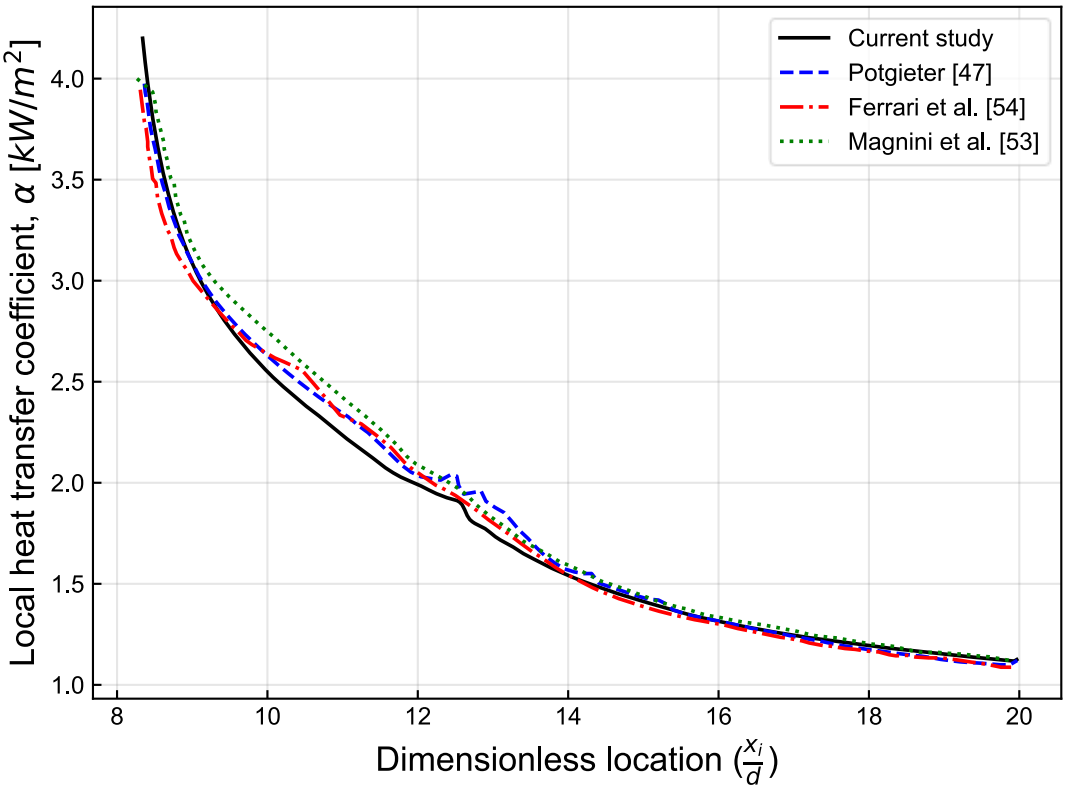

Figure 3-7: Local heat transfer coefficient distributed along the heated wall at flow time stamp 12.5 ms.

The heat transfer coefficient for the two-phase region was calculated using:

$$\alpha_{tp} = \frac{\dot{q}}{(T_s - T_{sat})} \tag{3-28}$$

Where the saturation temperature is used in place of the fluid temperature, as in Eq. (2-1), as this is done for two-phase flows [54].

The local heat transfer coefficient was observed to be the largest at the trailing edge of the vapour slug ($\frac{x_i}{d}$ = 8) where the vapour slug clogs the domain, and the surface temperature is the lowest (closest to saturation). Moving towards to leading edge of the bubble, and thus the outlet of the channel, the heat transfer coefficient reduces. This is caused by the higher surface temperatures and the thicker fluid films. The current study matches well with the other when considering the heat transfer coefficients, with a slight underprediction near the trailing edge.

The results were deemed to be accurate and therefore the model was implemented correctly.

3.5 Chapter Summary

This chapter discussed the numerical model used for the current study. The volume of fluid (VOF) method was used as the multiphase model within the ANSYS Fluent 23R1 software package. The continuum surface force (CSF) method was used to model the effects of surface tension. The evaporation model used was the modified Schrage model, also referred to as

Hardt's evaporation model [2] which was a source term-based model. The evaporation model was implemented via a user-defined function (UDF) developed in-house by Potgieter [47] for similar microchannel flow boiling studies. The implementation of this UDF was briefly discussed along with the spatial and temporal discretization methods used to solve the necessary models. Thereafter, a benchmark test was performed to validate the multiphase model, surface tension model, and evaporation model against previous studies. The results confirmed that the models and the UDF were implemented correctly.

The next chapter discusses the test case geometry used for the numerical investigation. The geometry was developed from the experimental investigation performed by Venter [3] and was simplified to 2D. The boundary conditions, fluid properties, domain meshing, and simulation settings were all included in this discussion. The chapter then ends with a validation study comparing the experimental results to some numerical results using water as the working fluid.

4 TEST CASE GEOMETRY

In this chapter, the experimental set-up and geometry used by Venter [3] in performing the pure water and self-rewetting case studies is discussed. This is important as the water case studies are used to validate the numerical model. Thereafter, the numerical domain that was used to consider the experimental case is illustrated and discussed along with the modelling approach, boundary conditions and operating conditions used. This is followed by the mesh structure and fluid properties used for the different simulations. Finally, the validation results are briefly discussed.

It is important to note that the experimental results were re-processed by Venter [3] before the submission of this dissertation. The re-processing meant that the experimental results discussed in this section differ slightly from the initial experimental results considered for the numerical model, and in some cases, certain experimental data points were deemed un-usable. The numerical model, discussed in section 4.2, was developed using the initial experimental data before the re-processing was performed. Despite this adjustment in the experimental results, the results obtained from both numerical and experimental studies were deemed to be applicable and comparable for the validation of the numerical model.

4.1 EXPERIMENTAL TEST CASE

4.1.1 EXPERIMENTAL SET-UP AND METHOD

Venter [3] experimentally investigated the flow boiling of binary and self-rewetting mixtures in high aspect ratio microchannels at various angles of inclination. A schematic of the experimental test facility is shown in Figure 4-1.

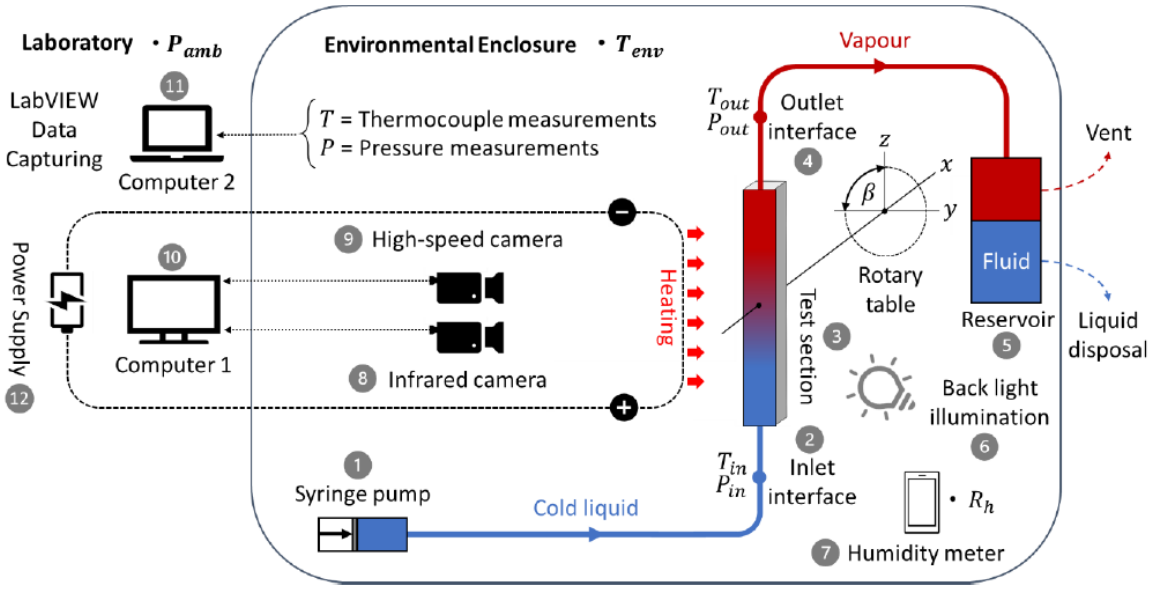

Figure 4-1: Schematic representation of the Experimental test facility [3].

The experimental study was performed in the laboratories at the University of Edinburgh in Scotland. To shelter the experiments from fluctuating temperatures in the laboratory, the test

setup was enclosed in an acrylic glass container. Fluid was pumped through the test section (3) by using a syringe pump (1) located upstream in the system. This allowed for accurate control of the inlet flow rate. The fluid in the test section was heated by applying single sided wall heating to the test section. This was achieved by electrically heating a Tantalum layer applied to the test section via a DC power supply (12) located outside the enclosure. This allowed for controlled heating to the test section by altering the voltage. Once heated, the spent fluid was then captured downstream of the test section by using a fluid reservoir (5), which vented to the atmosphere. Fluid measurements were recorded at the inlet (2) and outlet (4) of the test section with the use of thermocouples and pressure transducers. The thermocouples were used to measure the inlet temperature, saturation temperature, and to approximate the heat loss to the environment. Due to the small scale of the test section, fluid temperature measurement was not viable. The measure data from the thermocouples and the measured vapour quality was used to approximate the fluid temperature. Additional temperature measurements were conducted on the exterior heated surface of the test section by using an Infrared camera (8). Lastly, a high-speed camera (9) was used to observe the boiling of the fluids.

The test section (3) that was used was a rectangular glass borosilicate tube, and is shown in Figure 4-2.

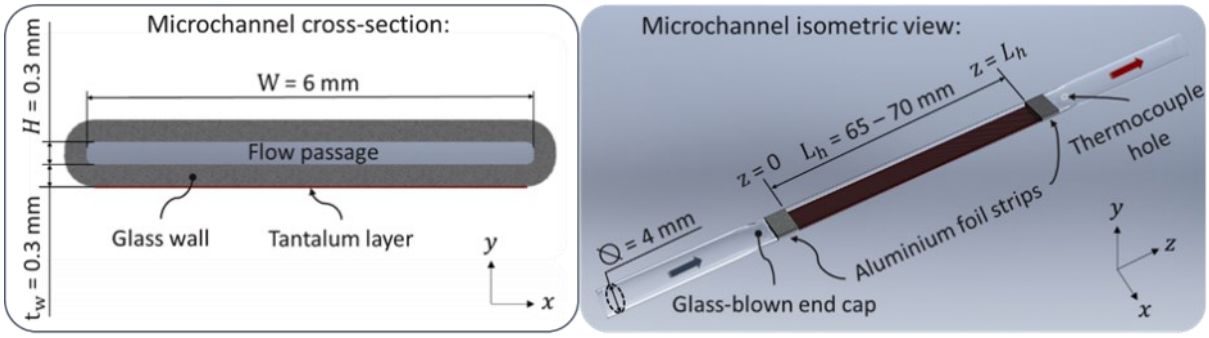

(a) (b)

Figure 4-2: Experimental test piece used by M Venter with (a) illustrating the cross-section and (b) an isometric view. [3]

A tantalum layer, approximately 11 nm thick with a surface resistivity of 120 Ω/square, was applied to the outer surface of the bottom wall of the channels, as seen in Figure 4-2(a), to enable bottom heating via an electrical current. The electrical current was supplied by the external DC power supply and sent through clamps and aluminium foils contacting the tantalum layer which, due to the high electrical conductivity of aluminium, allowed the electric current to flow through the Tantalum layer, providing single-sided, locally uniform heating.

Measuring between the aluminium foil strips, the test sections had a heated length (L_h) of 70 mm ± 0.01 mm, an inner width (W) of 6 mm ± 0.02 mm, and an inner height (H) of 0.3 mm ± 0.02 mm. The channels had a uniform wall thickness (t_w) of 0.3 mm ± 0.02 mm along the length, with a wall thermal conductivity, k, of 1.1489W/m.K. Using these

dimensions, the hydraulic diameter (D_h) and the aspect ratio were obtained using equations (4-1) and (4-2) respectively.

$$D_h = \frac{4A_c}{p} \tag{4-1}$$

$$Aspect\ Ratio = \frac{W}{H} \tag{4-2}$$

The hydraulic diameter was calculated to be 571.43 µm and the aspect ratio was 20. Furthermore, the test section had a heated length to diameter ratio of L_h/D_h = 122.5, which is important for investigating flow regimes, pressure drops, and heat transfer effects. From the literature, a hydraulic diameter of 571.43 µm is said to fall outside of the microscale classification. However, as mentioned in Section 2.1.1, dimensionless parameters such as the Laplace constant, La, are required to accurately classify the cases as microscale. This is discussed further in Section 4.3.

4.1.2 Experimental Cases

The experiments were divided into two main portions with the first comparing water, as the pure fluid, to a 5% v/v 1-butanol-water mixture (where v/v refers to a volume percentage), as the self-rewetting fluid (SRF), in a horizontally orientated microchannel with various applied heat fluxes and mass fluxes. The second portion used the 5% v/v 1-butanol-water mixture, again as the SRF, to perform an inclination study with various applied heat fluxes and mass fluxes. Only the first portion of the experiments is described further as the numerical investigation was unable to accurately model the influence of inclination. This was attributed to the short flow time experienced when modelling rapid bubble growth, hence insufficient time was available for buoyancy forces to significantly influence the numerical solution. Furthermore, only the water cases are discussed in this chapter for the validation of the numerical model.

A range of constant inlet mass fluxes (G) of 10 kg/m^{2}s, 15 kg/m^{2}s, and 25 kg/m^{2}s were investigated. However, for this study, only the 15 kg/m^{2}s cases are considered due their observed reliability by Venter [3]. Various uniform heat fluxes were applied to the bottom of the channel via the tantalum layer. The heat fluxes were regulated by adjusting the voltage output of the DC power supply. Additionally, the inlet temperatures were dictated by the average lab environmental temperature which was 24°C ± 3°C.

The experimental cases were further divided into a set of single-phase flow cases and a set of two-phase flow cases. The single-phase flow cases were used to calibrate the heat loss and heat flux characteristics. The calibration made use of the energy balance principle to compare the supplied energy to the energy absorbed by the fluid based on its temperature rise. The heat loss characteristics were very important due to the channel not being thermally insulated to allow for the capture of temperature measurements with the IR camera. Not insulating the channel resulted in energy loss to the environment in the form of heat across the top and both side walls.

Following the single-phase flow cases, the two-phase experiments were performed with which the numerical study is interested. The single-phase experiments were recorded once steady-state conditions were recorded. Similarly, the two-phase experiments officially began once quasi-steady-state conditions were satisfied with measurements recorded over a 60 second period. This was verified by visual inspection of boiling incipience as well as the bulk fluid temperatures at the outlet. Each case in either portion was performed three times to ensure that the results obtained were accurate and to reduce the impact of any external factors on the results.

During the two-phase experiments, it was observed that, on average, majority of the test section was filled with single-phase flow and only a small portion extending from the outlet consisted of two-phase flow. As the applied heat fluxes increased, the two-phase flow portion stretched towards halfway along the length of the channel. To reduce the computation time of the numerical model, discussed in Section 4.2.1, only the second half of the test sections (z = 35 mm to z = 70 mm) were considered. It then follows that only the experimental results across the second half of the test section were investigated. The test section locations z = 35 mm and z = 70 mm are therefore referred to as z = 0 mm to z = 35 mm respectively. Furthermore, it was observed that at most, the last 2.5 mm of the test sections experienced in-accurate IR-camera results shown by a temperature run-away, which is shown in the next sub-section. Because of this temperature run-away, the last 2.5 mm of the second half of the test section was not included in the results.

A total of five experimental investigations were considered in this study for validation of the numerical model. A summary of the five experimental cases investigated are shown in Table 4-1 below where only the second half of the test sections were considered excluding the last 2.5 mm:

Table 4-1: Experimental test matrix for the horizontal pure water cases where only the second half of the test section is considered.

Test Cases	***Fluid***	***Inlet mass flux [kg/m²s]***	***Saturation temperature (T_{sat})[°C]***	***Applied Average Effective heat flux across the second half of the test section [W/m²]***	***Measured Average Wall temperature across the second half of the test section [°C]***
1	Water	15	99.74 ± 0.1	19403.11	100.57
2	Water	15	99.74 ± 0.1	20767.66	102.20
3	Water	15	99.74 ± 0.1	22003.65	103.89
4	Water	15	99.74 ± 0.1	24061.97	108.86
5	Water	15	99.74 ± 0.1	25315.15	110.27

4.1.3 Experimental Wall Temperature Data

As mentioned earlier, the experimental cases applied an effective heat flux to the outer surface of the test section bottom wall and measured the heated surface temperature. The distinction between the applied parameter (effective heat flux) and measured parameter (surface temperature) is important to note due to the role it plays on selecting the boundary

conditions for the numerical model in the coming chapters. Furthermore, it was mentioned that the heat flux characteristics were obtained using the single-phase cases. The measured wall temperature data is described in this sub section to explain the experimental results. It should be noted that this sub section describes how the experimental wall temperature data is processed over the entire length of the test section and not just the second half of the test section because the data processing precedes the reduction of the results.

Throughout this section and the preceding sections, the terms time-average, width-average and area-average are used. These refer to the various methods in-which the average of the relevant data was calculated. Time-average refers to the average calculated over a time period. The width-average refers to the average calculated over the channel width to obtain a single value for each location along the length of the channel. This is necessary for relating the three-dimensional experimental data to two-dimensions. Lastly, the area-average is the average calculated over the heated surface to obtain a single value per time-instance.

The experimental data was captured using multiple thermocouples placed along the length of the channel, as well as from an IR camera measuring the surface temperature of the tantalum layer. The data capturing commenced from the onset of quasi-steady-state flow boiling conditions. The thermocouple data was captured over a 65 second period at a frequency of 100 Hz (or every 0.01 s) and the IR camera data was captured over a 60 second period at 25 fps (or every 0.04s). The datasets were averaged over the 65 and 60 second periods to obtain a time averaged value with the IR camera data requiring an additional width average. An example of the data captured by the IR camera at a specific time in the 60 second period is shown in Figure 4-3.

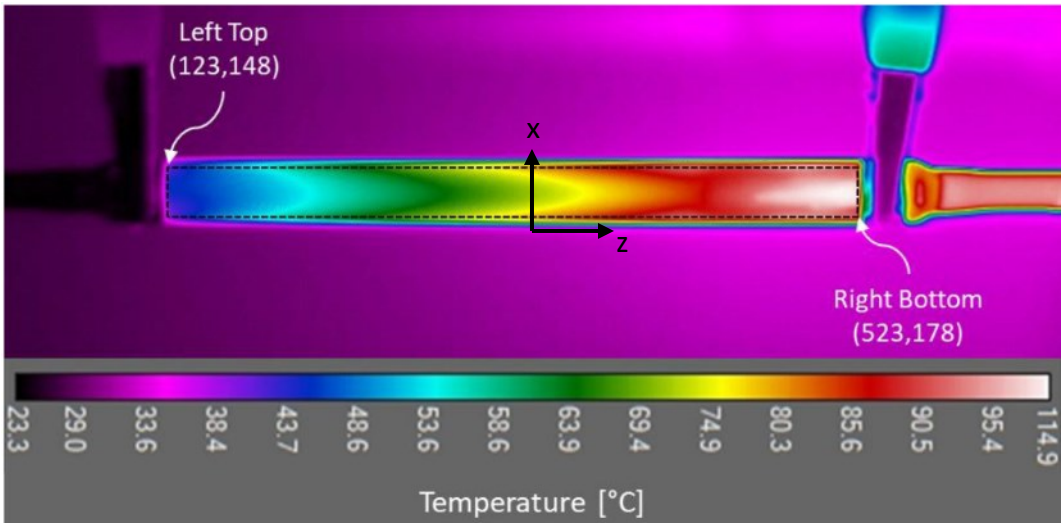

Figure 4-3: Example of the IR camera footage at a specific time step during the flow experiments [3]. The dotted lines indicated the enclosed area used for identifying the channel pixels.

To interpret and reduce the data, a grid-like structure, like that in numerical investigations, is required for the IR camera. The IR camera had a resolution of 640 x 480 pixels but the channel section, marked by the dotted box, used only 400 x 30 pixels along the length and width respectively. Therefore, 12 000 (400 x 30) data points were obtained for every time step. Each z-coordinate along the length of the channel had 30 temperature values along the width

(x-direction) of the channel. To reduce this, a width average was obtained for each z-coordinate using equation (4-3), reducing the 30 temperatures values per z-coordinate.

$$T_{s,local} = \frac{\sum_{i=1}^{N} T_{s,i}\Delta x_i}{\sum_{i=1}^{N} \Delta x_i} \tag{4-3}$$

Here the subscript $local$ represents the width-averaged value at each z-coordinate, the subscript i represents the x-location along the width of the channel, and Δx represents the distance between the points.

This reduces the temperature pixels from 12 000 to 400 for each time instant. The reduction means that over the total 60 second period, a total of 500 000 (400 x 25 fps x 60 s) spatial and temporal temperature data points were obtained. Then, for each z-coordinate along the length of the channel, the temporal data points over the 60 second period were summed together, and the average was obtained. This is known as the time-average and is described by equation (4-4):

$$T_{s_{avg,t}} = \frac{\sum_{i=1}^{N} T_{s,i}\Delta t_i}{\sum_{i=1}^{N} \Delta t_i} \tag{4-4}$$

Here the subscript avg, t represents the time-average and Δt represents the timestep between each temporal point.

The time-averaging step meant that each z-cordinate along the length of channel was represented by a single temperature value causing the data to reduce from 500 000 to again only 400 data points. Therefore, each experiment produced 400 time-averaged local surface temperatures along the heated length. Since only the second half of the channel was considered, the experimental data consisted of 200 local surface temperatures along the heated length. Figure 4-4 shows an example of the time-average wall temperature along the length of the channel for an experimental case.

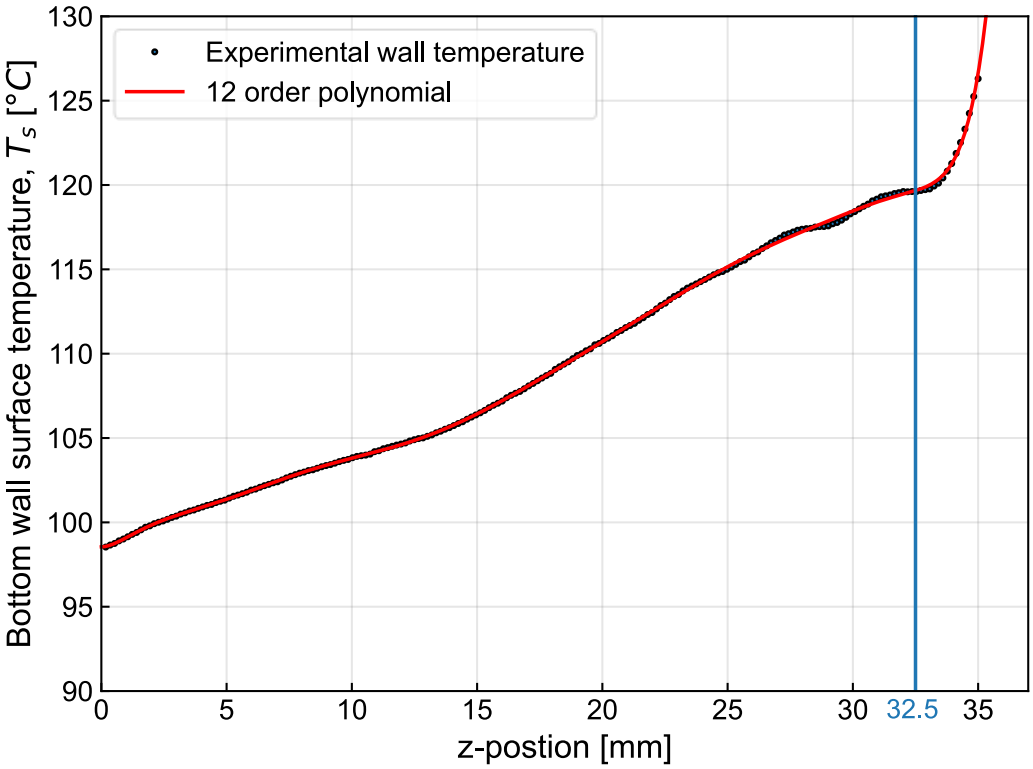

Figure 4-4: Example of the time-averaged wall temperature along the length of the channel. The black dots represent the experimental data reduced from the IR camera while the red line represents the temperature profile implemented as the heating boundary condition. The blue line indicates the cut-off of the data used.

The black dots in Figure 4-4 represent the measured, and reduced, IR camera data for a specific water case. The red line represents the 12th order polynomial used to implement this surface temperature data into ANSYS Fluent as the heated wall boundary condition described in section 4.2.1. As mentioned in Section 4.1.2, the experimental results were not deemed accurate across the last 2.5 mm of the domain as illustrate by the temperature run-away to right of the blue line. Because of this, last 2.5 mm of the experimental results were removed and only 32.5 mm of the second half of the test section was considered (0 mm to 32.5 mm). To further process the temperature data to get a single area-average surface temperature for the specific case, equation (4-5) would be used:

$$T_{S_{avg,A}} = \frac{\sum_{i=1}^{N} T_{s,i} \Delta A_i}{\sum_{i=1}^{N} \Delta A_i} \tag{4-5}$$

Here the subscript avg, A represents the area-averaged quantity and ΔA represents the incremental area between data points. However, since the surface temperatures have already been reduced to a one-dimensional array, this incremental area can be described as the distance between the points along the length of the channel.

4.2 Numerical Model And Approach

The goal of the validation study is to prove that the numerical model accurately models real world investigations. Therefore, by modelling the experimental investigations conducted by Venter [3], it is expected that the numerical model should produce similar results. It is

extremely important that the domain and boundary conditions accurately depict the real-world conditions.

As mentioned previously, the experimental results were re-processed prior to the submission of this study. This sub section briefly discusses why the re-processing of the experimental data did not impact the validity of the numerical investigation and thus the validation results.

4.2.1 Domain and Generic Boundary Conditions

The numerical domain is based on the experimental case study discussed in section 4.1. Figure 4-5 below illustrates the experimental test section (a) and how it was sectioned for the 2D simulations (b).

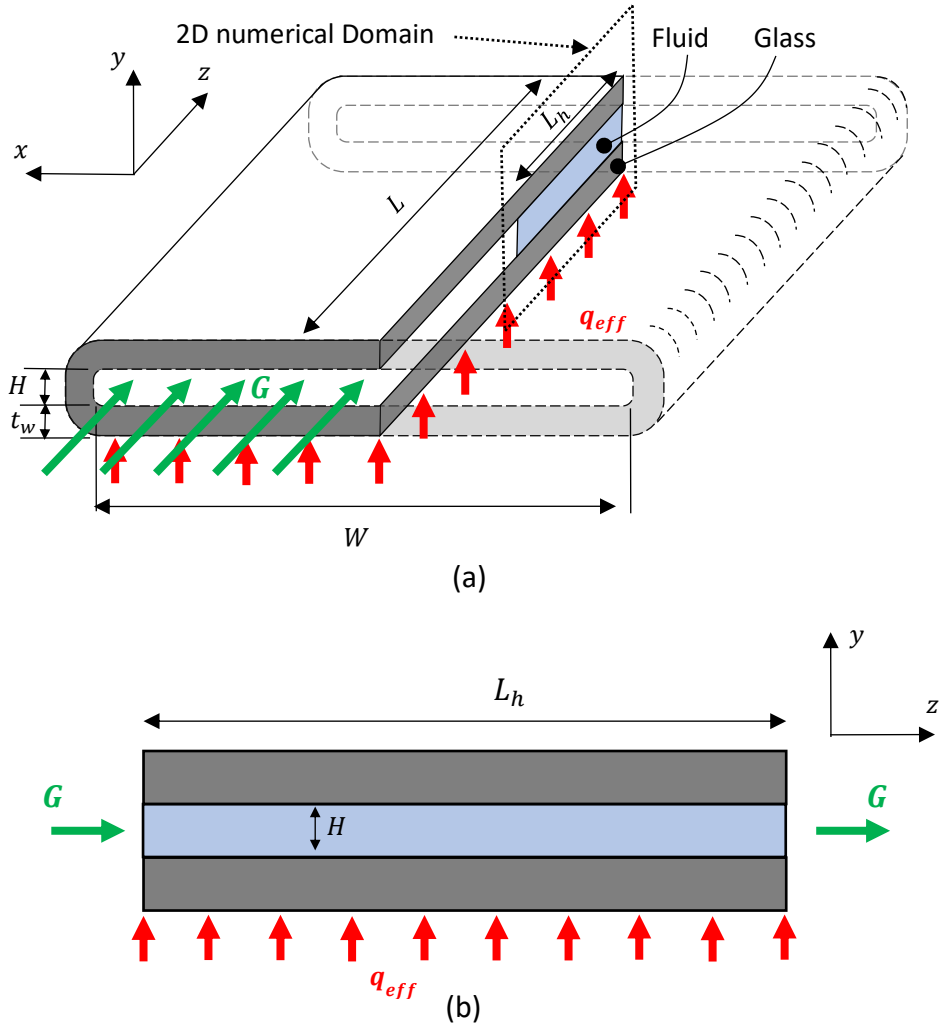

Figure 4-5: (a) 3D representation of the experimental test section; (b) 2D numerical domain simplification.

The numerical domain was developed from the experimental test tubes. From the experimental investigation it was clear that large vapour slugs filled the domain, therefore vapour slugs are investigated in the numerical study. To perform the two-dimensional (2D) simulations, a section of the test channel along its centre, parallel to the z-y plane was taken. This runs along the length of the channel, and through the centre of the width of the channel.

As discussed in Section 4.1.2, only the second half of the test sections, with length L_h = 35 mm, were investigated due to the absence of two-phase flow in the first half of the test sections. For the remainder of Section 4, only the second half of the test section is considered. It then follows that the original test section locations z = 35 mm and z = 70 mm are now referred to as z = 0 mm and z = 35 mm respectively as mentioned in Section 4.1.2.

It should be noted that in Figure 4-5(b), only the fluid domain, denoted by the height H = 0.3 mm and length L_h = 35 mm, was simulated because adding additional solid domains (wall thickness) in ANSYS Fluent resulted in complications with the UDF. The addition of the wall thicknesses was also deemed unnecessary as it would not have a significant impact on the growth of the bubbles. Instead, it was possible to implement a wall thickness at the heated surface as a boundary condition which allowed 1D heat conduction, thus more accurately predicting the heat transfer to the fluid through the glass.

BOUNDARY CONDITIONS

Selecting the correct boundary conditions are essential. Implementing the wrong boundary conditions could greatly alter the results of the simulation or jeopardize the stability of the simulation. At the inlet, a constant uniform mass flux and fluid temperature was applied. As previously mentioned, a mass flux of 15 kg/m²s was selected as it was noticed to have the most stable experiments with the least uncertainty in general. Using these cases, the temperatures ranged from 68.1°C to 79.1°C.

The experimental fluid temperature inside the channel was predicted due to the limited access. Using the predicted fluid temperature, the inlet temperature to the domain was obtained by observing the temperature halfway along the length of the test channel.

The inlet mass flux can also be translated into a constant mass flow rate ($\dot{m}$) and a constant, uniform inlet velocity (u) using Equations (4-6) and (4-7) respectively:

$$\dot{m} = G \times A_c \tag{4-6}$$

$$u = \frac{G}{\rho} \tag{4-7}$$

The equivalent mass flow rate and inlet velocity for both the numerical domain and the experimental study is shown in Table 4-2:

Table 4-2: Fluid inlet mass flux, mass flow rate, and velocity comparison.

Property	***Experimental (3D)***	***Numerical (2D)***
Mass Flux, G [kg/m²s]	15	15
Mass Flow Rate, $\dot{m}$ [kg/s]	2.7 x 10^{-5}	4.5 x 10^{-3}
Velocity, u [m/s]	0.015	0.015

Table 4-2 indicates that the mass flow rate between the experimental and numerical domains differ. This difference is attributed to the inlet cross-sectional area used for either calculation.

In 2D simulations, the inlet cross-sectional area (A_c) is calculated using the height of the domain and multiplying it with a unit width, whereas the experimental case used the channel width of 6 mm. As mentioned previously, the Reynolds number (Re) is an important parameter in flow studies, which is dependent on the fluid velocity. Since the fluid velocity is the same for the experimental and numerical investigations, the difference in mass flow rate does not pose a significant issue for the analysis.

The outlet boundary condition was a pressure outlet set at atmospheric pressure as the experimental studies had an air vent downstream open to atmospheric conditions.

As described in 4.1.2, due to energy losses to the environment, the heating applied to the external bottom wall would be better described by an effective heat flux. However, to accurately model this heating, a profile for the heat flux is required but is not known. Instead, the exterior surface temperature measured by the IR camera was used to apply the heating by implementing a temperature profile. The temperature profile was implemented with a thermal wall thickness of 0.3 mm, meaning that a theoretical wall thickness was applied to the equations and not to the actual domain. The theoretical wall thickness used existing material properties for glass borosilicate in ANSYS Fluent which had a thermal conductivity of k = 1.1489 W/m.K. ANSYS Fluent makes use of polynomial functions to implement temperature profiles and thus a 12th order polynomial was used to describe the measured wall temperatures. The data reduction technique used to model this temperature profile was discussed further in section 4.1.3. Using a surface temperature profile instead of a heat flux for the applied heating means that the effective heat flux becomes the measured quantity with which the results are compared.

A total of six cases were numerically investigated, illustrated in Table 4-3, as opposed to the five experimental cases shown previously in Table 4-1. The extra case (test case 6) was conducted based on the initial experimental results before the re-processing of the experimental results. The re-processed experimental data from Table 4-1 is represented in the grey-shaded column below.

Table 4-3: Numerical test matrix for the horizontal pure water investigation used for the validation study.

Test Cases	***Fluid***	***Applied Inlet mass flux [kg/m²s]***	***Applied Inlet fluid temperature [°C]***	***Saturation temperature (T_{sat})[°C]***	***Measured Average Experimental Wall temperature [°C]***	***Average Applied Wall temperature [°C]***
1	Water	15	70.0	99.1 ± 0.48	100.57	100.44
2	Water	15	72.5	99.5 ± 0.48	102.20	102.1
3	Water	15	74.2	99.9 ± 0.48	103.89	103.79
4	Water	15	77.5	100 ± 0.48	108.86	108.74
5	Water	15	79.1	100.1 ± 0.48	110.27	110.14
6	Water	15	68.1	100.1 ± 0.48	N/A	97.89

Table 4-3 illustrates the numerical test cases investigated in this chapter. The average applied wall temperatures in the last column were used as the heated wall boundary condition by implementing a 12-th order polynomial as discussed above. These applied wall temperature average values differ by no more than 0.15°C from the re-processed experimental wall temperatures measured by the IR-camera (shaded in grey). Furthermore, the measured saturation temperature used for the numerical study was 100°C due to the varying measured saturation temperatures, whereas the re-processed data measured the saturation temperature as a constant 99.74°C for all cases. The small discrepancy between the applied numerical wall temperature profiles and the re-processed measure experimental wall temperatures meant that the numerical results were still applicable for validation. Additionally, the difference in saturation temperature was considered negligible for the validation. However, after the re-processing of the experimental data, it was noted that the experimental results for test case 6 were deemed unusable due to inaccurate IR-camera measurements. The numerical results for test case 6 were thus not used for comparison but rather to further the validation trend.

4.2.2 Numerical Approach

Using the numerical domain and generic boundary conditions above, the simulations were divided into two portions. In the first portion, a single-phase steady-state simulation was performed to determine the fluid velocity and temperature profiles. Using these profiles, a transient simulation was conducted for the second portion. The velocity and temperature profiles from the single-phase simulation were used as initial conditions for the transient simulation. They were also used to identify the ideal location in the domain wherein to patch a vapour bubble. During the transient simulation, the bubble was allowed to grow in order to investigate its effects on the wall temperature. The measured wall temperature and wall heat flux values were then compared to the quasi-steady-state results from the experiments.

Finding the ideal location to patch the bubble is necessary to ensure the success of the modelling of bubble growth. This is because the VOF method only models phase change when the bubble interface is in-contact with saturated fluid, meaning that the entire bubble needs to be in a region of saturated temperature. To represent this location graphically, the bulk fluid temperatures during the single-phase steady-state simulation and the flow boiling transient simulation are illustrated in Figure 4-6.

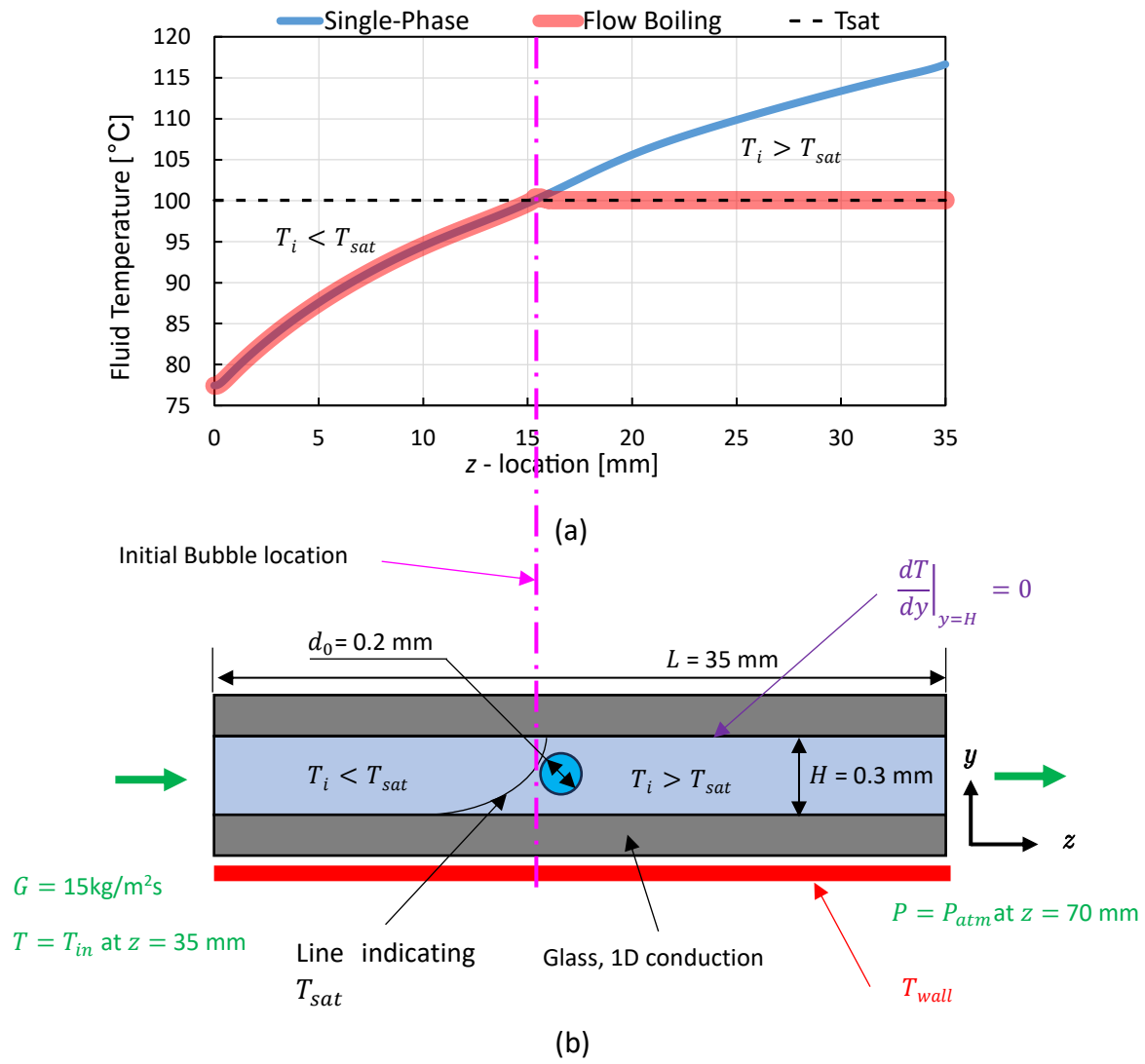

Figure 4-6: (a) Bulk fluid temperature vs z-location; (b) 2D numerical domain with initial bubble patch location.

Figure 4-6(a) shows the bulk fluid temperature along the z-location of the channel during the single-phase (blue line) and at the end of the flow boiling (red line) simulations. The black dashed line indicates the saturation temperature of the water. From the single-phase steady-state simulation, the bulk fluid temperature rises over 15°C above the saturation temperature along the length of the channel, which is expected as the simulation does not yet allow phase change. However, once phase-change was enabled, the simulated boiling process would enforce fluid temperatures near the fluid saturation temperature, as indicated by the red line. The dashed pink line indicates where the bulk fluid temperature reaches saturation temperature. This also represents the location where the initial bubble is patched to ensure phase change and bubble growth.

Figure 4-6(b) illustrates the location of the initialized bubble in the domain. The pink dashed line passes through a solid black curve in the domain which represents the points in the fluid that are equal to the saturation temperature. To the left of this curve is fluid below saturation temperature, and to the right is fluid above the saturation temperature. It should be noted

that the dashed pink line indicating the location where the bulk fluid temperature is equal to the saturation temperature, includes fluid below the saturation temperature near the upper wall of the domain. For this reason, both the bulk fluid temperature and the saturated line were used to place the bubble. The bubble was placed slightly to the right of the pink line in a completely saturated zone.

Additionally, the bubble patched was a 0.2 mm diameter bubble. This diameter was selected as it would replicate the bubble just before confinement and would result in shorter solution times than a smaller initial bubble.

4.3 Fluid Property Modeling

4.3.1 Experimental

The properties of pure water are readily available and were used to model the working fluid. However, even though the 5% v/v 1-butanol-water cases were not investigated in this section, they are briefly discussed in the next section (Chapter 5). For this reason, the methods used by Venter [3] to obtain the mixture fluid properties are briefly discussed here.

To accurately interpret the experimental results for the self-rewetting fluid, the fluid properties need to be accurately modelled. Based on the first law of thermodynamics, the linear ideal mixing rule was used to approximate the SRF properties. To describe this method, the temperature dependent fluid properties for pure water and pure 1-butanol are used. Firstly, the substance mass values were calculated from the relevant volumes and densities:

$$m_i = \rho_i V_i \tag{4-8}$$

Here the subscript i represents either the solute (the 1-butanol) or the solvent (the pure water).

Next, the total number of moles that were present in the mixture was calculated by adding the number of moles of the solute to the number of moles of the solvent used:

$$n_{mix} = n_{solute} + n_{solvent} \tag{4-9}$$

$$n_i = \frac{m_i}{M_i} \tag{4-10}$$

Here n is the number of moles and the subscript i again refers either the solute or the solvent.

Using the total number of moles, the molar fraction (η) of the substance is obtained by using the following equation:

$$\eta_i = \frac{n_i}{n_{mix}} \tag{4-11}$$

Finally, the mixture properties were approximated by multiplying the molar fraction with the specific property of each substance and adding them together. The equation below uses the specific heat, c_p, as an example:

$$c_{p,mix} = \eta_{solute} c_{p,solute} + \eta_{solvent} c_{p,solvent} \tag{4-12}$$

Due to the little available data on 1-butanol-water mixtures, the preceding method was deemed the best approach, albeit conservative, to remain consistent throughout the experiments. The fluid properties for the pure water and the 5% v/v 1-butanol-water mixture (SRF) as obtained by the ideal mixing rule are given in Table 4-4:

Table 4-4: Temperature dependent fluid properties for pure water investigated by Venter [3].

Physical Property	***Symbol***	***Units***	***Pure Water***	***5% v/v 1-Butanol-Water***
Molecular formula	-	-	H_2O	$C_4H_{12}O$
Molar mass	M	g/mol	18.015	92.138
Liquid density (at 25°C)	ρ_l	kg/m³	997.05	995.06
Liquid dynamic viscosity (at 25°C)	μ_l	kg/m.s	0.00089	0.000907
Liquid surface tension (at 25°C)	σ	N/m	0.072055	0.0716
Liquid specific heat capacity (at 25°C)	$c_{p,l}$	J/kg.K	4181	4163
Liquid thermal conductivity (at 25°C)	k_l	W/m.K	0.6065	0.6019
Saturation temperature (at 101.325 kPa)	T_{sat}	°C	99.74 ± 0.1	93.5 ± 0.1
Vapour density (at T_{sat})	ρ_v	kg/m³	0.5977	0.68
Latent heat of vaporization (at T_{sat})	h_{lv}	kJ/kg	2256.472	2239.46

The green column in the table represents the fluid properties of pure water which are of interest in this chapter. The table indicates that the fluid properties differ by less than 2% for most properties at 25°C. However, as the fluid temperature increases towards saturation temperature, the difference in fluid properties such as density increase. This difference is caused mainly by the lack of available fluid properties for 1-butanol at higher temperatures. Another property that differs by a margin greater than 2% is the saturation temperature (highlighted in green). This is important to note as the saturation temperature was not calculated using the linear ideal mixing rule but rather obtained from experiments. It should also be noted that the measured saturation temperature for the 5% v/v 1-butanol-water was 100.14°C before the re-processing of the experimental data. With the calculated properties above, the dimensionless parameters for the microchannel classifications were obtained and represented as follows:

Table 4-5: Microchannel classification dimensionless parameters calculated by Venter [3].

Dimensionless Number	*Symbol*	*Equation Number*	*Pure Water*	*5% v/v 1-Butanol-Water*
Laplace constant	La	(2-3)	0.00272	0.00268
Confinement number	Co	(2-4)	4.75	4.69
Bond number	Bo	(2-6)	0.044	0.045
Eötvös number	$Eö$	(2-5)	891.2	870.13

Again, the green column indicates the parameters for pure water which is the working fluid in this section. As mentioned in the previous chapter, the various dimensionless parameters illustrated in Table 4-5 are used to help with the channel classification. From Table 4-5, it is observed that microscale physics were at play because the threshold values of La > 571.43 x 10^{-6}, $Co \geq 1$, $Bo < 0.05$, and $Eö > 1$ are not exceeded in the case of pure water, thus classifying the test sections as microchannels.

4.3.2 NUMERICAL

The VOF method in ANSYS Fluent implemented the liquid phase and vapour phase as two separate fluids in the domain. Each phase made use of constant fluid properties at saturation temperature. The fluid properties used in the numerical investigation were obtained at a fluid temperature of 100°C and pressure of 101.325 kPa and are shown in Table 4-6.

Table 4-6: Numerical fluid properties for Pure water

Property	*Symbol*	*Units*	*Water*
Saturation temperature	T_{sat}	°C	100
Liquid density (at T_{sat})	ρ_l	kg/m3	958.2
Vapour density (at T_{sat})	ρ_v	kg/m3	0.6010
Liquid viscosity (at T_{sat})	μ_l	Pa.s	281.2 x 10^{-6}
Vapour viscosity (at T_{sat})	μ_v	Pa.s	12.24 x 10^{-6}
Liquid-specific heat (at T_{sat})	$c_{p,l}$	J/kg.K	4215.8
Vapour-specific heat (at T_{sat})	$c_{p,v}$	J/kg.K	2080.6
Liquid conductivity (at T_{sat})	k_l	W/m.K	677.3 x 10^{-3}
Vapour conductivity (at T_{sat})	k_v	W/m.K	24.6 x 10^{-3}
Latent Heat of vaporization (at T_{sat})	h_{lv}	J/kg	2256.5 x 10^{3}
Surface tension (at T_{sat})	σ	N/m	58.9 x 10^{-3}

The surface tension was the only temperature dependent fluid property and was implemented using the general polynomial form:

$$\sigma(T) = C_2T^2 + C_1T + C_0 \quad (4\text{-}13)$$

Here C_0, C_1, and C_2 are polynomial coefficients. The three coefficients for the pure water are shown in Table 4-7.

Table 4-7: Polynomial coefficients describing the temperature dependent surface tension of pure water.

Fluid	C_0	C_1	C_2	R^2
Pure water	0.0757722228	-1.43395295E-04	-2.49482313E-07	1

4.4 Initial Flow Conditions

The initial flow conditions refer to the first portion of the simulation, which is the single-phase steady-state simulation. As a reminder, this portion is crucial to the success of the transient, two-phase simulation as it ensures that the fluid velocity and temperature profiles are developed.

4.4.1 Domain and Refined Boundary Conditions

The domain mimics that described in Figure 4-6(b). It is a 2D domain with one-sided heating applied by a constant, non-uniform wall temperature as determined by the experiments. Figure 4-7 shows this in detail.

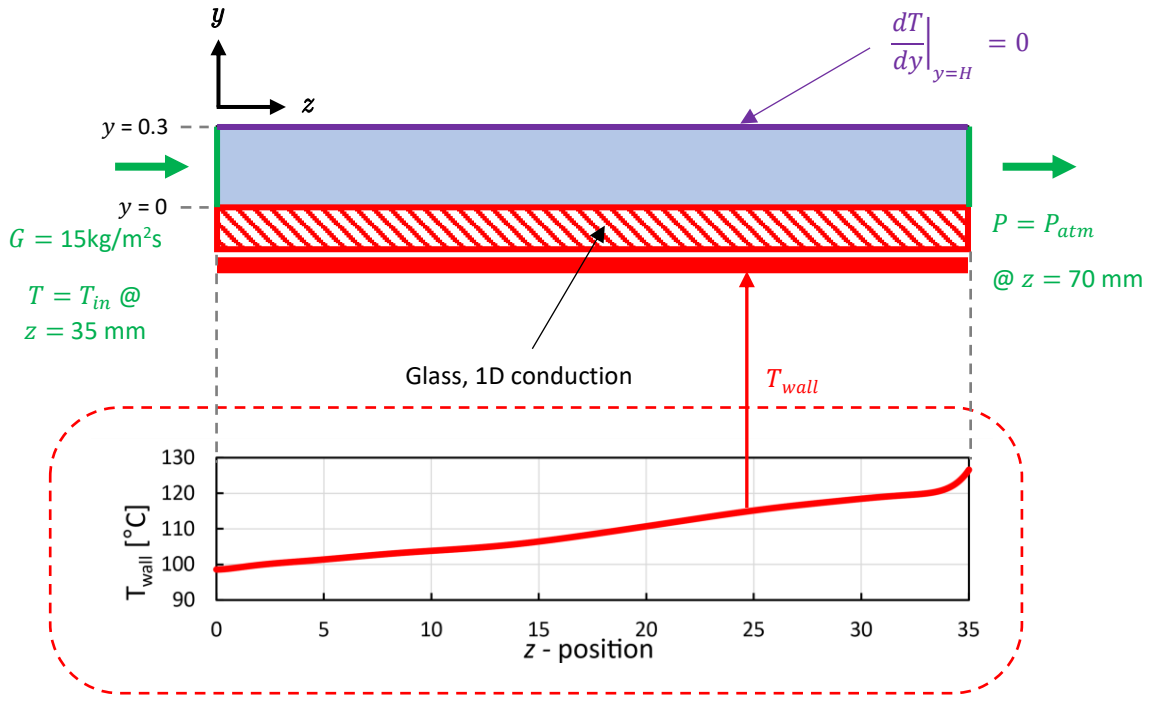

Figure 4-7: 2D representation of the Initial single-phase, steady-state flow study.

The 2D domain mimicked the second half of the test section with an overall length of 35 mm and a height of 0.3 mm. At the inlet, a constant mass flux (G) of 15 kg/m^{2}s was used with an inlet temperature equal to the predicted experimental bulk fluid temperature at z = 35 mm. This inlet temperature ranged from 68.1°C to 79.1°C. The outlet was defined by a pressure

boundary condition set at atmospheric pressure. The top wall was set as an adiabatic ($\left(\frac{dT}{dy}\right|_{y=H}$ = 0) wall condition. Heating was applied to the bottom wall via a constant, non-uniform temperature profile defined by a 12-th order polynomial, as illustrated by the temperature graph circled with red dashed lines. The bottom wall condition also made use of a theoretical wall thickness by using 1D conduction with a thermal conductivity, k, of 1.1489 W/m.K, as obtained from the ANSYS Fluent material data base and the experimental study [3]. The boundary conditions are summarized in Table 4-8 where the average of the applied wall temperature profile is given instead of the describing polynomial:

Table 4-8: Boundary conditions for the initial single-phase, steady-state flow study.

Boundary	***Boundary Condition***	***Unit***	***Value***
Inlet	Constant mass flux	kg/m²s	15
	Inlet Temperature	°C	68.1, 70.0, 72.5, 74.2, 77.5, 79.1
Outlet	Pressure	Pa	101325
Upper wall	Adiabatic	kW/m²	0
Lower wall	Average wall temperature	°C	97.89,100.44,102.1,103.79,108.74,110.14
	Wall thickness	m	0.0003
	Wall thermal conductivity, k	W/m.K	1.1489

4.4.2 MESH

The importance of proper meshing was discussed previously in Chapter 3.2.2. This included the type of meshing, structured vs unstructured, and the mesh sizing. With the complex nature of flow simulations, it is often preferred to use structured grids in meshing for their simpler algorithms which help to reduce the overall complexity of the simulation. Also as mentioned previously, one of the important factors in investigating the mesh quality is the aspect ratio (AR) of the cells. Using square elements and having an aspect ratio of unity, is the priority as this ensures that the data transfer between cells is not negatively affected. The meshing used in the numerical simulations is illustrated in Figure 4-8 below.

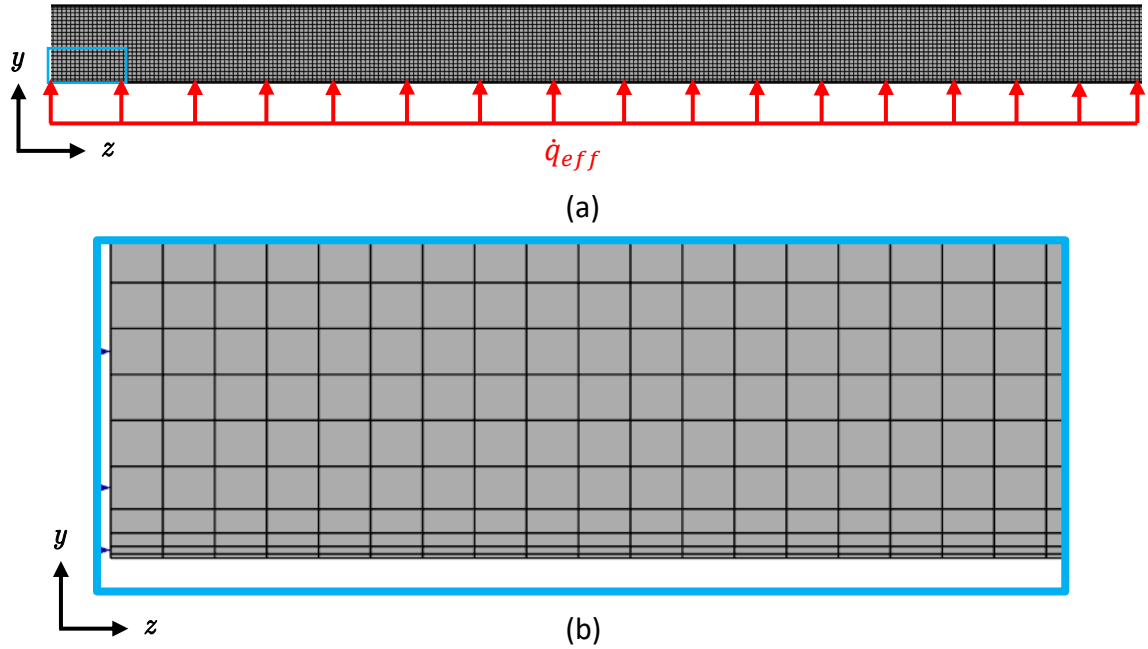

Figure 4-8: Mesh of (a) the initial Two-dimensional numerical domain; (b) Zoomed in view of the inflation layers.

Figure 4-8 (a) shows how the entire domain is meshed along with the initial bubble. A global element size of 17 µm proved to be sufficient, however this was not considered to be a very fine mesh. Figure 4-8(b) highlights the inflation layers near the walls of the domain. Five inflation layers were used to accurately capture the liquid film layer that forms near the wall. Generally, more layers would be used to capture this liquid film layer however, since this is a steady-state simulation for the initial velocity and temperature profiles, the coarseness of this mesh was viable. Furthermore, because mesh refinement was being used in the transient flow boiling simulations that follow, this initial mesh size was suitable to reduce the solution time while still ensuring accurate results.

The summary of the mesh properties is illustrated in Table 4-9 below.

Table 4-9: Numerical domain mesh properties for the single-phase, steady-state study.

Property	***Value***
Global element size	17 µm
Number of inflation layers	5
Total number of cells	8870
Smallest refined element (global)	2.215 µm
Maximum cell aspect ratio	12.3

4.4.3 Simulation Settings

The simulation settings used in ANSYS Fluent 23R1 for the initial single-phase simulations are described here in Table 4-10. Settings ranging from the mesh specifications, solver types, and other modeling methods are all mentioned in the table.

Table 4-10: Summary of the simulation settings used during the initial single-phase simulations.

Property		***Specification***
Geometry (2D)		
H x L_h (mm)		0.3 x 35
Mesh Properties		
Elements		8870
Maximum size (µm)		17
Minimum size (µm)		2.215
Maximum Aspect ratio		7.14
Refinement levels		None
Number of inflation layers		5
Adaption method		None
Boundary Conditions		
Inlet	G (kg/m^{2}s)	15
	T_{in} (°C)	68.1 to 79.1
Outlet	P (kPa)	101.325
	Backflow T (°C)	100
Heated Wall	Temperature Profile average, $T_{wall,avg}$ (°C)	97.89 to 110.14
Solver Settings		
Type		Pressure-based
Precision		Double
Turbulence Settings		
Model		Laminar
Pressure-Velocity Coupling Settings		
Type		Coupled
Discretization Settings		
Pressure		PRESTO!
Momentum		Second-order upwind
Energy		Second-order upwind
Initialisation Settings		
Method		Hybrid
Calculation Settings		
Type		Steady-State
Residual convergence		1E-04 1E-06 (energy)
Iterations		300

4.4.4 Example Output

As described in section 4.2.2, the numerical domain was initialized using a steady state simulation to obtain the fluid temperature and velocity profiles. The VOF method uses a fluid temperature difference across the two-phase interface to induce phase change, thus the temperature profile is very important. This also means that phase change will only occur when the two-phase interface is in contact with fluid at saturation temperature or higher. The

velocity and temperature profiles over the first 5mm of the channel in case 4 (G = 15 kg/m^{2}s, $T_{wall,avg}$ = 108.74°C) are illustrated in Figure 4-9.

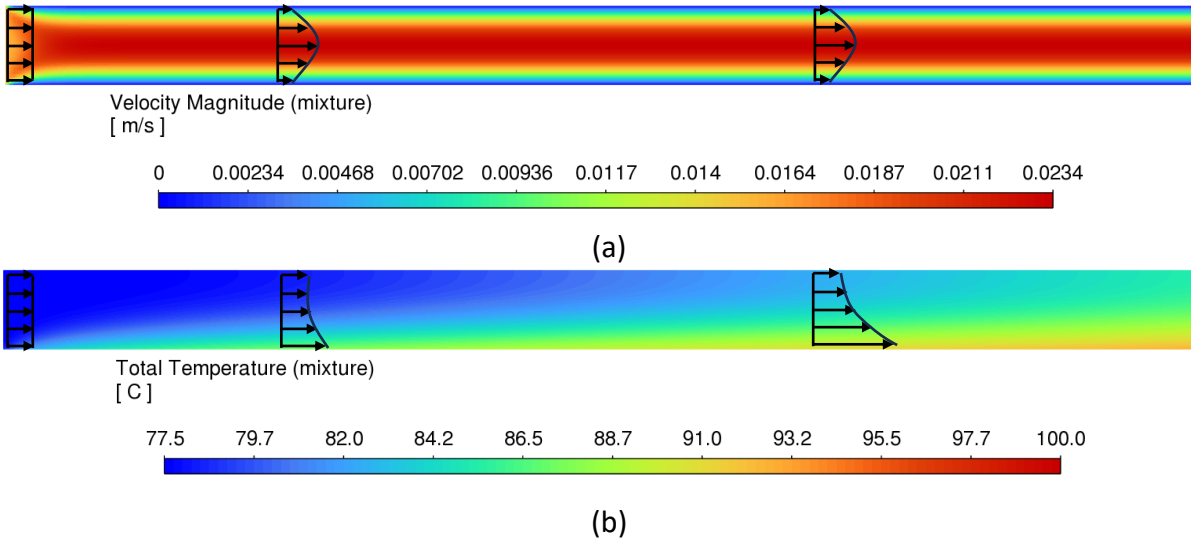

Figure 4-9: Contour plots showing the first 5 mm of the channel with G = 15 kg/m^{2}s and $T_{wall,avg}$ = 108.74°C: (a) The velocity profile; (b) The temperature profile.

It should be noted that the inlet velocity was a uniform 0.0156 m/s which was expected for the 15kg/m²s mass flux when using:

$$u_{avg} = \frac{G}{\rho} \tag{4-14}$$

However, due to no-slip conditions at the walls, the local fluid velocity near the wall becomes zero. This causes the fluid velocity along the centreline of the channel to increase to ensure that the average velocity across the height of the channel remains 0.0156 m/s. This causes the velocity profile to develop as shown in the Figure 4-9(a) by the arrows. Similarly, the temperature profile shows a uniform inlet temperature which becomes non-uniform as one moves away from the inlet. The temperature increases as the fluid moves towards the outlet (to the right), and downwards towards the heated wall.

4.5 Transient Bubble Modeling

The second portion of the simulations involve the transient, two-phase study with the addition of the evaporation model. During this portion, a 0.2 mm diameter bubble was placed in the domain from the single-phase study in a region of saturated liquid as obtained from the fluid temperature profiles. The goal of this study was not to compare the bubble growth rate to the experiments but rather the heat flux, therefore the bubble diameter was selected as large as possible to reduce the computational time required to model initial bubble growth. To ensure that the simulation was stable, the bubble was placed in a region of fully developed flow and outside of the inflation layers. The fluid velocity profile in Figure 4-9(a) shows a thick red band of fluid with similar velocities indicating a region of developed flow. A diameter of approximately 0.2 mm was the largest diameter possible to comfortably fit in this region and ensure simulation stability. The vapour bubble growth was then simulated, and the heat flux results were compared to that of the experimental results.

4.5.1 Domain and Refined Boundary Conditions

The domain used in this portion, illustrated in Figure 4-10, is the same as the domain used in the single-phase study, shown in Figure 4-7, with the addition of the 0.2 mm diameter bubble, d_0. This bubble was placed in a region of saturated liquid, indicated by the black T_{sat} curve, as described in section 4.2.2.

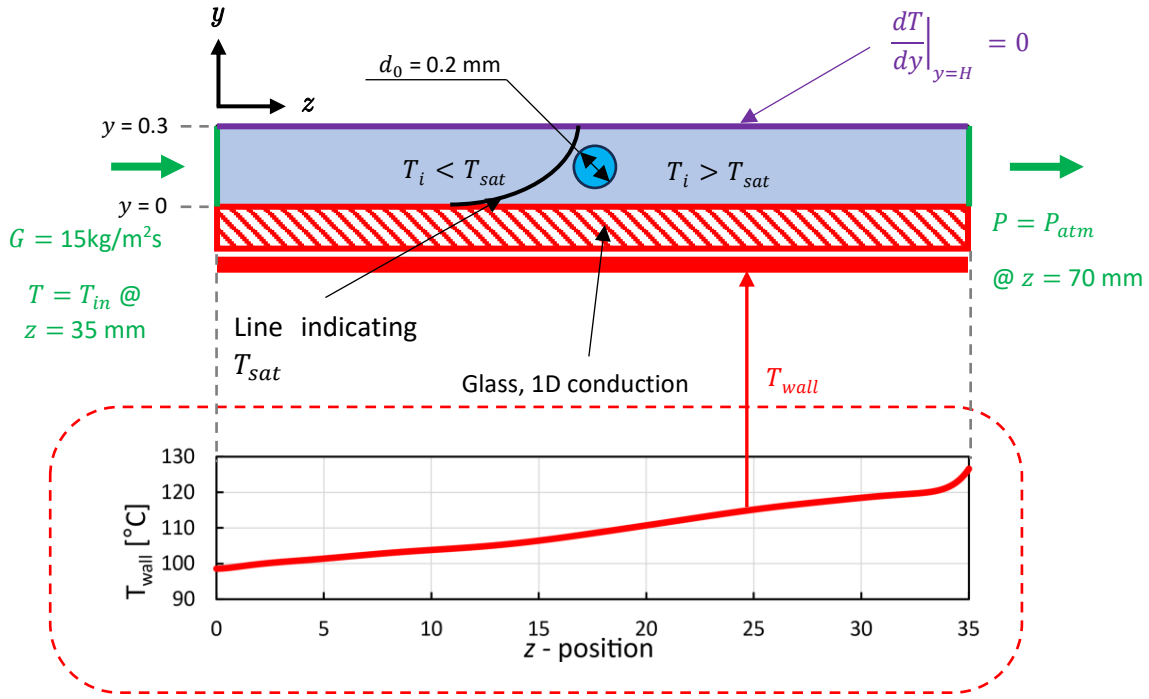

Figure 4-10: 2D representation of the two-phase, transient flow study.

An example of the bubble placement in the test section is shown in Figure 4-11.

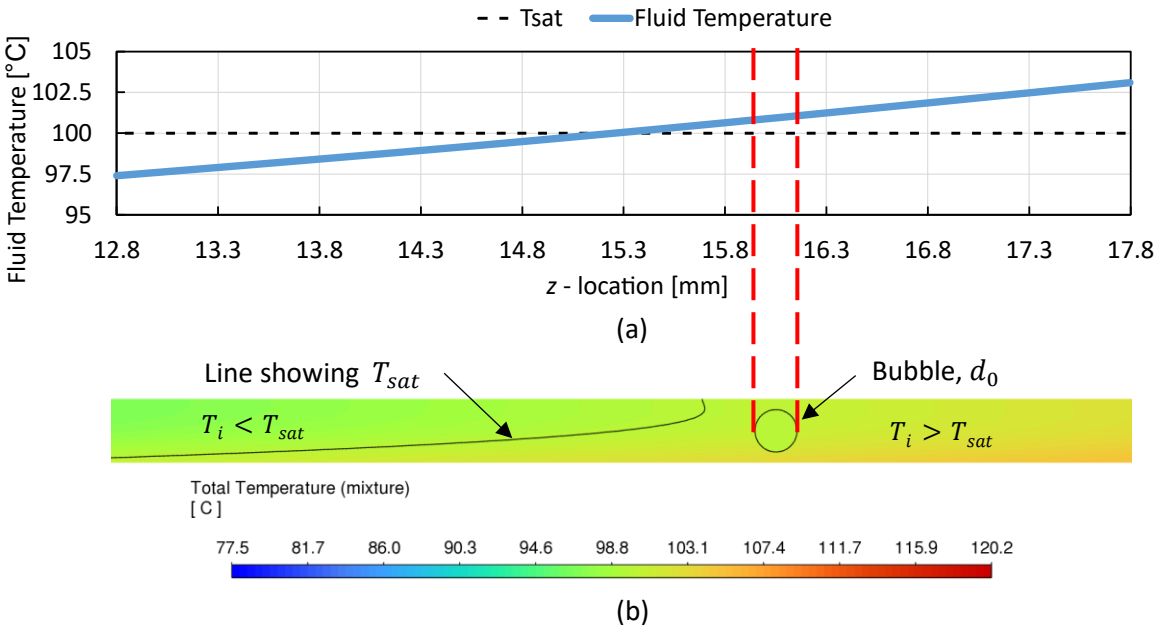

Figure 4-11: Illustration of the bubble initialisation in the validation simulations. (a) The bulk fluid temperature; (b) the fluid domain with temperature contours.

Figure 4-11(a) shows the bulk fluid temperature between the locations z = 12.8 mm and z = 17.8 mm and Figure 4-11(b) illustrates the fluid temperature profile in the channel between these z-locations. The dashed red lines indicate where the bubble was patched with the centre of the bubble placed at z = 16 mm. Figure 4-11(a) shows that the bulk fluid temperature is greater than T_{sat} from z = 15.3 mm onwards, whereas (b) shows that the bubble would only be in a completely saturated region from approximately z = 15.8 mm onwards. Both the bulk fluid temperature and the fluid temperature profile were used to patch the bubbles.

As mentioned in Section 4.2.2, the bubble diameter was selected as 0.2 mm to reduce the simulation time required to solve. The rapid growth of the bubble was required as the experimental results represented large vapour slugs in the channel.

The boundary conditions were therefore the same as in the steady-state case described in section 4.4.1, and are illustrated in Table 4-11.

Table 4-11: Boundary Conditions of the two-phase, transient flow study.

Boundary	***Boundary Condition***	***Unit***	***Value***
Inlet	Constant mass flux	kg/m²s	15
	Inlet Temperature	°C	68.1, 70.0, 72.5, 74.2, 77.5, 79.1
Outlet	Pressure	Pa	101325
Upper wall	Adiabatic	kW/m²	0
Lower wall	Average wall temperature	°C	97.89,100.44,102.1,103.79,108.74,110.14
	Wall thickness	m	0.0003

	Wall thermal conductivity, k	W/m.K	1.1489
Bubble	Fluid Temperature	°C	T_{sat}

4.5.2 MESH

With the addition of the vapour bubble, the mesh refinement was implemented via the UDF to accurately model the heat transfer and phase change across the bubble interface. The mesh refinement is also necessary as it reduces the cell size in the areas of interest ensuring accurate results, while not drastically affecting the required computational power. The meshing used in the two-phase, flow boiling simulations are shown in Figure 4-12.

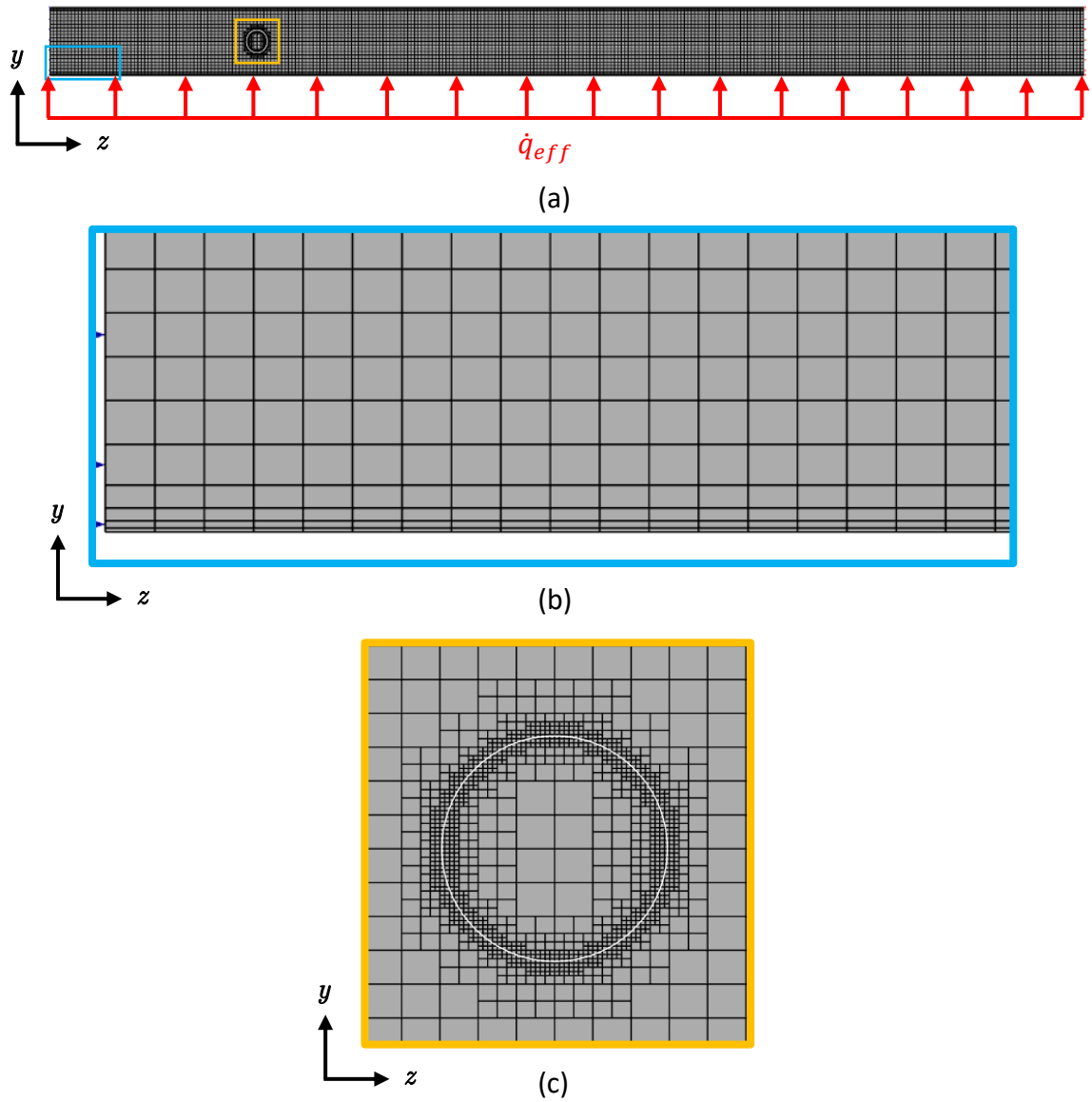

Figure 4-12: Mesh of (a) the initial Two-dimensional numerical domain; (b) Zoomed in view of the inflation layers; (c) Zoomed in view of the bubble interface.

Figure 4-12 (a) shows how the entire domain is meshed along with the initial bubble. Just as with the single-phase study, a global element size of 17 µm was used with five inflation layers near the wall, shown in (b). The adaptive mesh refinement illustrated in (c) reduced the mesh elements using 3 levels which resulted in the elements shrinking down to 2.125 μm around the interface. This meant that an area reduction of 8^2, or 64, was enforce by the mesh refinement taking the cell areas from 289 μm^2 to 4.516 μm^2. The mesh refinement caused the cells in the inflation layer to also reduce by 8 times their original size.

The summary of the mesh properties is illustrated in Table 4-12below.

Table 4-12: Numerical domain mesh properties for the two-phase, transient study

Property	***Value***
Global element size	17 µm
Number of inflation layers	5
Refinement levels	3
Total number of cells (initial - maximum)	8870 to 43079
Smallest refined element (global)	2.215 µm
Smallest refined element (inflation layer)	0.31 µm
Maximum cell aspect ratio	7.15

4.5.3 Simulation Settings

The simulation settings follow from those described in the steady-state study found in section 4.4.3 with a few additional settings. Once the bubble was patched and initialised in the domain, the UDF was implemented via the energy equation (equation (3-12)) and the volume fraction advection equation (equation (3-14)) and the simulations were solved. The simulations ran until the bubble leading edge had exited the outlet of the domain, with the higher heat flux cases solving quicker. The simulations ran for flow times ranging from 5.6ms to 10.4ms, taking approximately 24 hours in actual simulation time. The simulation settings used in the two-phase transient simulations are shown in Table 4-13.

Table 4-13: Summary of the simulation settings used during the two-phase simulations.

Property		***Specification***
Geometry (2D)		
H x L_h (mm)		0.3 x 35
Mesh Properties		
Elements		8870-43079
Maximum size (µm)		17
Minimum size (µm)		2.215
Maximum Aspect ratio		7.14
Refinement levels		3
Number of inflation layers		5
Adaption method		User-Defined Function (UDF)
Boundary Conditions		
Inlet	G (kg/m^{2}s)	15

	T_{in} (°C)	68.1 to 79.1
Outlet	P (kPa)	101.325
	Backflow T (°C)	100
Heated Wall	Temperature Profile average, $T_{wall,avg}$ (°C)	97.89 to 110.14
Solver Settings		
Type		Pressure-based
Precision		Double
Turbulence Settings		
Model		Laminar
Multiphase Settings		
Model		VOF
Interface		Sharp
Evaporation modelling		Modified Schrage (User-Defined Function)
Volume fraction cut-off		1E-06
Surface tension model		CSF
Pressure-Velocity Coupling Settings		
Type		PISO
Discretization Settings		
Pressure		PRESTO!
Momentum		Second-order upwind
Energy		Second-order upwind
Time		First-order implicit
Volume Fraction		Compressive/implicit
User-defined Scalars		First-order upwind
Initialisation Settings		
Method		Standard
Bubble z-velocity (m/s)		0.0234
Bubble y-velocity (m/s)		0
Temperature (°C)		100
Vapour quality		0
Calculation Settings		
Type		Transient
Flow time (ms)		5.6 to 10.4
Time step size (s)		2E-7
Residual convergence		1E-04 1E-06 (energy)
Maximum iterations		20

4.6 Numerical Results And Comparison With Experimental Case

The experimental results obtained investigated the effective heat flux, the average local wall temperatures, and the average local heat transfer coefficients. Since the numerical model applies the average local wall temperatures as a boundary condition for the heated wall, the local heat flux is obtained and compared. First, Figure 4-13 is presented to illustrate how the

vapour slug grows throughout the domain during each numerical simulation. Case 4, with an average heated wall temperature of 108.74°C, was used to represent this growth.

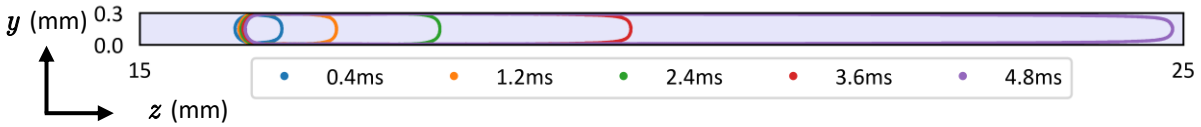

Figure 4-13: Example of the bubble growth throughout the validation simulations of the 108.74°C average wall temperature case.

It should be noted that only 0.15 mm to 0.25 mm of the domain is represented in Figure 4-13 as showing a greater portion of the channel would hinder the readers ability to visualise the bubble growth.

An example of how the local heat flux along the channel length looks is illustrated in Figure 4-14 below.

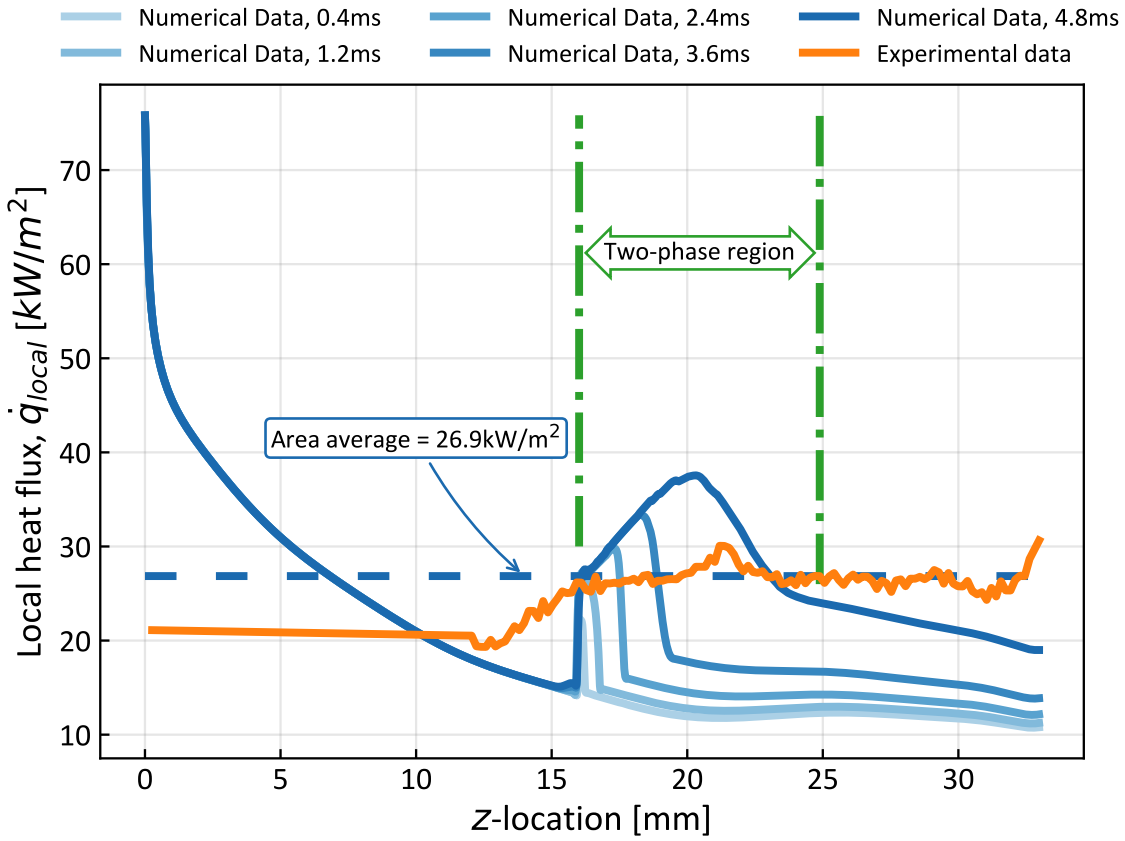

Figure 4-14: An example of the local heat flux along the heated wall for the 108.74°C average wall temperature case at various flow times for the numerical data (shades of blue) and the time-averaged local data for the 108.86°C average wall temperature case for the experimental data (orange).

Figure 4-14 shows the local heat flux for case 4 ($T_{wall,avg}$ = 108.74°C) of the numerical study with the various timesteps illustrated in different shades of blue, and case 4 ($T_{wall,avg}$ = 108.86°C) of the experimental study illustrated in orange. The dashed blue line represents the area-averaged local heat flux of the numerical data at a 4.8 ms. Additionally, the green two-phase region represents the two-phase region for the numerical data at 4.8 ms

and was calculated using the local heat flux values along the entire 35 mm length. A clear decrease in the local heat flux from the inlet to the outlet is shown across all the represented timesteps of the numerical data, with a spike in the two-phase region. As the simulation develops and the bubble grows, the local heat flux increases, and the spike begins to plateau. On the other hand, the experimental data shows a steady decrease in heat flux from the inlet to the two-phase region (approximately z = 12.5 mm), thereafter the heat flux spikes and plateaus with relatively noisy measurements. The fluctuations in experimental data illustrate the volatility of flow boiling. As the numerical data progressed, it was observed that the local heat flux began to plateau like the experimental data. It then follows that the difference between the numerical and experimental local heat fluxes is mainly attributed to the experimental data being time-averaged over a 65 second period whereas the numerical data represents a specific time instant. This means that fluid near the heated wall has had time to develop meaning that the surface and fluid temperatures are more stable than when compared to the initial growth stages represented by the numerical investigation.

It is expected that the two-phase region experiences the peak heat flux in the numerical results however, the peak is instead observed at in the inlet. This is caused by the type of inlet boundary conditions used as the fluid temperature at the inlet near the wall is forced to be different to the wall temperature at the inlet. This is due to the inlet temperature having a uniform profile along the height of the channel, instead of having a non-uniform profile. This can be seen by the local heat flux drastically decreasing as you move to the right of the inlet where the fluid temperature near the wall converged to the wall temperature. A visual illustration is shown in Figure 4-15 to better explain what is meant by a uniform and a non-uniform inlet temperature profile.

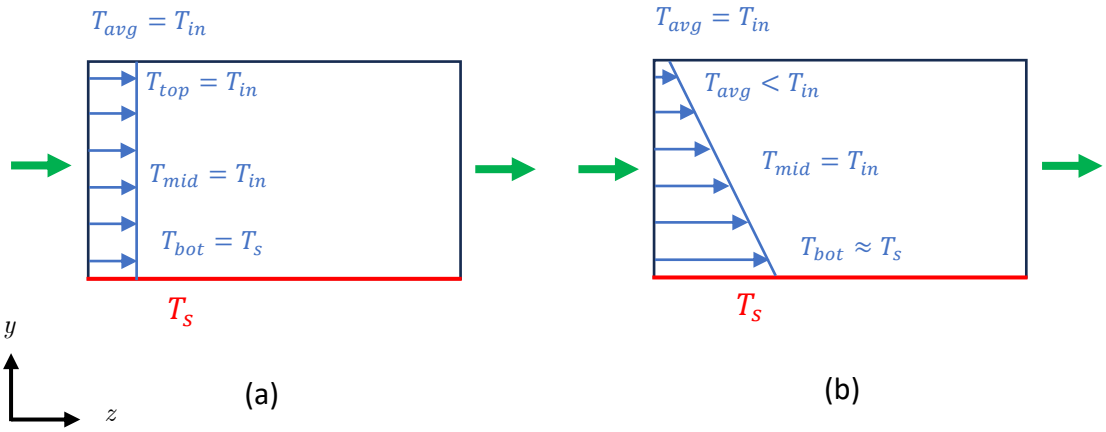

Figure 4-15: Visual representation of possible inlet temperature profiles; (a) Uniform profile; (b) non-Uniform profile.

To test whether a non-uniform temperature profile like the one in Figure 4-15(b) would improve the results, the heat fluxes were recorded for the initial time stamp of the case 4 before the bubble is initialized. The results were compared when using (a) a Uniform temperature profile (constant temperature) and (b) a non-uniform temperature profile. The non-uniform temperature profile was described by the linear function $T(y) = -140000y +$

371.6 $[K]$ which resulted in $T(0) = T_s$ and $T_{avg} = T_{in}$. The results are show in Figure 4-16 below.

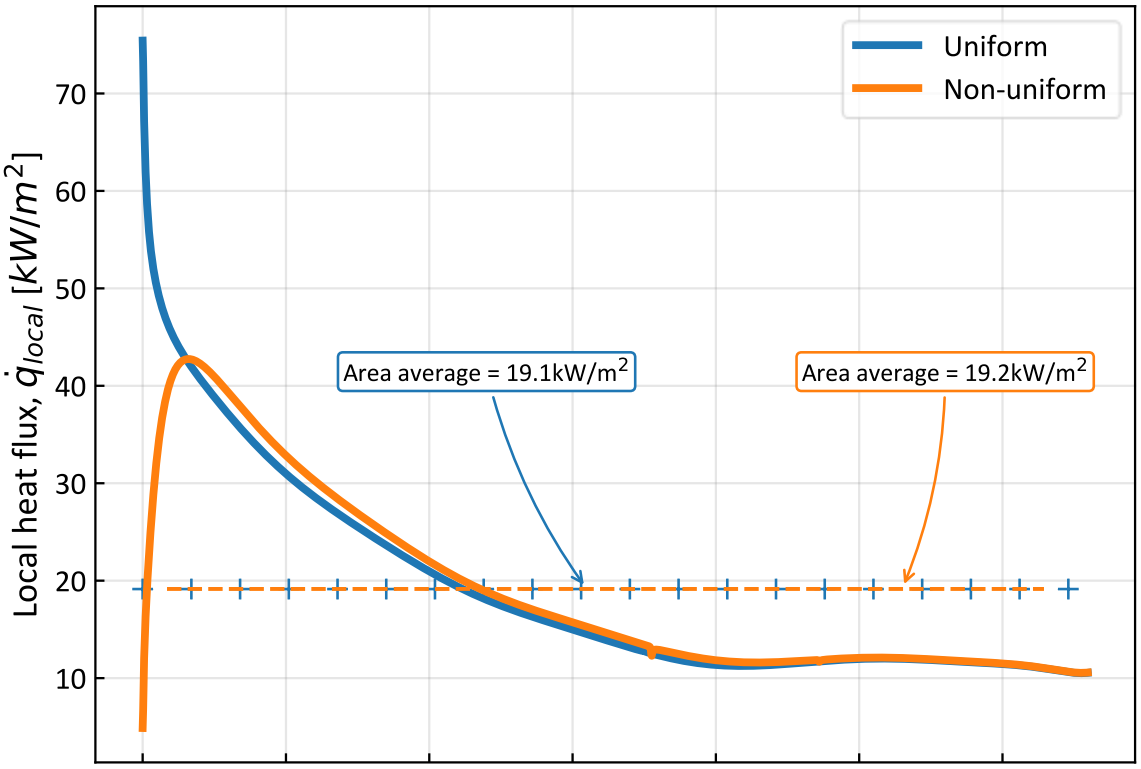

Figure 4-16: Testing the local heat flux along the heated wall of the channel for the 108.74°C average wall temperature case when using (a) a uniform temperature profile at the inlet; and (b) using a non-uniform temperature profile at the inlet.

There is a drastic drop in the local heat flux at the inlet of the channel, however there is still a spike near the inlet where the fluid velocity profile becomes fully developed. Additionally, even with this drastic drop in heat flux, the average heat flux changes by 0.1 kW/m² which is a 0.5% difference. Because of this, it was decided to use a uniform temperature inlet for all the simulations.

Looking back at Figure 4-14, the area-averaged heat flux along the length of the channel was calculated. We are more interested in only the two-phase region, however, the experimental data looked at the entire channel length and not solely on the two-phase region. Therefore, the area-average, described by equation (4-5), of the heat flux over the entire channel was used. This average was obtained for each time stamp in the measured numerical data and the results can be seen in Figure 4-17 below.

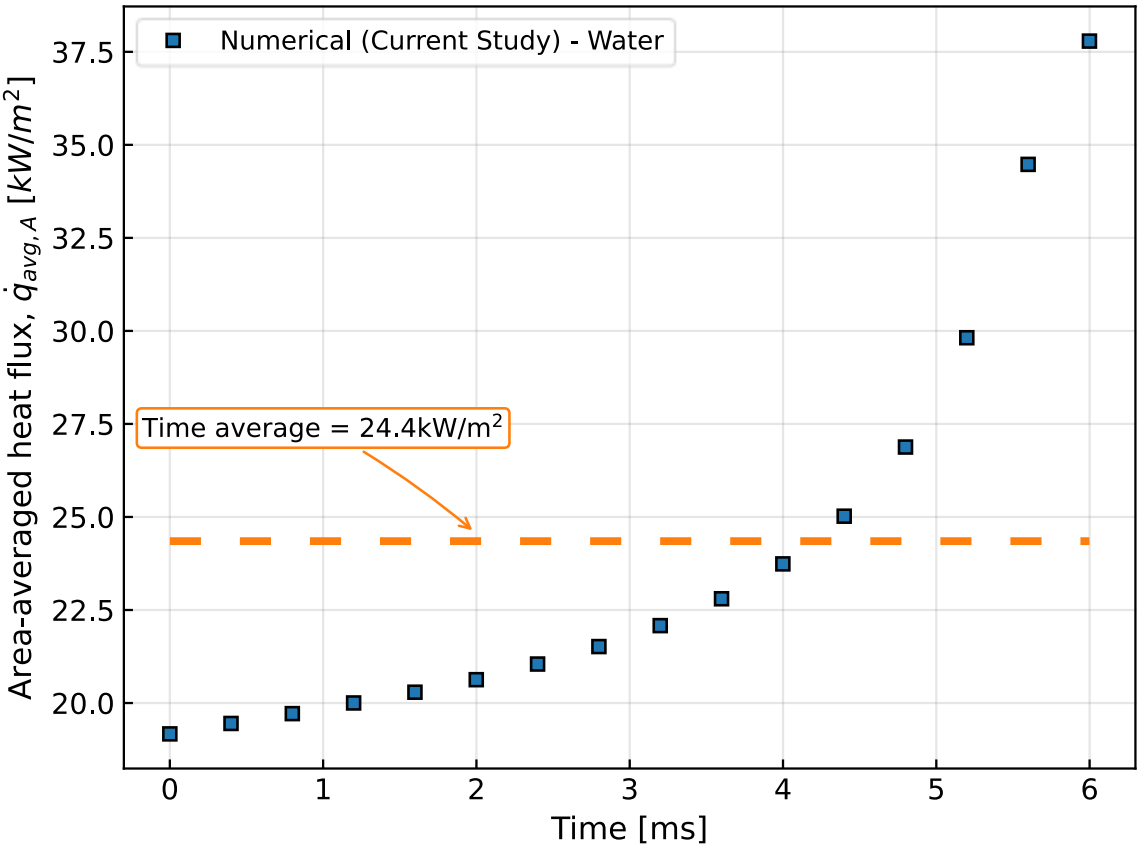

Figure 4-17: Area-averaged heat flux along the heated wall of the channel at various time instances of the 108.74°C average wall temperature case within the numerical study.

Figure 4-17 illustrates how the area-averaged heat flux, or the effective heat flux of the channel, changes during the simulation as the bubble grows. As the simulation progresses and the bubble grows, the average heat flux in the domain increases. This is because the two-phase region, where there is an increased heat flux, continues to grow. The experimental data considers the time-averaged data captured over a period. Comparing the results to the experimental work requires a time-average of the heat fluxes obtained for each simulation. Figure 4-17 shows the time averaged heat flux for case 4 ($T_{wall,avg}$ = 108.74°C) with the orange dashed line as 24.4kW/m². This time-averaging was applied to all six cases, and the results are shown in Figure 4-18 below.

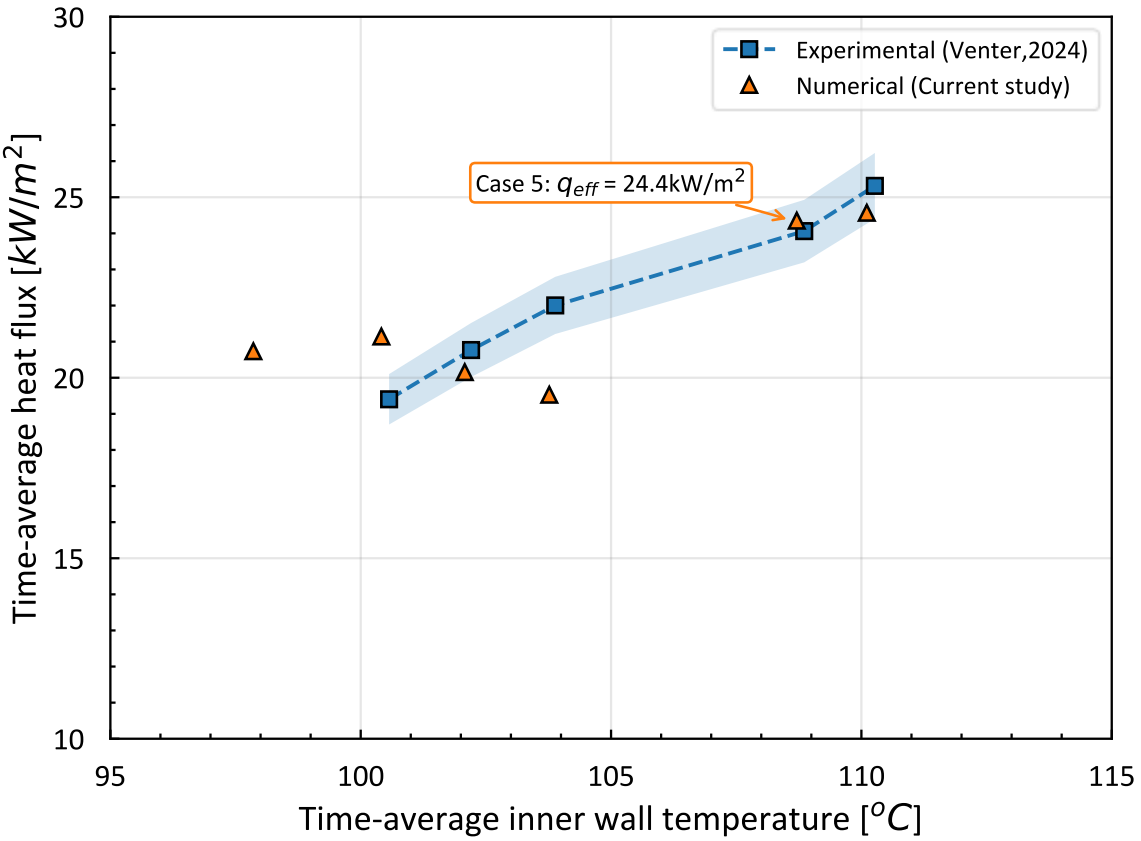

Figure 4-18: Effective heat flux against the average wall temperature comparing the numerical results (orange) to the experimental work (blue). The experimental results had a maximum error of 3.6% indicated by the blue shading.

Figure 4-18 illustrates the six numerical cases (orange triangles) vs the five experimental cases (blue squares). As previously mentioned, the experimental results were re-processed after the numerical study was conducted which caused very slight alterations to the measure wall temperatures as well as the removal of one case. The slight alterations to the measured wall temperatures are indicated by the small offset in inner wall temperature between the numerical and experimental results. The numerical results are shown to predict very similar heat fluxes to the experimental results with some data points underpredicting the experimental data points and others overpredicting the experimental data points. These discrepancies are attributed to many factors such as the numerical model being two-dimensional whereas the experiments are three-dimensional. This means that all three-dimensional effects are lost in the numerical simulations. Additionally, the numerical simulations only replicate about 20 ms of flow time where the bubble grows throughout the domain, whereas the experimental data considers 60 s of flow time only once the flow has stabilized and the vapour slug is at a relatively constant size. Furthermore, the simulations consider constant fluid properties, except for the surface tension, whereas the experimental data considered the effect of temperature and pressure on fluid properties. Considering these differences caused by the numerical assumptions, it is important that the numerical results present a similar trend to the experimental data. Apart from two data points, case 1 (100.4°C) and case 3 (103.8°C), which overpredict and underpredict the experimental data respectively,

the numerical data forms a trend very similar to the experimental data. The results indicate that as the heating was increased using higher surface temperatures, the effective heat flux increased.

These results showed that the numerical model was accurately simulating the boiling of water in a microchannel and would be sufficient in trying to simulate the self-rewetting fluids.

4.7 Chapter Summary

This chapter discussed the experimental test cases from Venter [3] that were used to develop the numerical domain and to validate its applicability. Here the importance of the experimentally measured wall temperature was discussed for its use as a boundary condition in the numerical model. This was followed by describing the numerical domain used with the relevant generic boundary conditions that are applicable to the main numerical study in the next chapter. The numerical domain discussed was two-dimensional (2D) with a length of 35 mm and a height of 0.3 mm. Additionally, the numerical approach was briefly discussed by describing that the numerical studies were separated into an initial set of single-phase steady-state simulations and a set of two-phase transient simulations. This was done to ensure the success of the more complex, transient simulations. This chapter then addressed the fluid properties of water as used in both the experimental and numerical investigations. This was then followed with a discussion for both the initial single-phase, steady-state simulations and the two-phase, transient simulations by addressing the necessary boundary conditions used, mesh structure implemented, and simulation settings applied. Lastly, the effective heat flux vs the average surface temperature was compared between the numerical model and the experimental investigation. The results indicated that the numerical model predicted similar results when compared to the experimental results and shared the same trend. However, some results over-predicted the experimental results while others under-predicted which were ascribed largely due to the model being two-dimensional whereas the experiments are three-dimensional. With the numerical model predicting such similar results, it was trusted to accurately model the numerical investigations to come.

The next chapter discusses the influence of self-rewetting on microchannel flow boiling. Here the model discussed is mostly used with small differences such as the domain shortening to 5 mm and the applied heating changing to an applied heat flux. Again, the chapter starts by describing the numerical domain and boundary conditions, which is then followed by the fluid properties of 5% v/v 1-butanol-water, and a short description of the test matrix used. The chapter then discusses the results obtained by investigating the bubble behaviour and the heat transfer characteristics.

5 INFLUENCE OF SELF-REWETTING

This chapter describes the influence of self-rewetting on microchannel flow boiling by using the 5% v/v 1-butanol-water mixture as the self-rewetting fluid (SRF). The chapter starts by presenting the two-dimensional (2D) numerical domain used along with the relevant boundary conditions applied. This is then followed by the fluid property modeling section which discusses how the SRF propertues were defined. A short section on the test matrix used is briefly discussed before the discussion of the results. The results are described in two portions namely, the bubble behaviour and the heat transfer. Lastly, a summary of the chapter is provided.

5.1 NUMERICAL MODEL

5.1.1 MODELLING APPROACH

A similar 2D domain was used as that in the validation study discussed in the previous chapter. The intention is to compare pure water to a 5% v/v 1-butanol mixture as the self-rewetting fluid (SRF). An example of the 2D domain modelled for the validation study is illustrated in Figure 5-1.

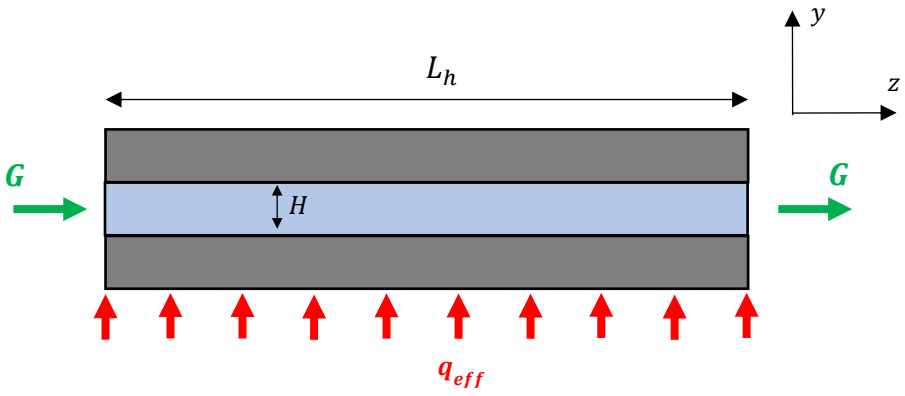

Figure 5-1: 2D Numerical domain simplification.

This study focused on the bubble growth rate in the channel and how this effects the heat transfer capabilities. During the validation study it was noted that the initial bubble clogs the channel very quickly with majority of the simulation time modeling the horizontal expansion of the vapour slug that forms. For these reasons it was decided that a shorter domain would suffice, thus a domain length of L_h = 5 mm was used instead of the 35 mm used in the validation. This reduction in channel length greatly reduced the computational power and time required to conduct the simulations. Furthermore, only the fluid domain denoted by length L_h = 5 mm and height H = 0.3 mm was modelled.

Again, the simulations were divided into two portions, with the first portion consisting of the single-phase steady-state study and the second portion consisting of the two-phase transient study. During the first portion, a constant, uniform mass flux was applied to the inlet of the domain just as previously done in the validation study. The inlet fluid temperature was at saturation temperature to speed up the computational time and to reduce unnecessary

single-phase regions. Additionally, a heat flux was applied to the bottom wall to provide heating to the fluid. The first portion was performed to obtain the fluid velocity and temperature profiles as done previously in the validation case.

The second portion used the temperature and velocity profiles obtained from the first portion of simulations to ensure the success and stability of the transient simulations. The second portion also implemented the two-phase evaporation model in the form of the UDF as described earlier. At the start of the transient simulations, a 0.1 mm diameter bubble was patched into the domain and allowed to grow. In this study, the bubble growth and behaviour near the heated wall was of interest, therefore it was not necessary to model the smallest possible bubble. Instead, only a short period of bubble growth before confinement was necessary to illustrate initial bubble growth and reduce any possible affects bubble confinement may have on the initial bubble growth. It was observed that a diameter of 0.1 mm allowed for a minimum of two data points to be captured before confinement for the high heat flux cases, and more for the low heat flux cases. This was deemed sufficient to represent the initial growth rate and ensure that bubble confinement did not influence this initial growth rate. With the inlet fluid temperature set at saturation temperature, the bubble placement was not dependent on the bulk fluid temperature but rather on the fluid velocity profile. Figure 5-2 shows an example of the fluid velocity profile with the bubble initialised.

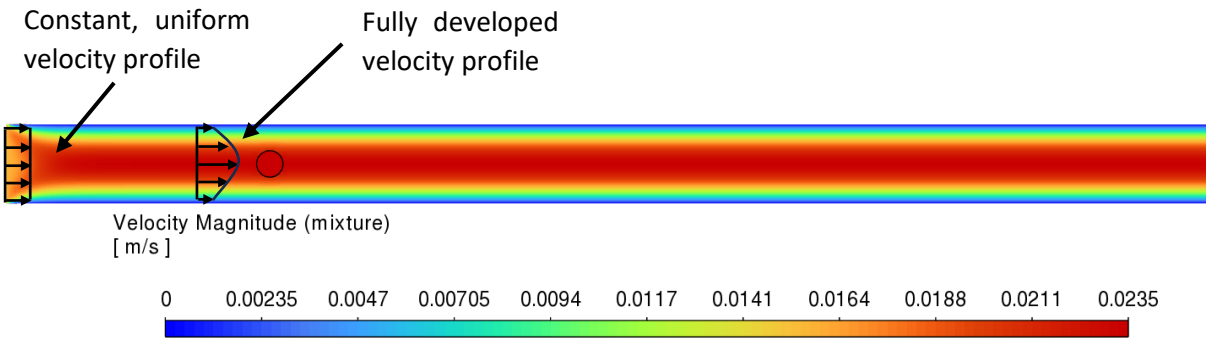

Figure 5-2: Example fluid velocity profile with patched bubble.

The bubble was placed in a region of fully developed flow as indicated in Figure 5-2.

5.1.2 Domain And Boundary Conditions

The 2D domain used in this study is illustrated in Figure 5-3 below. Unlike previously, heating was applied to the bottom wall via a constant heat flux with a wall thickness as a boundary condition.

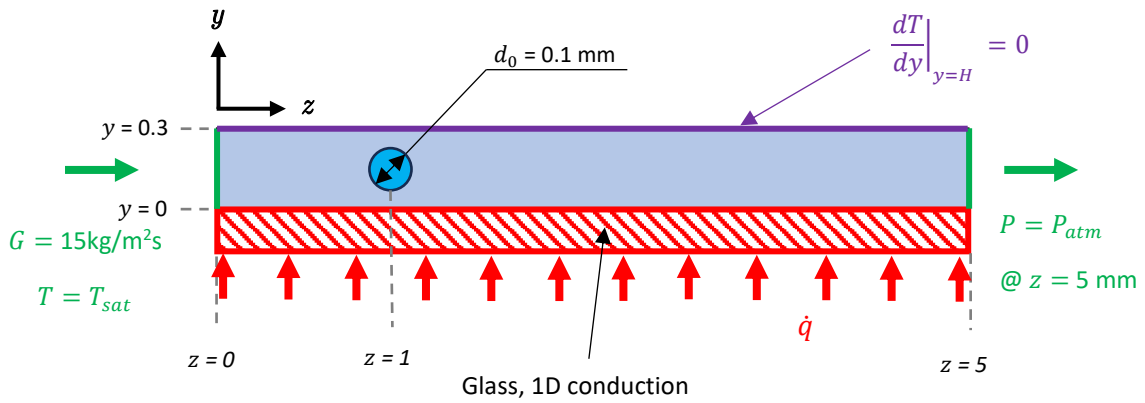

Figure 5-3: 2D numerical domain for the self-rewetting study.

The 0.1 mm bubble was inserted 1 mm downstream of the inlet where the velocity profile was fully developed, as mentioned in Chapter 5.1.1. By patching the bubble in at this location, it meant that the bubble would only ever grow to maximum of 4 mm in length.

BOUNDARY CONDITIONS

A constant mass flux of G = 15 kg/m² was applied to the inlet which was carried over from the experimental data by Venter [3], as it had the more stable results in general. The inlet fluid temperature however was set to saturation temperature to ensure that phase change occurred. The outlet made use of a pressure outlet at atmospheric pressure, again matching the experimental setup with its downstream collector tank open to atmospheric pressure. The bottom wall was heated using a constant heat flux instead of a temperature profile, like in the validation, since the intention of the numerical investigation was no longer to mimic the experimental results. The applied heat flux used values ranging from 1 kW/m² to 40 kW/m². Lastly, the top wall was set as an adiabatic boundary condition like the validation study meaning that heat losses were not modelled.

A summary of the boundary conditions for the numerical domain can be seen in Table 5-1 below.

Table 5-1: Summary of the boundary conditions used for the numerical domain for both water and SRF cases.

Boundary	***Boundary Condition***	***Unit***	***Value***
Inlet	Constant mass flux	kg/m²s	15
Outlet	Pressure	Pa	101325
Upper wall	Adiabatic	kW/m²	0
Lower wall	Constant heat flux	kW/m²	1,5,10,15,20,30,40
	Wall thickness	m	0.0003
	Wall thermal conductivity, k	W/m.K	1.1489
Bubble	Temperature	°C	T_{sat}

5.2 Fluid Property Modelling

With limited available thermophysical properties for 1-butanol, obtaining or predicting the properties for the 1-butanol-water mixture were challenging. Just like in section 4.3.1, the linear ideal mixing rule was used to obtain the properties for the mixture. This means that the properties were approximated by multiplying the molar fractions to each substance and adding them together. Using these methods, the properties of the 5% v/v 1-butanol-water mixture at 25°C (298 K) were predicted to differ by a maximum of 1.8% from that of water. However, since this study is focused mainly on the two-phase region, the fluid properties at saturation temperature are the most important. Even fewer properties were obtainable for 1-butanol at saturation temperature for both single and two-phase regions. Consider the T-x-y data, which refers to the temperature versus composition diagram, for 1-butanol-water mixtures at 1 bar by Straathof et al. [55] in Figure 5-4:

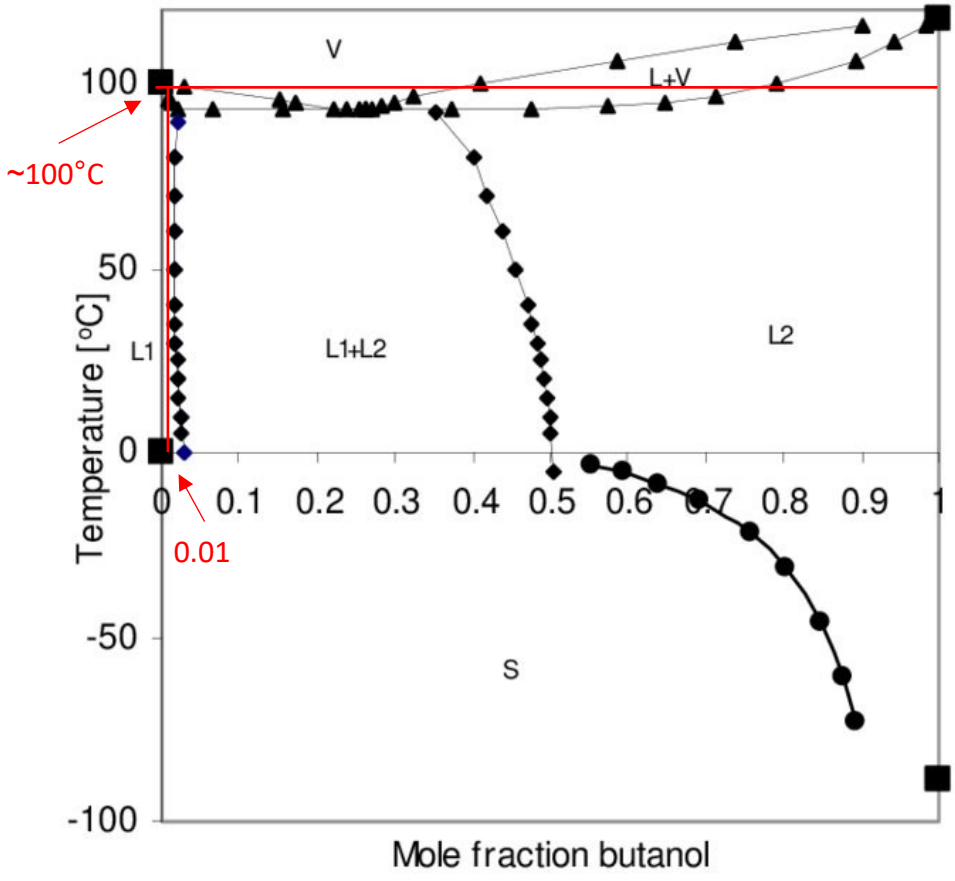

Figure 5-4: T-x-y data for 1-butanol-water mixtures at 1 bar from Straathof et al. [55]. The triangle markers indicate the vapour-liquid data, the diamond markers indicate the liquid-liquid data, and the circles indicate the solid-liquid equilibrium data.

The T-x-y diagram shows the mixture composition lines for various mixture ratios with T representing the temperature, x representing the liquid composition, and y representing the vapour composition. It should be noted that for 5% v/v 1-butanol-water, with a molar fraction of 0.01, the saturation temperature is expected to be approximately 100°C. This approximation corresponded well with the initial saturation temperature of 100.14°C

experimentally measured by Venter [3]. Predicting fluid properties of mixtures near the saturation point and in the two-phase region becomes increasingly challenging. Because of this, and the similar properties to water at 25°C, the properties of water were assumed for both fluids. The only property that differed between the two fluids was the surface tension as this property is the focal point of the study. Hence, fluid properties used for both fluids were that of water at saturation temperature (100°C) and can be seen in Table 5-2.

Table 5-2: Fluid properties at 100° (373K) for both water and the SRF

Property	***Symbol***	***Units***	***Water***	***5% v/v 1-Butanol-Water (SRF)***
Saturation temperature	T_{sat}	°C	100	
Latent Heat of vaporization	h_{lv}	J/kg	2257 x 10^{3}	
Density (Liquid)	ρ_l	kg/m3	958.2	
Density (Vapour)	ρ_v	kg/m3	0.6010	
Viscosity (Liquid)	μ_l	Pa.s	281.2 x 10^{-6}	
Viscosity (Vapour)	μ_v	Pa.s	12.24 x 10^{-6}	
Specific heat (Liquid)	$c_{p,l}$	J/kg.K	4215.8	
Specific heat (Vapour)	$c_{p,v}$	J/kg.K	2080.6	
Conductivity (Liquid)	k_l	W/m.K	677.3 x 10^{-3}	
Conductivity (Vapour)	k_v	W/m.K	24.6 x 10^{-3}	
Surface tension (100°C)	σ	N/m	58.9 x 10^{-3}	32.3 x 10^{-3}

The surface tension in Table 5-2 was given as the value at saturation point. However, the surface tension with respect to temperature of the two fluids is illustrated in Figure 5-5 below.

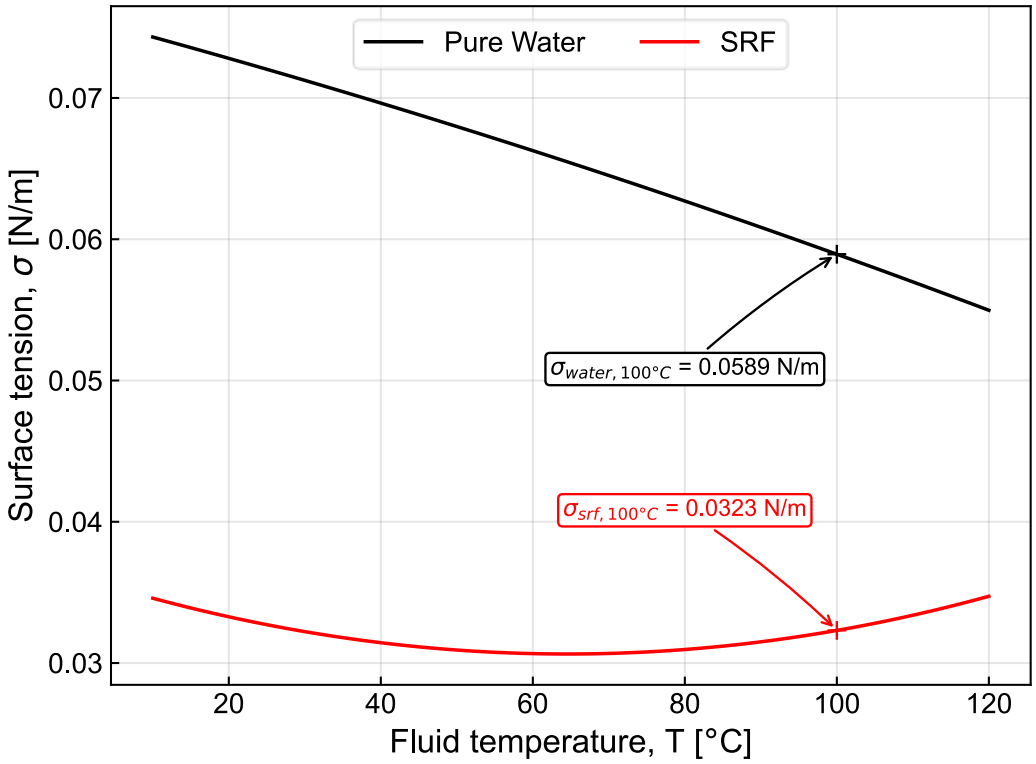

Figure 5-5: Temperature dependent surface tension profile for water and SRF. The surface tension values at saturation (100°C) are illustrated with the cross markers.

Here the non-linear temperature dependency of the SRF surface tension is illustrated with the a 'turning point' at roughly 65°C. It should also be noted that the water has a greater surface tension everywhere, in the provided temperature range. These two curves were described by 2nd order polynomials using the temperatures in °C, with the general polynomial formulations shown by:

$$\sigma(T) = C_2 T^2 + C_1 T + C_0 \quad (5\text{-}1)$$

Here C_0, C_1, and C_2 are polynomial coefficients. The respective coefficients for the two fluids are shown in Table 5-3.

Table 5-3: Polynomial coefficients describing the temperature dependent surface tension curves.

Fluid	C_0	C_1	C_2	R^2
5% v/v 1-butanol-water	0.0361700568	-1.71363860E-04	1.32767318E-06	0.994
Pure water	0.0757722228	-1.43395295E-04	-2.49482313E-07	1

It should be noted that after the re-processing of the experimental data, the actual measured saturation temperature of the SRF was 93.5°C. This "new" saturation temperature is significantly lower than the initially expected, and modelled, 100°C. If the correct saturation temperature of 93.5°C was used for the SRF, it is expected that the simulated heated surface temperature would have lowered by approximately the difference in saturation temperature (6.5°C). This is because the self-rewetting nature of the SRF is the main contributor to how

the bubble grows. At a fluid temperature of 93.5°C, Figure 5-5 indicates that the SRF is still in a region of a positive surface tension gradient and thus in a region of self-rewetting. To remove the effect the choice of saturation temperature has on the results, the surface temperature difference above saturation temperature ($\Delta T = T_s - T_{sat}$) and the heat transfer coefficient was compared between the two fluids. With the surface temperature being influenced by the saturation temperature, using the surface temperature difference and heat transfer coefficients means that fluids with differing saturation temperatures can be compared.

5.3 Test Matrix

A total of 14 test cases were investigated which compared the pure water and the SRF across a range of heat fluxes applied to the bottom wall. The tests conducted are illustrated in the test matrix in Table 5-4 below.

Table 5-4: Test Matrix describing the 14 numerical simulations conducted.

Case	***Fluid***	***Inlet Mass flux [kg/m²s]***	***Inlet Temperature [°C]***	***Applied Heat flux [kW/m²]***
1	5% v/v 1-Butanol-Water (SRF)	15	100	1
2				5
3				10
4				15
5				20
6				30
7				40
8	Water	15	100	1
9				5
10				10
11				15
12				20
13				30
14				40

The purpose of the 14 cases was to investigate how the different surface tensions in these two fluids effect the heat transfer capabilities.

The ANSYS Fluent Simulation settings used in this study are illustrated in Table 5-5.

Table 5-5: Summary of the simulation settings used in the Self-rewetting study.

Property	***Specification***
Geometry (2D)	
H x L_h (mm)	0.3 x 5
Mesh Properties	
Elements	8870-43079
Maximum size (µm)	17

Minimum size (µm)		2.215
Maximum Aspect ratio		7.14
Refinement levels		3
Number of inflation layers		5
Adaption method		User-Defined Function (UDF)
Boundary Conditions		
Inlet	G (kg/m^{2}s)	15
	T_{in} (°C)	100
Outlet	P (kPa)	101.325
	Backflow T (°C)	100
Heated Wall	Constant, uniform heat flux, $\dot{q}$ (kW/m²K)	1 to 40
Solver Settings		
Type		Pressure-based
Precision		Double
Turbulence Settings		
Model		Laminar
Multiphase Settings		
Model		VOF
Interface		Sharp
Evaporation modelling		Modified Schrage (User-Defined Function)
Volume fraction cut-off		1E-06
Surface tension model		CSF
Pressure-Velocity Coupling Settings		
Type		PISO
Discretization Settings		
Pressure		PRESTO!
Momentum		Second-order upwind
Energy		Second-order upwind
Time		First-order implicit
Volume Fraction		Compressive/implicit
User-defined Scalars		First-order upwind
Initialisation Settings		
Method		Standard
Bubble z-velocity (m/s)		0.0234
Bubble y-velocity (m/s)		0
Temperature (°C)		100
Vapour quality		0
Calculation Settings		
Type		Transient
Flow time (ms)		1.5 to 20.6
Time step size (s)		2E-8 to 2E-7
Residual convergence		1E-04 1E-06 (energy)
Maximum iterations		20

5.4 Bubble Behaviour

5.4.1 Bubble Growth

With the difference in surface tension emphasized between the two fluids, it is important to compare the bubble growth rates. As a sanity check, for all cases it was observed that the initial bubble grew until clogging, followed rapid growth of the leading edge towards the outlet. The bubble interface was tracked for each case with Figure 5-6 representing the interfaces for case 5, SRF with $\dot{q}$ = 20 kW/m², and case 12, water with $\dot{q}$ = 20 kW/m², respectively. Case 5 and 12 were used for discussion purposes throughout this sub-section. The interfaces were used to obtain a dimensionless bubble length by dividing the bubble length (L_b) along the z axis with the initial bubble diameter (L_b/d_0) shown in (c) and (d) for the SRF and pure water cases respectively.

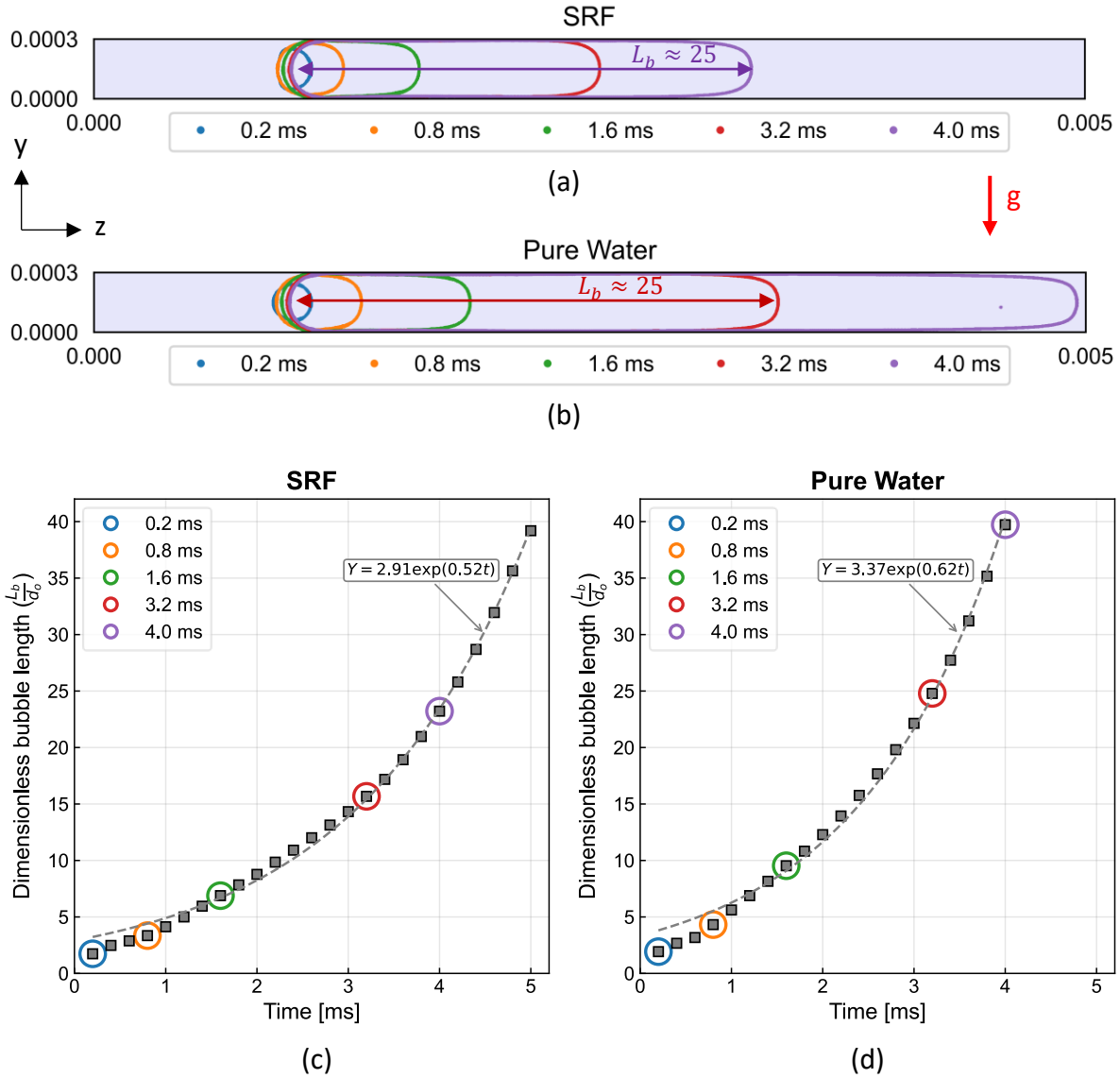

Figure 5-6: Visual illustration of the two-phase interface for case 5 and 12 (SRF and Water with $\dot{q}$ = 20 kW/m²); (a) The SRF (case 5) and (b) pure water (case 12); as well as the plotted dimensionless bubble length (L_b/D_0) for case 5 and 12; (c) SRF and (d) Pure water.

Figure 5-6(a) and (b) illustrate the bubble growth from clogging to rapid expansion as mentioned above. The diagrams show the that the bubble developed as expected and that the pure water case had a higher growth rate than the SRF. This is confirmed when looking at the plotted dimensionless bubble length in (c) and (d). As an example, note that the SRF fluid reached a non-dimensional bubble length of approximately 25 after 4 ms (purple circle) whereas the water reached the same bubble length (≈ 25) after only 3.2 ms (red circle). To better represent the bubble growth rate, an exponential line was fitted through the bubble length data using the equation $Y = ae^{bt}$, where b represents the growth rate measure. The variable a is known as the scaling factor and does not affect the growth rate of the function, rather it shifts the function up and down and dictates in which direction it grows. For this reason, a was solved for each case allowing the exponential line to fit the data accurately while only b was compared. This is shown in both (c) and (d) by the dotted grey lines. The SRF fluid had a growth rate measure of b = 0.52 whereas the water had a growth rate measure of b = 0.62, indicating again that the water had a higher bubble growth rate than the SRF. However, this is only for one heat flux. The bubble lengths and bubble growth rates for all the tests are shown in Figure 5-7 and Figure 5-8.

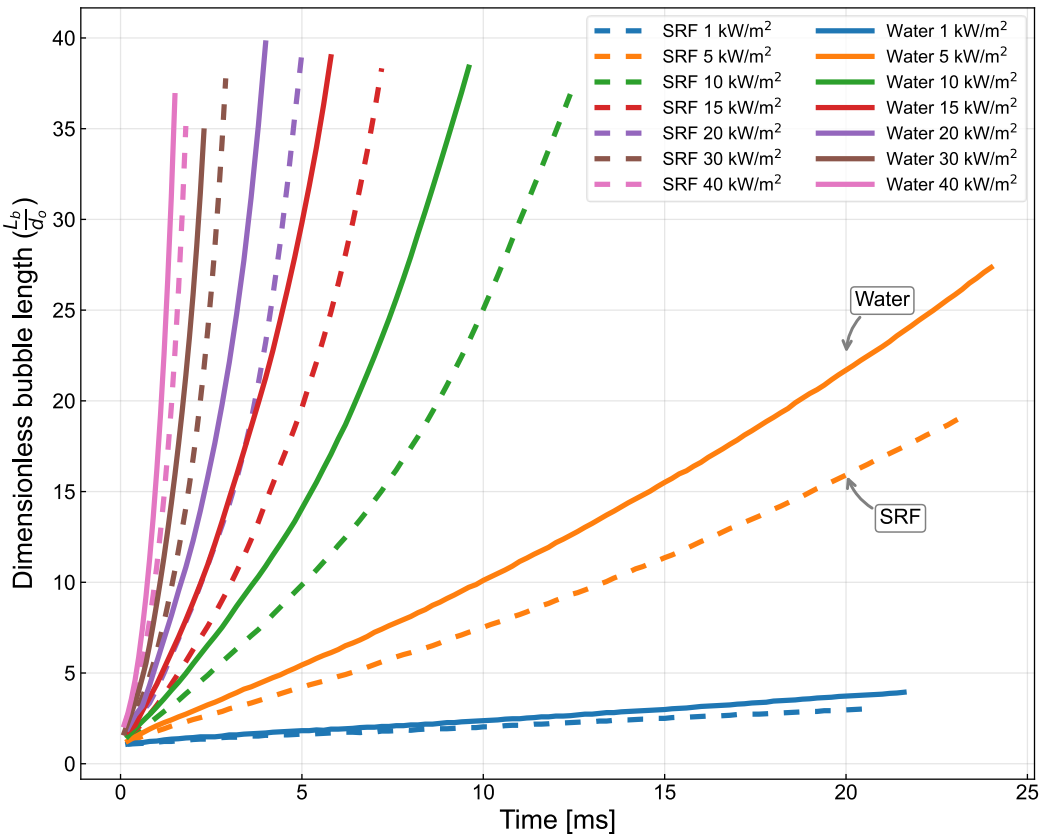

Figure 5-7: Graph showing the dimensionless bubble length of both the water and SRFs for bottom wall heat fluxes from 1 kW/m² to 40 kW/m².

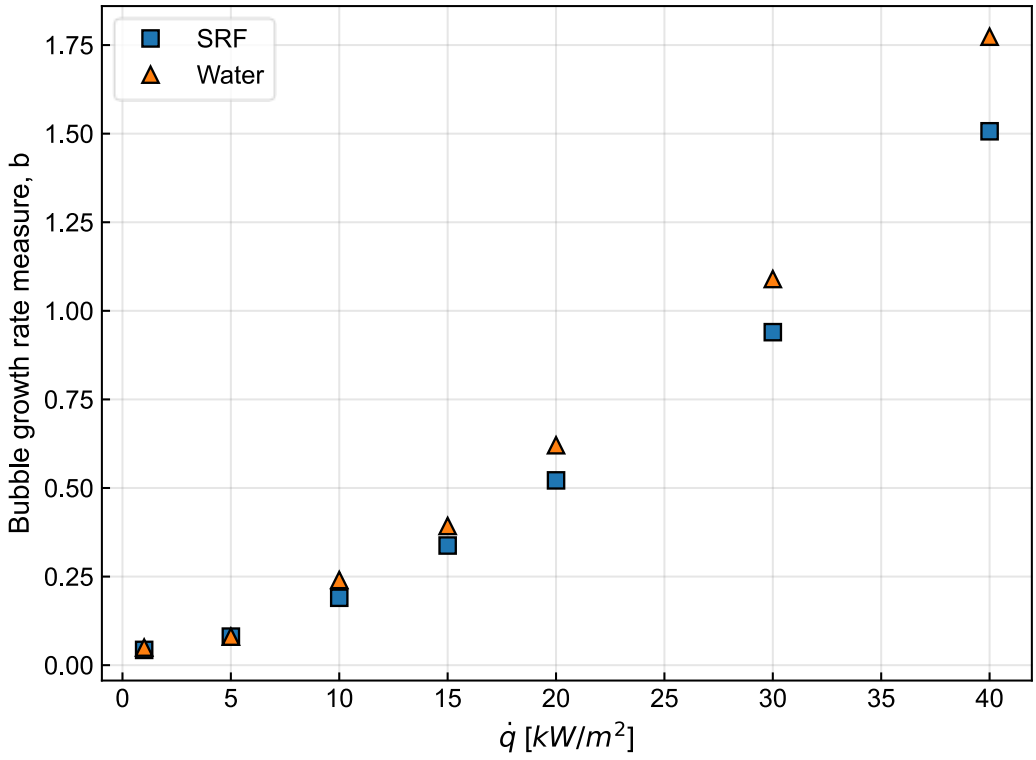

Figure 5-8: Graph of the bubble growth rate measure for the Water and the SRF with bottom wall heat fluxes from 1 kW/m² to 40 kW/m².

Figure 5-7 compares the bubble lengths between the two fluids at different bottom wall heat fluxes. The square markers represent the SRF whereas the triangle markers represent the water. A non-dimensional bubble length of 40 indicates that the bubble had filled the entire domain. All the cases with heat flux larger than 10 kW/m² had filled the entire channel even though the last data point may not have a non-dimensional length of exactly 40. This discrepancy is due to the data being stored based on flow time-steps and not on bubble location. When the bubble leading edge exited the outlet, the energy equation diverged due to reverse flows trying to force liquid into the vapour region, and the simulation stopped. The dataset stored before this divergence occurs was used as the final dataset to ensure that the numerical errors caused by the diverging energy equation did not have an impact on the results. On the other hand, the 1 kW/m² and 5 kW/m² cases did not fill the entire domain within the 48-hour simulation time constraints. The 1 kW/m² case hardly experienced any growth with a near linear trend. Other than the simulation time constraints, this also shows that too little heat was added to experience bubble growth. This matches with the experimental results obtained by Venter [3] who found that two-phase flow boiling only occurred at heat fluxes above 10 kW/m² for the 5% v/v 1-butanol-water solution. It should also be noted that as the heat flux increased and the bubble growth increased, less time-step data points were obtained (i.e. the residence time of the bubble was reduced). The timestep sizes for the 30 kW/m² and 40 kW/m² cases were reduced from 2E-07 to 2E-08 to cope with this reduction in data.

It should be noted that at most of the timestamps, the water had a longer bubble than the SRF across the heat fluxes. This also correlates to a higher bubble growth rate for the water than for the SRF, shown by the gradient of the curves, and by Figure 5-8. This is contrary to what was observed by Wei et al. [2] who found that the SRF, in their case a 0.2 wt.% heptanol-water solution, had a higher bubble growth rate than the water. However, their study included the effects of dry-out regions at the wall by initializing the bubble on the wall and not in the fluid. These dry-out regions, which were smaller in the case of the SRF due to the Marangoni effect, were responsible for the higher growth rate of the SRF. This is due to the additional effects of wall friction resisting the flow movement, as well as the dry-out region preventing more fluid to change phase. Their study does not describe how the bubble growth would be affected if there was no dry-out region. The author believes that it is the Marangoni effect, driven by the surface tension gradient between the phases, that causes the water to have a larger bubble growth rate than the SRF for the current study. The surface tension gradient at the interface is larger for the SRF fluid which draws fluid towards the interface, restraining the expansion of the vapour-region. To better understand this, the velocity of the bubble interface and the surrounding fluid is investigated.

5.4.2 Bubble Velocity

The velocity of the bubble interface, or interfacial velocity, is important in understanding what causes the difference in bubble growth rate. The interfacial velocity is obtained by measuring the velocity components along the two-phase interface. The surrounding fluid velocity, or free stream velocity U, of 0.0156 m/s was subtracted from the local z-component of the interfacial velocity to obtain the relative interfacial velocity. Case 5, illustrated in Table 5-4 using the SRF and 20 kW/m² applied heat flux, was used as an arbitrary example to illustrate how the interfacial bubble velocity looked on the upper and lower halves of the bubble, with a visual illustration in Figure 5-9.

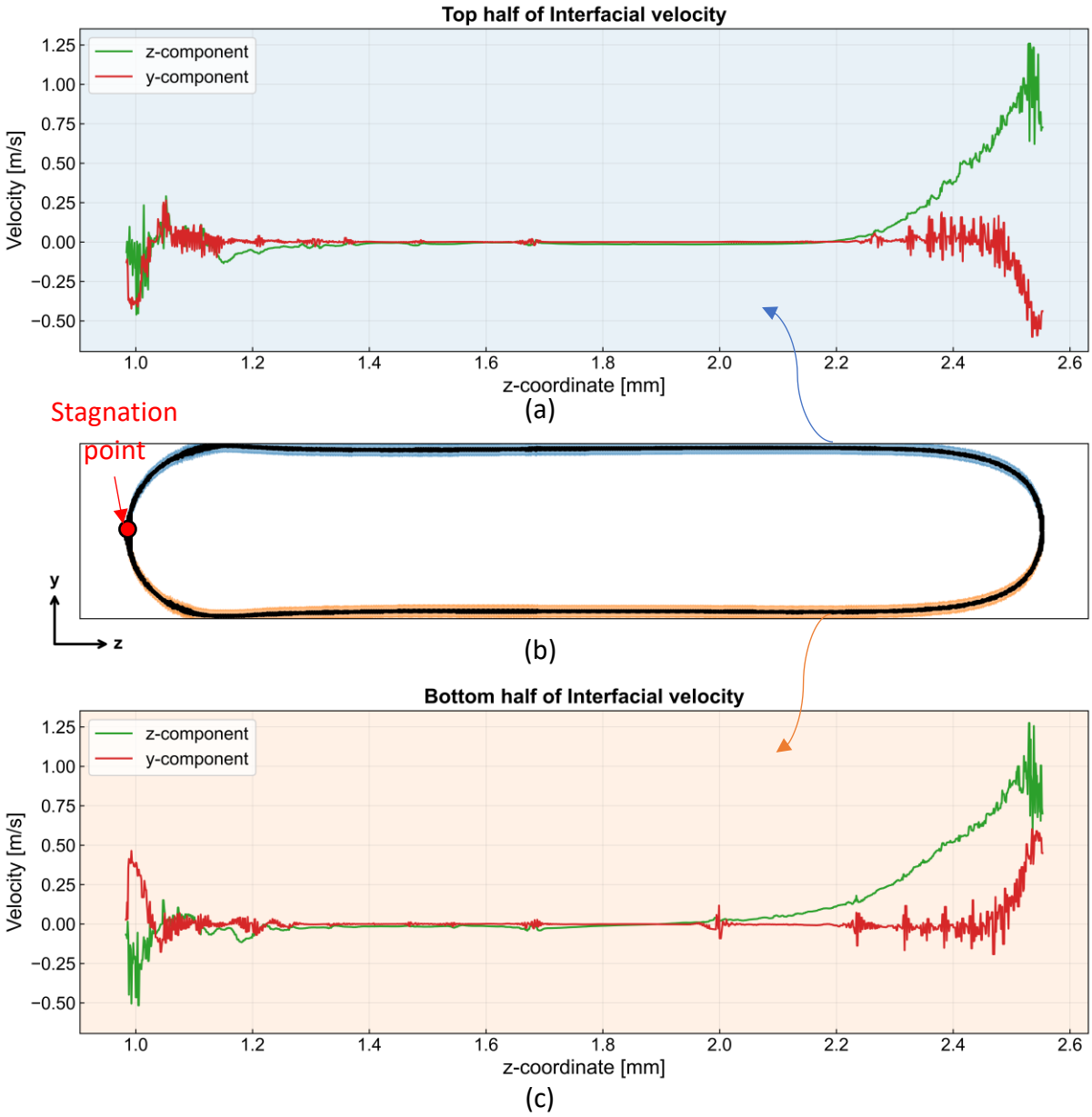

Figure 5-9: Interfacial velocity of Case 5 (SRF with $\dot{q}$ = 20 kW/m²) at t = 3.2 ms. (a) Interfacial velocity of the top half of the interface (shown in blue); (b) The bubble interface; (c) the interfacial velocity of the bottom half of the interface (shown in orange).

As the data shows, the interfacial velocity at the leading edge and trailing edge of the bubble is much larger than the velocity in the thin film near the wall. As a reminder, the free-stream fluid velocity was calculated in the validation study to be 0.0156 m/s by using:

$$U = u_{avg} = \frac{G}{\rho_l} \tag{5-2}$$

Figure 5-9 shows that the interfacial velocity at the leading edge is nearly 100 times greater than the free-stream velocity. This illustrates the rate at which these bubbles grew. It was also noticed that the z-components for both the top and the bottom halves of the interface had peaks near the trailing-edge in the negative direction. This indicates bubble growth upstream as expected during rapid expansion. The y-component of the top and bottom halves of the

interface have opposing trends. At the trailing edge, the top half has a negative y-component of the velocity while the bottom half has a positive y-component. The same is seen at the leading edge with the top half having a negative y-component and the bottom half having a positive y-component. These trends follow the shape of the interface which explains the opposing trends. It is also noted that a stagnation point forms on the centreline of the bubble trailing edge, where the fluid velocity and the interfacial velocity z-components oppose each other.

The velocity z- and y-components for both the top and bottom half of the interface shown in Figure 5-9(a) and (c) respectively, were then used to obtain local velocity magnitudes for the two interfacial halves. To capture the direction of the local interfacial velocities, the z-components were used to obtain a unit vector. Equation (5-3) illustrates how this was achieved:

$$u = \sqrt{u_z^2 + u_y^2} \times \frac{u_z}{|u_z|} \tag{5-3}$$

Here $|u_z| = \sqrt{u_z^2}$ is the absolute z-component of the velocity.

This allowed for a direct comparison of the local interfacial velocity between the SRF and the pure water. Figure 5-10 illustrates a direct comparison of the local interfacial velocity between case 5 and 12 at a flow time of 3.2 ms calculated using equation (5-3).

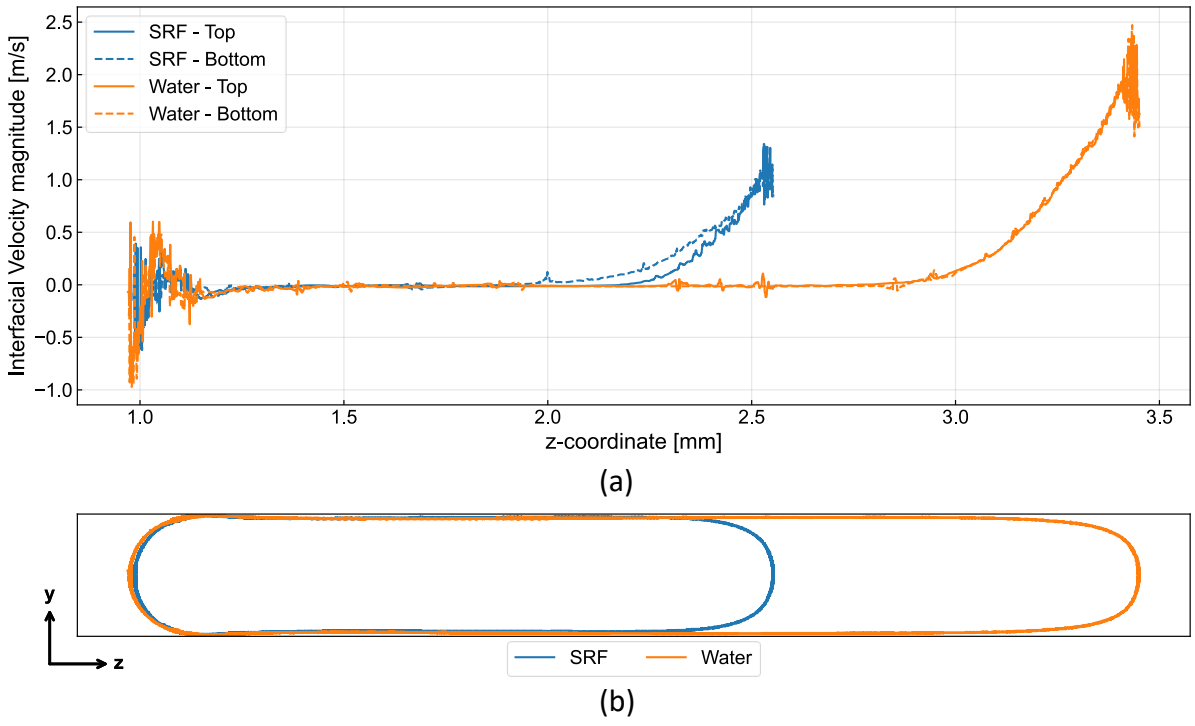

Figure 5-10: (a) Interfacial velocity magnitude of the top and bottom halves of the bubble interface for case 5 and 12 (SRF and Water with $\dot{q}$ = 20 kW/m²) at t = 3.2 ms with (b) an illustration of the respective vapour slugs. Positive velocities indicate flow along the positive z-axis.

It should be noted that both fluids experienced similar trends of the velocity magnitude, however the water experienced larger peak magnitudes at both the leading and trailing edges. This correlates to the expansion rate of water being greater than that of the SRF. It

should also be noted that the peak positive interfacial velocities are near the front of the leading edge while the peak negative interfacial velocities are near the rear of the trailing edge. Furthermore, it should be noted that the SRF experienced different interfacial velocity magnitudes at the top and bottom interface while the water did not. This is observed near the leading edges in Figure 5-10 with the dashed blue line above the solid blue line for the SRF case, whereas the dashed orange line and solid orange line for water lie on top of each other. When investigating these velocity magnitudes at different flow timestamps it was observed that as the vapour slugs grow, the interfacial velocity magnitude of the top and bottom interface at the leading edge fluctuated from larger velocity magnitudes observed at the top compared to larger velocity magnitudes observed at the bottom interface. As the vapour slugs continued to grow, the fluctuations diminished, and the variance in velocity magnitude between the top and bottom interface reduced to nearly zero, thus looking like the water results in Figure 5-10. This pattern was observed for both the water and SRF and can therefore be explained by the instabilities during the initial stages of rapid bubble growth.

To compare the interfacial velocities of all the cases, the average velocity magnitude was obtained. This is done by finding the average z- and y-components and then using Eq. (5-3) to find the corresponding magnitude. However, Figure 5-10 indicates that because the leading-edge experiences very large velocity components, these averages would not illustrate the flow at the trailing edge. The peak interfacial components at the leading edge and trailing edge were also obtained to compare the velocities at these locations. When comparing the average results, it was noted that the y-components only really contributed to the velocity magnitude in the first 0.8 ms of simulation where the bubbles expanded until clogging. Thereafter, the z-components where the dominant component in the fluid velocity. This is illustrated in Figure 5-11 where the average interfacial velocity magnitude on the bottom interface is compared to the z-component of the interfacial velocity on the bottom interface for case 5 and 12.

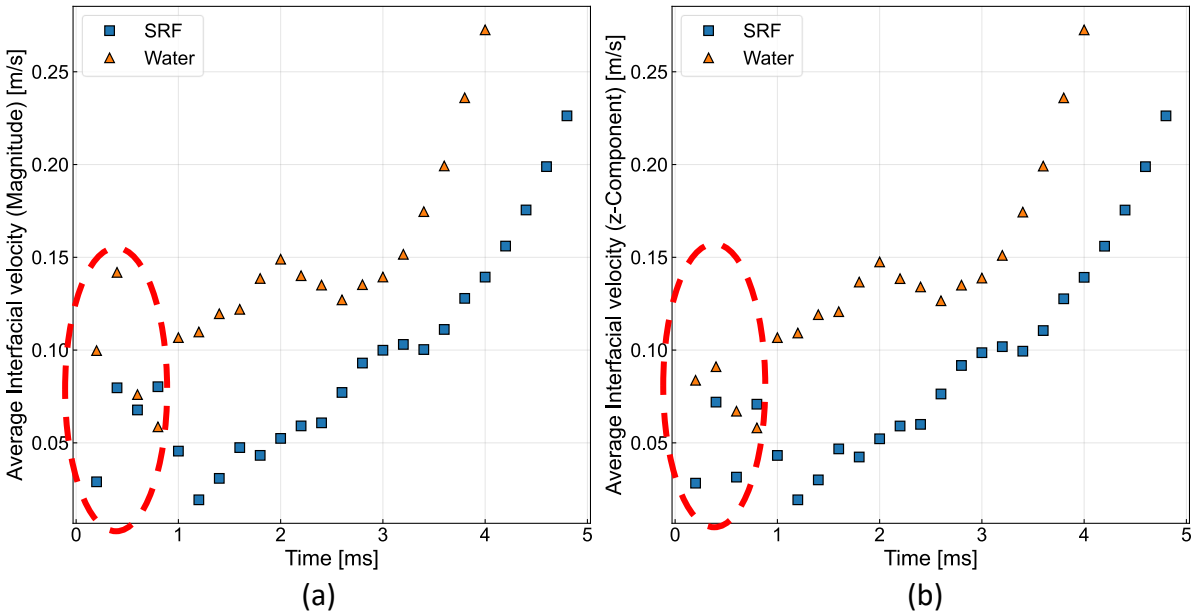

Figure 5-11: The average interfacial velocity for Case 5 and 12 (SRF and Water with $\dot{q}$ = 20 kW/m²) of the bottom half of the interface. (a) Average velocity magnitude; (b) Average velocity z-component. The red dashed ellipses indicate the timestamps where the magnitude of the velocities and z-component of the velocities differ.

The interfacial velocities for the bottom interface were used for the comparison as this where the heating was applied. As mentioned previously, the discrepancy in interfacial velocity between the top and bottom interfaces fluctuated in the early stages of the flow and then reduced to nearly zero as the flow progressed, therefore similar results are expected when looking at the top interface. The slight differences between the magnitude and the average z-component are shown by the red dashed ellipses. Slightly larger velocity magnitudes are observed for both fluids between t = 0.2 and t = 0.8 where the bubble grows until clogging. Thereafter, the z-component matches the magnitude. Because of these small differences, the z-components of the interfacial velocities were used instead of the velocity magnitudes to compare the average, peak leading-edge, and peak trailing-edge interfacial velocities between the top and bottom interfaces. The peak leading-edge and peak trailing-edge interfacial velocities are the maximum interfacial velocities found on the leading and trailing edge respectively, for both the top and bottom interfaces. As an example, case 5 and 12 are compared below in Figure 5-12.

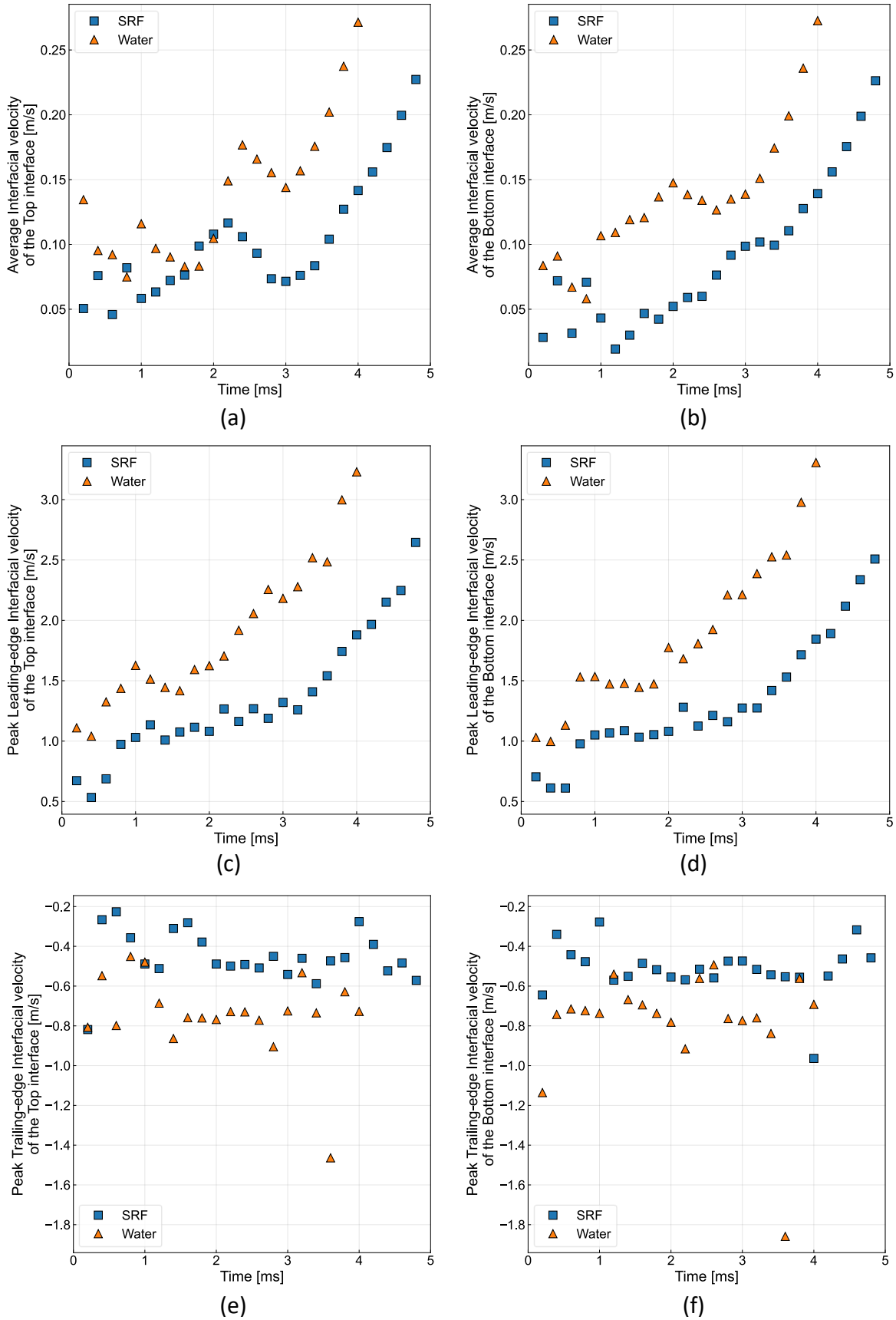

Figure 5-12: Case 5 and 12 (SRF and Water with $\dot{q}$ = 20 kW/m²) interfacial velocities when considering; (a-b) The average velocity; (c-d) The peak leading edge velocity; And (e-f) the peak trailing edge velocity of the top and bottom halves of the interface respectively.

Figure 5-12 illustrates the average interfacial velocity, the peak leading edge interfacial velocity, and the peak trailing edge interfacial velocity for cases 5 and 12 at various flow timestamps. For this heat flux of 20 kW/m², it can be noted that the water experienced larger interfacial velocities than the SRF. This is shown by the larger positive values in figures (a) to (d), and the larger negative values in figures (e) to (f). It is also important to note that the large values for water at t = 3.6 ms in figures (e) and (f) can be considered outliers as they are peak velocities ascribed by a single point on the interface and not averages, unlike those in figures (a) and (b). These peak velocities at the leading edge and trailing edge are not used for their specific values, rather for the trend they provide per case. Thus, what can be noted from figures (c) to (f) is that the water had a greater interfacial velocity in general than the SRF.

Finally, a time-average of the results in Figure 5-12 (a) – (f) was obtained along with the other 12 test cases. Obtaining a time-average of the results was required to accurately compare the various cases to each other despite their differences in flow time. As mentioned in the Bubble growth section, the bubble growth rate can be described by an exponential function, meaning that the bubble growth rate is small in the early stages of flow while it rapidly increases as the flow progresses. It was also shown that the cases with lower applied heat fluxes experience slower bubble growth compared to the cases with higher applied heat fluxes. Comparing a single timestamp between cases with various applied heat fluxes and thus, various bubble growth rates, means that some cases may be in their initial growth stage while others may be in their final growth stage. A time-average of the results will ensure that the bubble growth stage does not play a factor in the comparison between the various applied heat flux cases. Additionally, as seen in Figure 5-12 (a) – (f), the interfacial velocities along the top and bottom interfaces differed by very little. For this reason, an overall time-averaged interfacial velocity was obtained by:

$$u_{avg,t} = \frac{u_{avg,t_{top}} + u_{avg,t_{bottom}}}{2} \tag{5-4}$$

Here $u_{avg,t_{top}}$ and $u_{avg,t_{bottom}}$ represent the time-averaged top and bottom interfacial velocities. Using this, the time-averaged average, time-averaged peak trailing edge, and time-averaged peak leading edge interfacial velocities for the different cases were obtained. These results are shown in Figure 5-13 below.

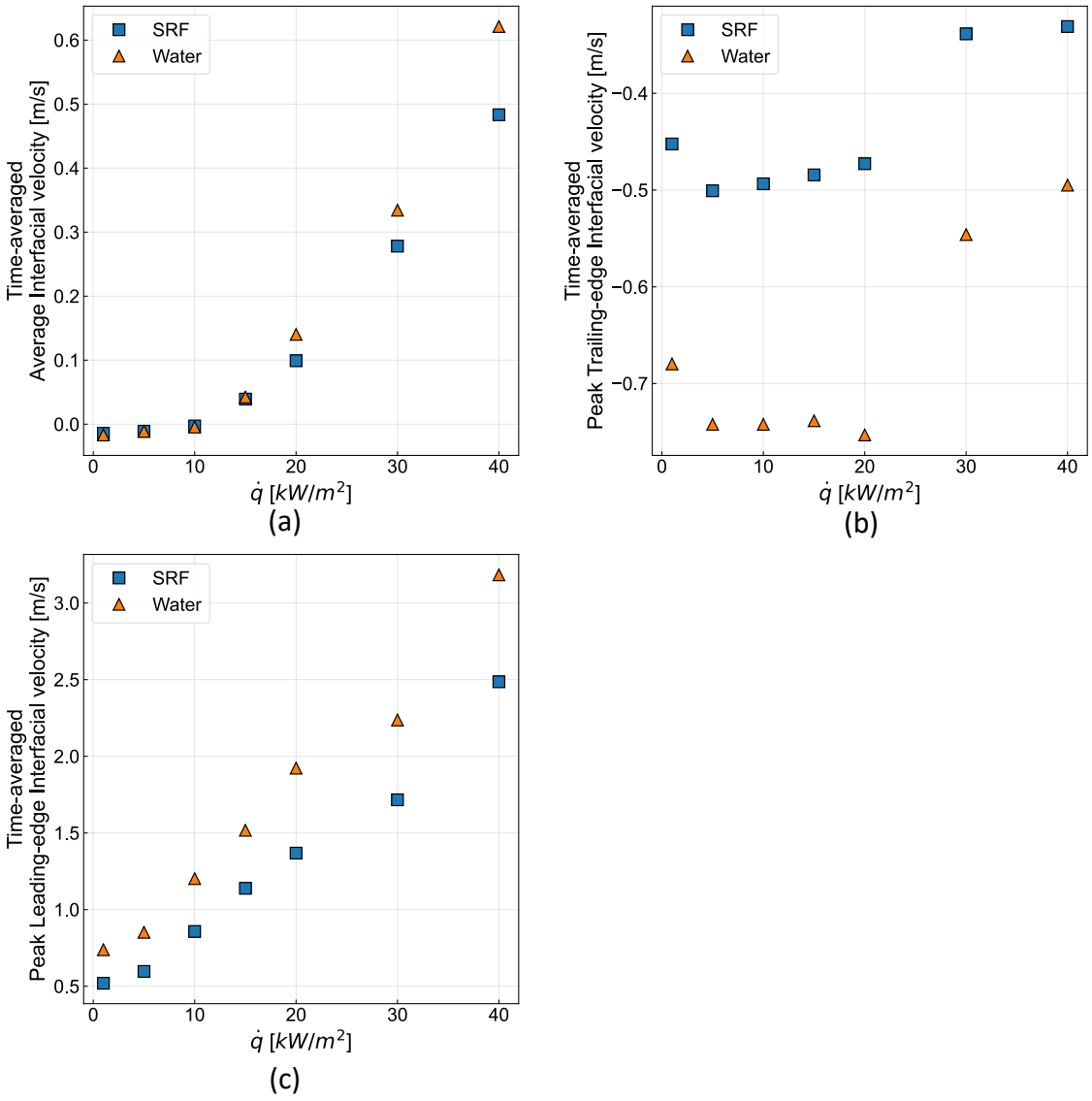

Figure 5-13: Time-averaged interfacial velocities for all cases: (a) the time-averaged, average interfacial velocity over the entire interface. (b) the time-averaged peak interfacial velocity at the trailing edge. (c) the time-averaged peak interfacial velocity at the leading edge.

As a reminder, the peak leading-edge and peak trailing-edge refer to the maximum interfacial velocities along the leading and trailing edges of the interface respectively. The time-averaged average interfacial velocity in (a) shows that as the heat flux increases, the overall bubble interfacial velocity increases. This is expected as adding more heat will increase the rate of evaporation and thus the rate at which the bubble expands. It should be noted that the water experienced a larger average interfacial velocity than the SRF, which correlates to what was observed by the bubble growth rates. This is particularly true at larger heat fluxes. Again, when looking at the time-averaged peak trailing edge (b) and time-averaged peak leading edge (c) velocities it should be noted that the trends are more important than the values. From both, it again shows that the water experienced greater interfacial velocities than the SRF. What is interesting is that as the heat flux increases, the trailing edge velocity seems to decrease. This may be caused by an increased “pulling” from the leading edge due to its drastically larger velocities at higher heat fluxes, however average values instead of peak

values at these locations would be better suited to draw those conclusions. What is important though is that all three methods of looking at the interfacial velocities confirm what was observed by the growth rates.

Studies by Mukherjee et al. [56], Saha et al. [57] and Li et al. [58] concluded that, with similar difference in surface tension magnitudes, the surface tension magnitude did not have a significant impact on the bubble growth rates. Rather, Saha et al. [57] suggested that the surface tension magnitudes would result in slightly different bubble shapes. This confirms that the surface tension gradients, and not the surface tension magnitudes, caused the difference in bubble growth rates due the different influences on the capillary flow as described by the Marangoni effect.

5.4.3 SURROUNDING FLUID VELOCITY

It is important to also consider the surrounding fluid motion. The surrounding fluid velocity vectors for the various test cases were investigated. To keep consistent with the previous local discussions, test case 5 and 12 at t = 3.2 ms are used for demonstration purposes and were arbitrarily selected. Figure 5-14 represents an overview of the relative velocity vectors at the trailing edge of the vapour slugs for the two fluids, remembering that the relative velocity is achieved by removing the constant inlet fluid velocity (U = 0.0156 m/s) from the z-component of the velocity vector.

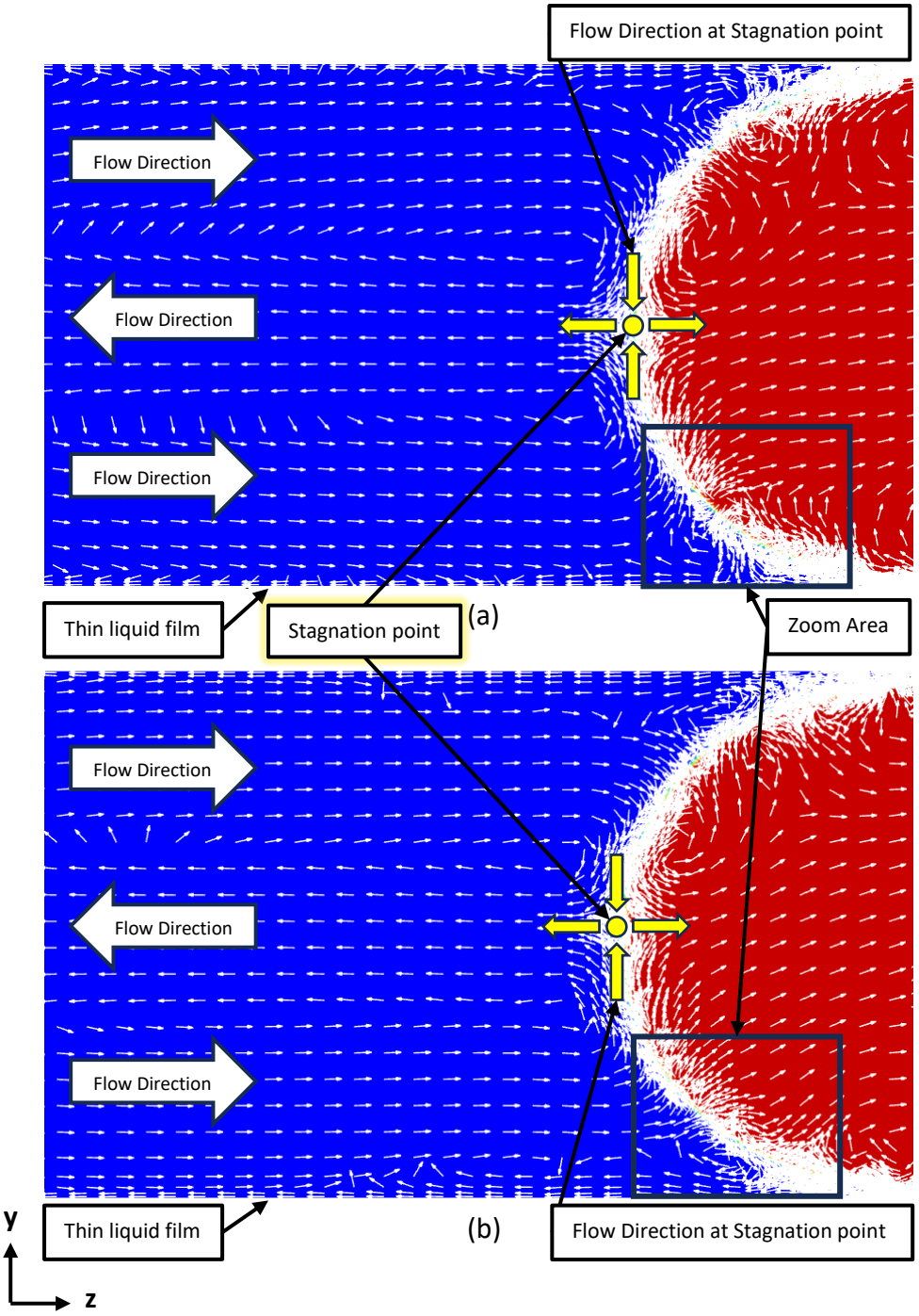

Figure 5-14: Relative velocity vectors at the trailing edges for cases 5 and 12 (SRF and Water with $\dot{q}$ = 20 kW/m²) where the blue and red represent the liquid and vapour phase respectively: (a) SRF at t = 3.2 ms and (b) pure water at t = 3.2 ms.

The purpose of Figure 5-14 is to illustrate the surrounding fluid flow upstream of the trailing edge interface. It should be noted that constant length vectors were used to illustrate the direction of the flow, rather than illustrate velocity magnitudes. Both fluids experienced very similar flow fields, with the fluid along the centreline of the channel in the opposite direction towards the inlet. Additionally, the stagnation points mentioned in the interfacial velocity discussion above are illustrated by the yellow circle and arrows. The interfacial velocity along the top interface cancels the interfacial velocity along the bottom interface at the stagnation

point. What should be noted is the direction of the fluid flow in the thin liquid film, near the wall in the inflation layers. The velocity field in this layer is thicker in the water case than in the SRF case. This does not mean that the liquid film layers are different thicknesses, rather that the velocity of the flow in the two differ. A more in-depth investigation can be done when zooming in on the area near the bubble interface and the bottom wall as shown by the zoom area rectangles. The zoomed areas are illustrated in Figure 5-15.

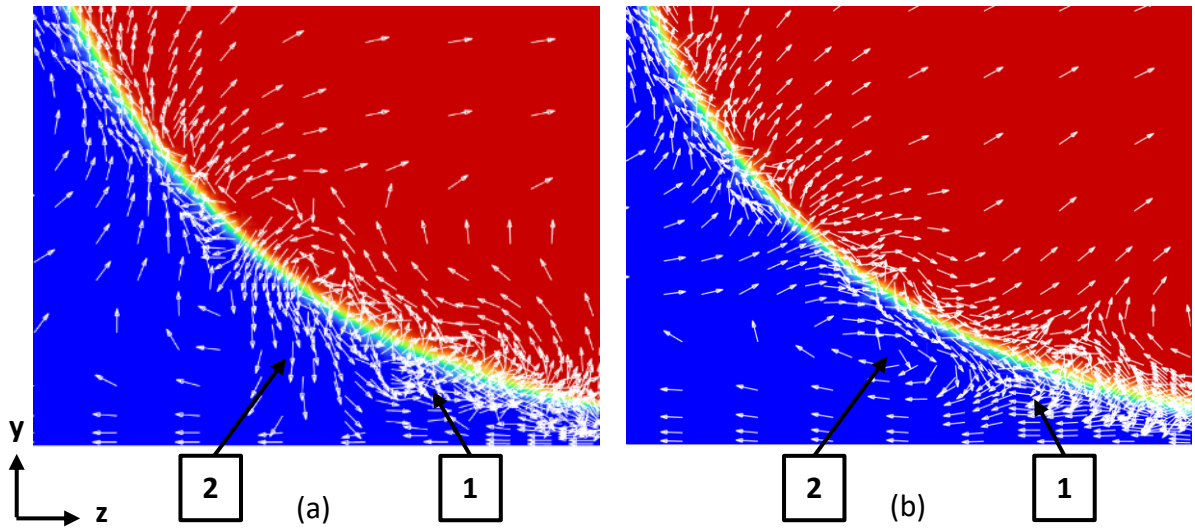

Figure 5-15: Relative velocity vectors near the interface and the bottom heated wall for case 5 and 12($\dot{q}$ = 20 kW/m²). The blue and red indicate the liquid and vapour phases respectively: (a) SRF at t = 3.2 ms and (b) water at t = 3.2 ms

Zooming in at the region near the wall, the differences between the two fluids becomes more apparent. The two major differences between the two fluids are indicated by points 1 and 2. Considering point 1, the liquid fluid flows to the right (along the positive z-axis) towards the heated surface (bottom wall) in the SRF case whereas the opposite is observed in the water case. This flow is driven by the thermocapillary force described by the Marangoni effect which clearly indicates the self-rewetting nature of the 5% v/v 1-butanol-water mixture as discussed previously. Similar observations were made by Li et al. [2] with their 0.2wt% heptanol-water self-rewetting solution. This difference in fluid flow at point 1 influences the velocity vectors observed at point 2. In the water case, the flow diverted by the bubble interface is forced away from the heated region causing a strong circulation zone to form. The opposite occurs in the SRF case. The flow in the SRF case, which is diverted from the bubble interface, is drawn towards the heated region causing a downward channel of flow to the bottom surface.

5.4.4 Film thickness

The thickness of the fluid between the vapour slug interface and the heated wall is known as the liquid film thickness, denoted by δ. Heat transfer in two-phase flows is heavily dependent on this liquid film that sits over the heated surface because this allows phase change to occur from the liquid phase to the vapour phase. The film thickness is a difficult quantity to measure, however, it was noted that all vapour slugs, after clogging, had a point of minimum film thickness and a point of inflection. The minimum film thickness occurred near the trailing

edge of the bubbles, and the point of inflection was considered as the point where the bubble began to narrow towards the leading edge. A schematic of the typical shape of the bubble slug after clogging is illustrated in Figure 5-16.

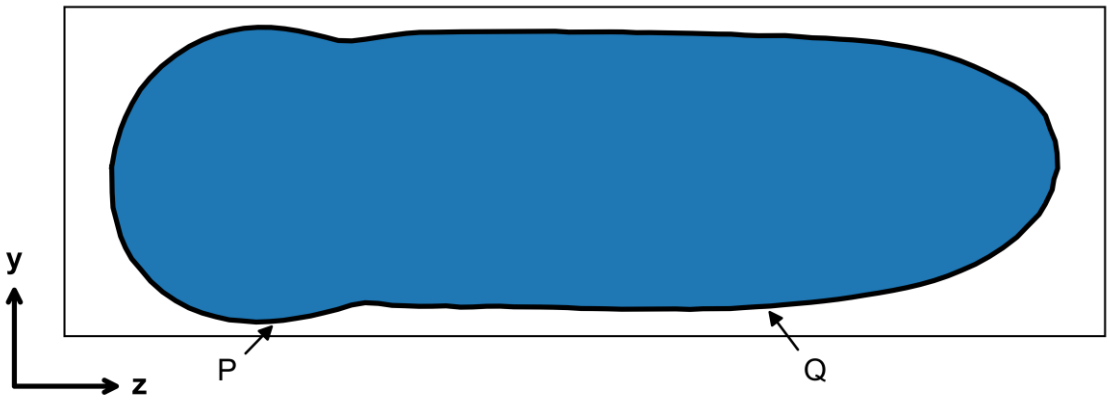

Figure 5-16: Schematic of a bubble in the horizontal channel. Points P and Q indicate the minimum film thickness and the point of inflection respectively.

Points P and Q were identified and selected to illustrate the minimum film thickness at the trailing edge and point of inflection at the leading edge respectively. This was done by looking at the concavity of the bottom half of the interface. A point of inflection is where the concavity of a line changes. Generally, for vapour slugs, the bottom half of the interface experiences two major inflection points. Considering Figure 5-16, the first inflection point is just to the right of P, where the concavity of the interface changes from concave upwards to concave downwards. The second inflection point is at Q where the concavity switches from concave downwards to concave upwards. During the simulations, it was noted that the second inflection point often occurred closer to the first point since the concave downward section was very small or very shallow. In those cases, point Q was defined as the minimum of the final concave upward section, indicating the start of the leading edge. To find these points, the derivative of the interface was obtained and the points of zero gradient were identified as these indicate local minima, maxima, and inflection points. Case 5 was used to demonstrate the process and is illustrated in Figure 5-17 below.

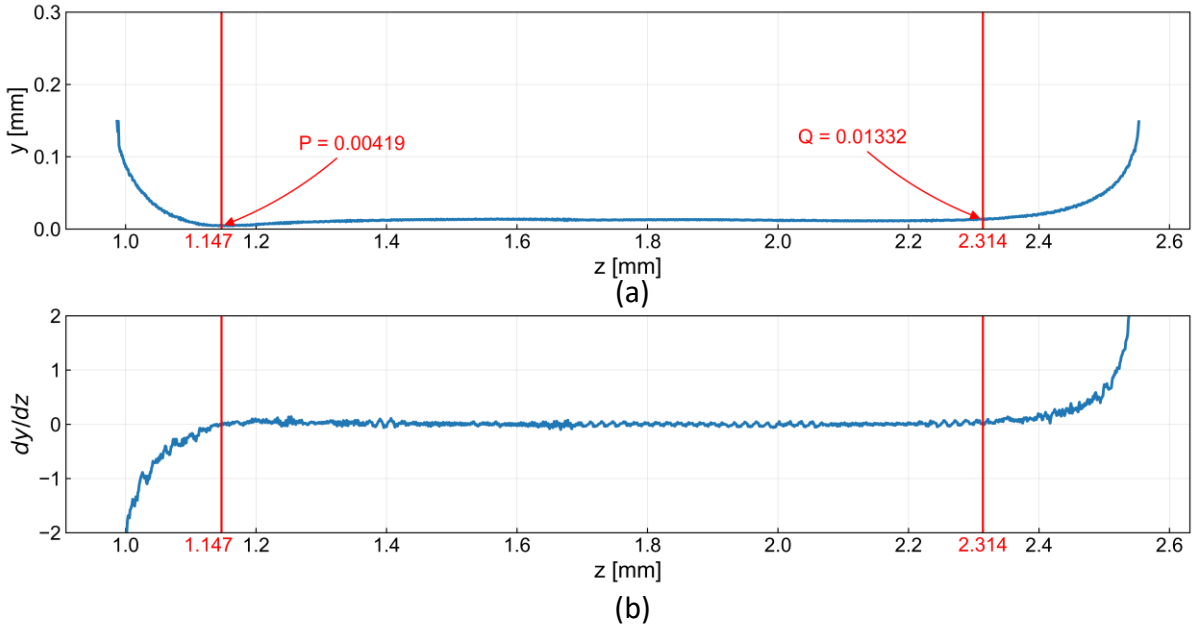

Figure 5-17: Bottom half of bubble interface for case 5 (SRF with $\dot{q}$ = 20 kW/m²) illustrating the point of minimum film thickness, P, and point of inflection, Q: (a) The bubble interface with the y coordinates representing the film thickness δ and (b) the derivative of the bubble interface dy/dz.

In Figure 5-17(a), the top and bottom borders of the figure represent the upper and lower walls of the channel. It can therefore be said that the y-coordinates represent the film thickness, δ, of the bubble. Furthermore, the derivative of the y-coordinates, dy/dz, in Figure 5-17(b) thus represent how the interface, and the film thickness, changes along the length of the channel.

Figure 5-17 perfectly illustrates how points P and Q were tracked and obtained. It also clearly shows how the interface fluctuates and experiences many minor inflection points. Furthermore, the three concavity regions are clearly seen in (a). A maximum film thickness between point P and Q is observed between 1.4 and 1.6 mm along the z-axis. However, as mentioned previously, at different flow timestamps and different vapour slug shapes, the three concavity regions were not so easily distinguished and a local maximum between P and Q was not very clear. Point Q became the local maximum in many of those cases which further solidified the decision for using Q as the point of interest.

The film thicknesses at point P and Q were obtained over the entire flow simulation for each case with Figure 5-18 representing that of case 5 and 12.

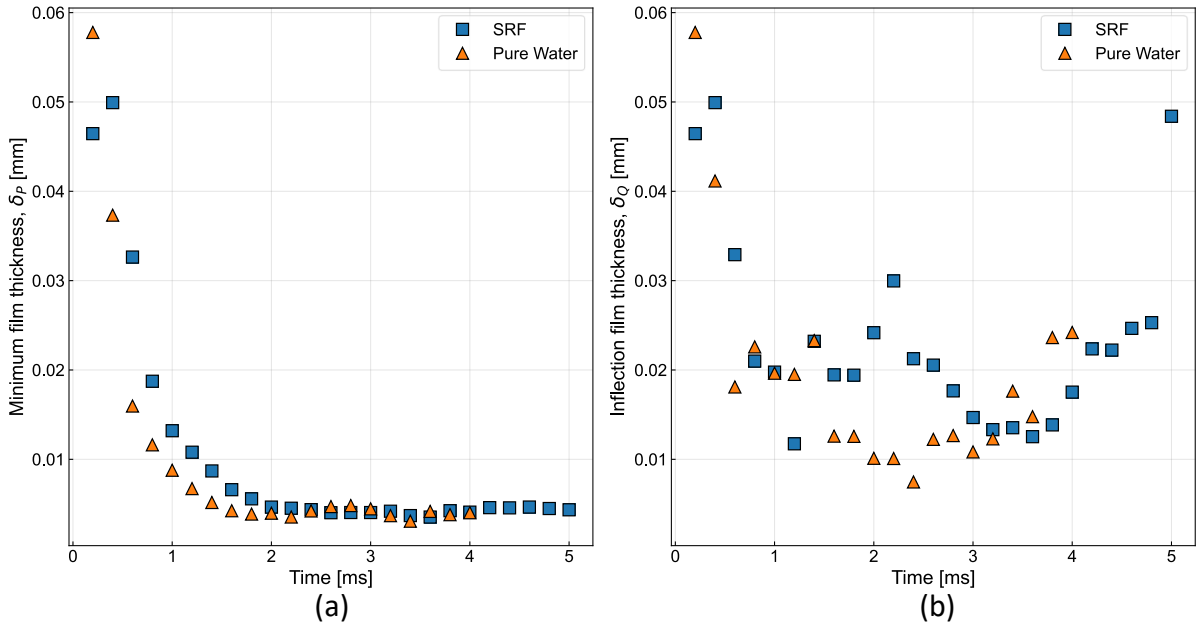

Figure 5-18: Fluid film thickness for case 5 and 12 (SRF and Water with $\dot{q}$ = 20 kW/m²) at: (a) The minimum film thickness δ_P, and (b) The inflection point film thickness δ_Q.

Figure 5-18 (a) indicates that as the bubble grows the minimum film thickness reduces. Once clogging occurs, the minimum film thickness plateaus with small fluctuations around this thickness. This is experienced by both fluids, noting that the pure water plateaus sooner than the SRF due to its higher growth rate. However, for this case, the plateaued film thickness is the same for both fluids. On the other hand, (b) shows that point Q experiences large fluctuations for both fluids. This is particularly true at the later stages of the simulation where the bubble velocity is very high. It is very difficult to observe clear trends for either fluid at point Q, however, it can be noted that most of the data points illustrate smaller film thicknesses at Q for the pure water than for the SRF.

Taking a time-average of the film thicknesses at point P and Q for the different cases allows for the comparison between the two fluids, as illustrated in Figure 5-19.

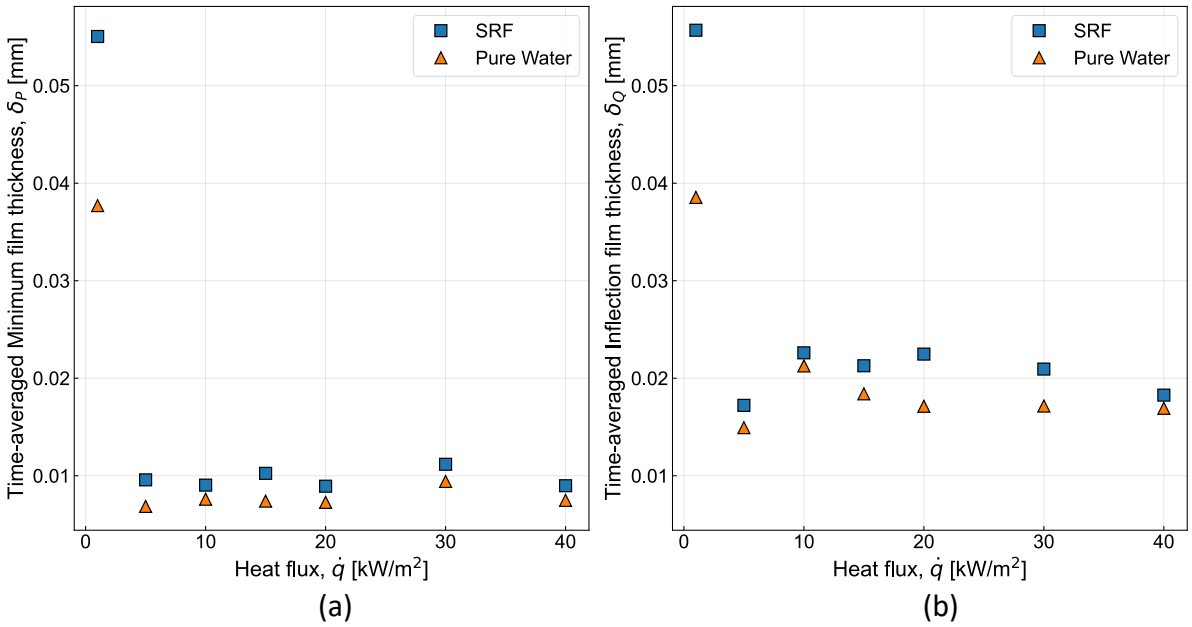

Figure 5-19: Time averaged liquid film thickness for the 14 cases at various heat fluxes: (a) The minimum film thickness δ_P, (b) The inflection point film thickness δ_Q.

Figure 5-19 (a) indicates a peak minimum film thickness at a heat flux of 1 kW/m² followed by a plateauing of the results for both fluids. The peak at 1 kW/m² is due to the little growth of the bubble and the absence of clogging as illustrated with Figure 5-7. It is expected that as the heat flux increases, the film thickness would decrease due to a higher rate of evaporation, however, according to both Figure 5-19(a) and (b), there is no clear decrease in film thickness after the 1 kW/m^2 case. This suggests that the range of heat fluxes used is too low and that higher heat fluxes could be tested. The pure water experienced a smaller minimum film thickness than the SRF everywhere. However, considering Figure 5-18 (a), this may be due to its higher bubble growth rate causing it to reach its plateau sooner and thus resulting in a lower time-averaged value.

Figure 5-19 (b) indicates a similar trend to that of (a) with the SFR having a thicker liquid film than the water everywhere. Both fluids experience fluctuating results however, the water stabilizes after about 20 kW/m² whereas the SRF decreases and comes closer to the water data. This indicates that as the heat flux increases, the SRF experiences more evaporation in the liquid film and behaves more like the water. The results indicate that the SRF had a thicker liquid film between the vapour slug and the heated wall. Since surface tension is the only property that differs between the two fluids, this difference in film thickness is due the capillary forces described by the Marangoni effect. The self-rewetting nature of the SRF draws more fluid into the heated region than the water, causing a thicker liquid film (refer to Figure 5-15). Unfortunately, due to the fluctuating nature of the results, the data should not be extrapolated and thus a prediction cannot be made for the film thickness at heat fluxes above 40 kW/m².

5.5 HEAT TRANSFER

When investigating the heat transfer capabilities of a flow system, the convection heat transfer coefficient is typically used by rearranging Equation (2-1). In studies where the heat transfer in a two-phase region is the focal point, like the current study, Eq. (2-1) is redefined to look like Equation (5-5):

$$\alpha_{tp} = \frac{\dot{q}}{(T_s - T_{sat})} \tag{5-5}$$

This requires the surface temperature and fluid temperature in the two-phase region. As a reminder, the two fluids were numerically modelled using the same saturation temperature of 100°C, which was later found to be in-accurate (see Section 5.2). The SRF was experimentally measured to have a saturation temperature of 93.5°C compared to the measured 99.74°C saturation temperature of the water. It is expected that the lower saturation temperature would reduce the simulated wall temperatures without significantly impacting the bubble film thickness, which is attributed to the capillary forces and thus, surface tension, as discussed in the previous section. Since both the SRF and water were modelled with the same saturation temperature, it follows that any difference in the heat transfer coefficient can be attributed to the surface tension, and thus, self-rewetting. Again cases 5 and 12, the SRF and Water with $\dot{q}$ = 20 kW/m² cases from Table 5-4 respectively, are used for demonstration purposes in this section. The difference in local wall temperature and saturation temperature for cases 5 and 12 at various timestamps are illustrated in Figure 5-20.

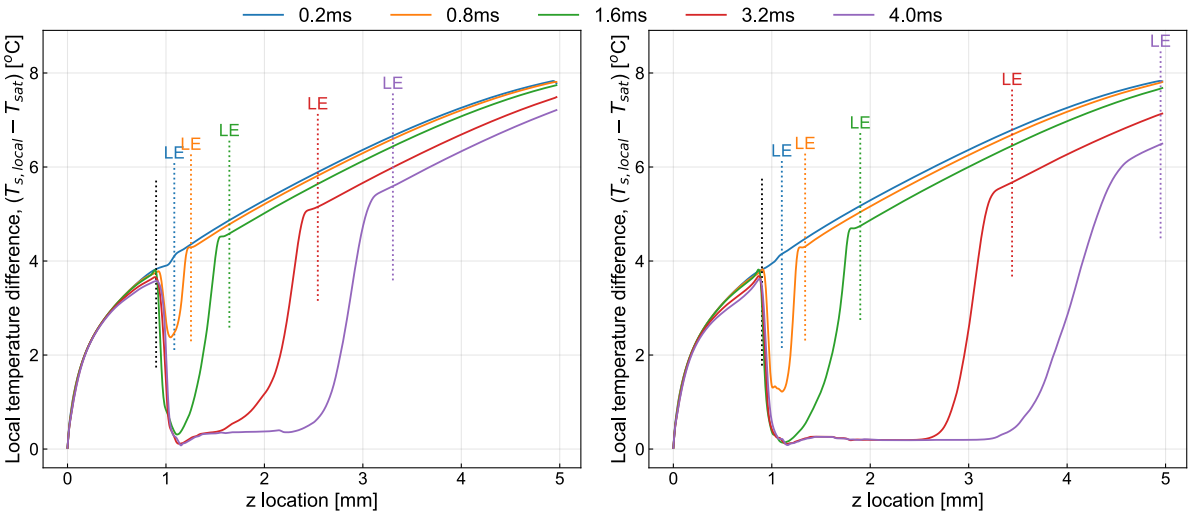

Figure 5-20: Difference in Local wall temperature and saturation temperature for case 5 and 12 (SRF and Water with $\dot{q}$ = 20 kW/m²) at various timestamps. The start and end of the two phase-regions are indicated by the dotted vertical lines with labels TE and LE respectively: (a) The SRF and (b) pure water.

The local difference in wall temperature and saturation temperature is illustrated since the fluid temperature is always greater than saturation temperature. With the saturation temperature remaining constant, the trend observed for the temperature difference results is the same as the trend observed for the local surface temperature results. As the vapour slugs clog the channel, the local surface temperatures reduce to near saturation temperature.

This is illustrated by the troughs of each curve where the bubble trailing edge clogs the channel. It should be clear that the dotted lines with labels LE and TE indicate the leading edge and trailing edge of the vapour slugs, thus representing the two-phase region in between. In the two-phase region, the local surface temperature decreases towards saturation temperature and plateaus depending on the length of the vapour slug. In front of the vapour slug, to the right of the LE, the local surface temperature follows a similar trend to the initial surface temperature but with lower values (smaller temperature differences). This indicates that the growth of the vapour slug effects the surface temperature ahead of the slug as well, which is expected. The local surface temperatures of the two fluids follow very similar trends, however the water seems to plateau at slightly lower temperatures. The lower plateau is attributed to the smaller film thickness of the water as illustrated earlier.

The saturation temperature was used for the fluid temperature in the two-phase region, as shown in Eq. (3-28), therefore the local fluid temperatures were not separately illustrated. Instead, the local heat transfer coefficient over the two-phase region was calculated and is illustrated Figure 5-21.

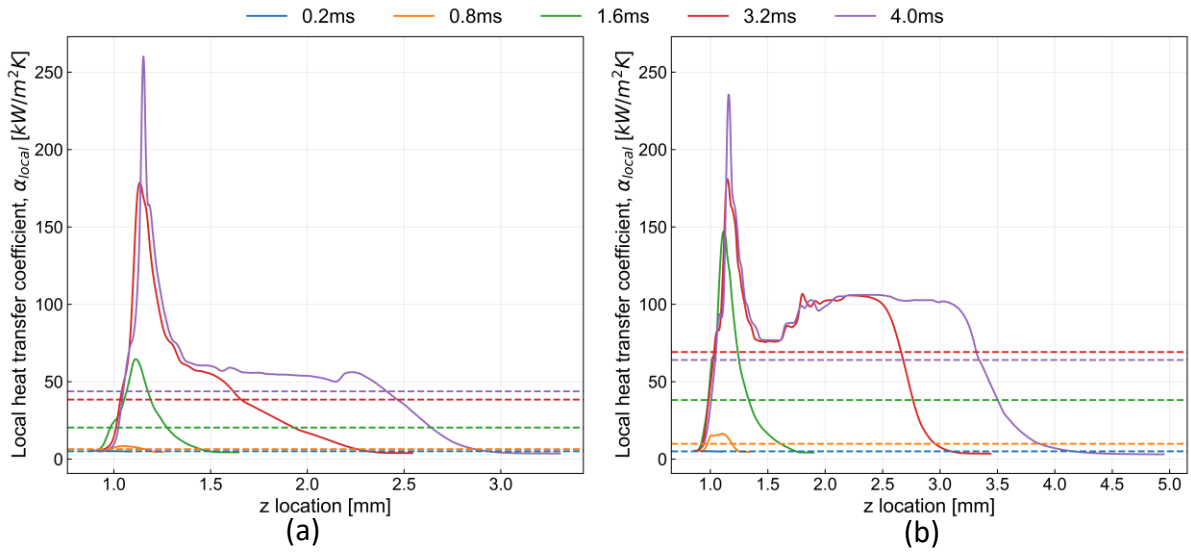

Figure 5-21: Local heat transfer coefficient of case 5 and 12 (SRF and Water with $\dot{q}$ = 20 kW/m²) at various timestamps. The dashed lines indicate the area-average local heat transfer coefficients for each timestamp: (a) The SRF and (b) pure water.

The local heat transfer coefficient has a peak near the trailing edge of the bubble, which correlates to the trough found in the local surface temperature results. This should be expected as the temperature difference between the fluid and the surface is the smallest here resulting in a larger heat transfer coefficient. As the vapour slug grows and gets closer to the heated wall of the channel, the surface temperature gets closer to saturation temperature and the local heat transfer coefficient drastically increases. After this point, the local heat transfer coefficient plateaus as the vapour slug expands downstream. The plateau is a result of the area of the heated surface that cools to saturation temperature increasing. Comparing the red (t = 3.2 ms) and purple (t = 4 ms) curves in (a) and (b), both experience similar plateaus of the heat transfer coefficient. As the simulation continued to progress, similar values of the plateaus were observed. The area-averaged local heat transfer coefficient over

the bottom heated wall was obtained for each timestamp throughout the simulation and the results are indicated using dashed lines. It can be noted that as the simulation progresses, the average heat transfer coefficient increases. This, however, does not occur in (b) as shown by the t = 3.2 ms and t = 4 ms lines. Instead, the heat transfer coefficient for the purple curve after the plateau is longer than that of the red curve due to the leading edge being long a thing, which brings down the average. It should also be noted that the water case experienced higher plateaus than the SRF which correlate to the area where the liquid film thickness in the water was thinner.

The area-average heat transfer coefficient for both case 5 and 12 were compared over their respective flow times in Figure 5-22.

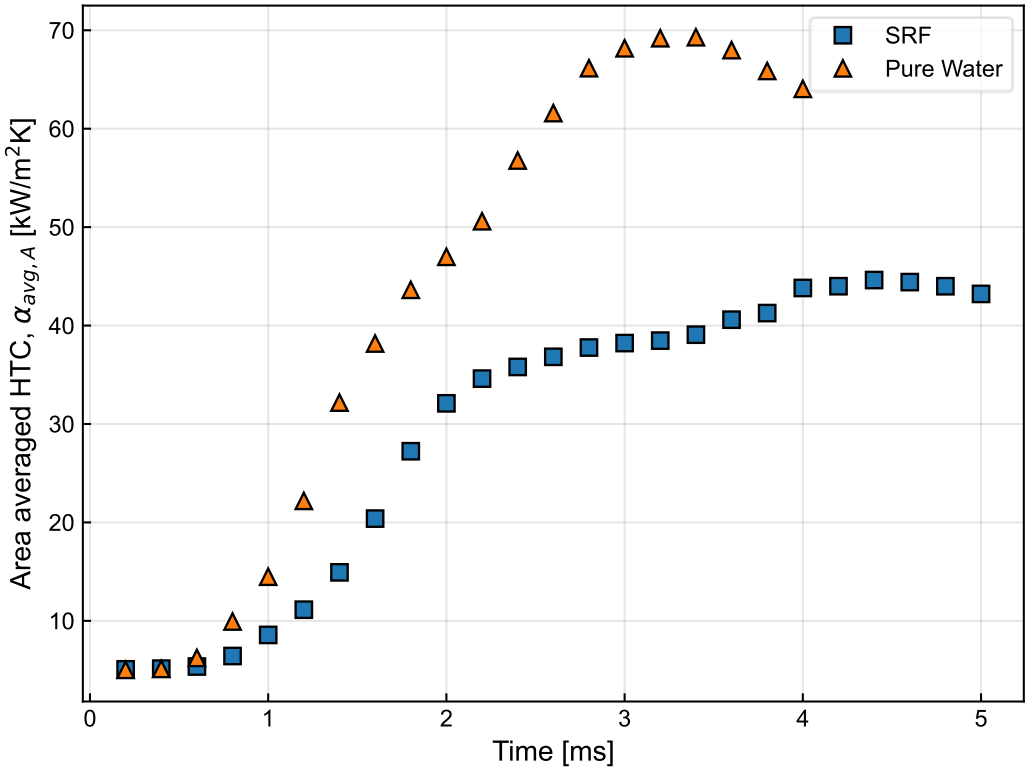

Figure 5-22: Area-averaged heat transfer coefficient for case 5 and 12 (SRF and Water with $\dot{q}$ = 20 kW/m²)

The data shows that as the simulation progresses and the vapour slug grows, the heat transfer coefficient increases. The increase in heat transfer coefficient is due to the surface temperature decreasing, indicating that more fluid has changed phase. It should be expected that as the vapour slug continues to grow, the average heat transfer coefficient should begin to plateau. Figure 5-20 above illustrated this by showing that the area of the heated wall that cooled to near saturation temperature, increased as the vapour slug grew. The SRF case above shows this trend with a slowed rate of increase in heat transfer coefficient near the end of the simulation. The pure water case on the other hand experienced a more drastic increase in average heat transfer coefficient, with less of a plateau and a sudden drop-off near the end. The rapid growth of the bubble in the water case caused a long, thin leading edge which resulted in the drastic drop-off near the end of the simulation. The thinner the leading edge

is, the thicker the liquid layer, and the less fluid changes phase causing larger surface temperatures. A slower drop-off is experienced in the SRF case due to its reduced growth rate. As mentioned previously, the rapid bubble growth rate of the water case means that less data points were captured to investigate the bubble heat transfer as it grew compared to the SRF case. This difference in available data points between the two fluids means that the fluid with less data points has a smaller pool from which it can take averages. This may also cause slight differences in the results such as the steep drop-off.

The time-averaged heat transfer coefficients and the time-averaged difference in wall temperature and saturation temperature for all 14 heat flux cases on the bottom heated wall was calculated and illustrated in Figure 5-23.

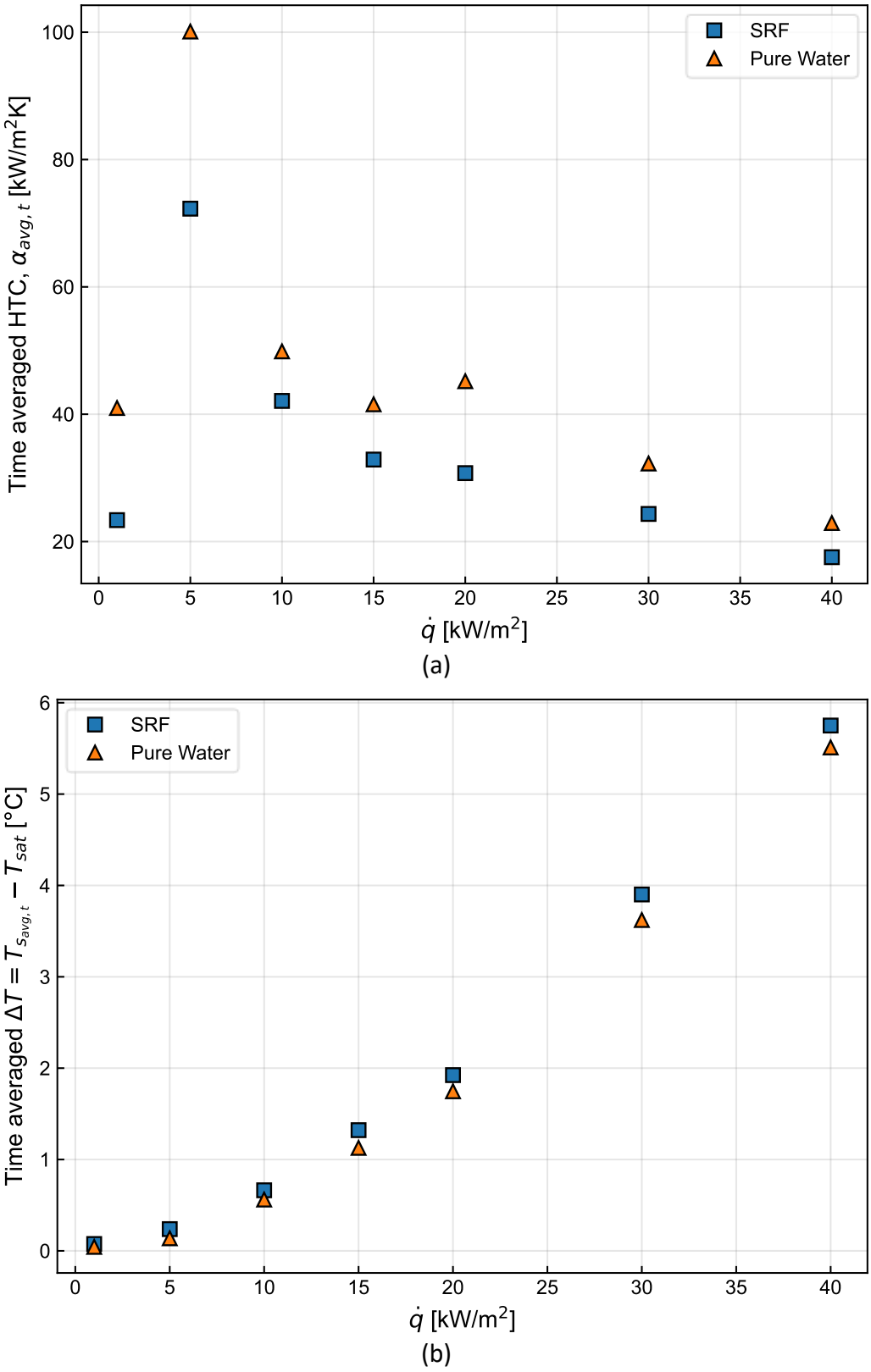

Figure 5-23: Time-averaged data of all 14 cases with varying heat fluxes: (a) Heat transfer coefficient and (b) the difference between the wall temperature and saturation temperature.

The bottom surface was investigated as this is where heating was applied and thus where the heat transfer coefficient is expected to the most profound. The time-average heat transfer

coefficient indicates that as the heat flux increases, the heat transfer coefficient decreases. At 1 kW/m², the heat transfer coefficient is expected to be low as the bubble remains small and does not experience clogging. Without clogging, the liquid film separating the bubble from the heated surface remains large and the system can almost be considered single-phase. At 5 kW/m², the heat transfer coefficient peaks. This indicates that the bubble clogging has occurred and that a thin film layer is present. The wall temperature at this heat flux is very close to saturation temperature ($\Delta T \approx 0$), therefore a small temperature difference causes the peak in heat transfer coefficient. As the heat flux increases, the subsequent wall temperatures increase at a higher rate which cause the observed decreased relationship of the heat transfer coefficient. The shapes of the heat transfer coefficient curves are very similar to the shapes of the thin film thickness curves. This indicates that as the heat flux increases, the rate at which the thin film evaporates increases.

The results show that the water had surface temperatures closer to the saturation temperature, and thus higher heat transfer coefficients than the SRF everywhere. The same was experimentally observed by Venter [3] for a mass flux of 15 kg/m^{2}s. However, Venter also observed that at a larger mass flux of 25 kg/m^{2}s and larger applied heat fluxes, the opposite was observed and the SRF had higher heat transfer coefficients than the water everywhere. To directly compare the results from Figure 5-23(b) and the experimental results by Venter [3], a 4 mm portion from the start of the two-phase region for the experimental cases was captured. The results are illustrated in Figure 5-24.

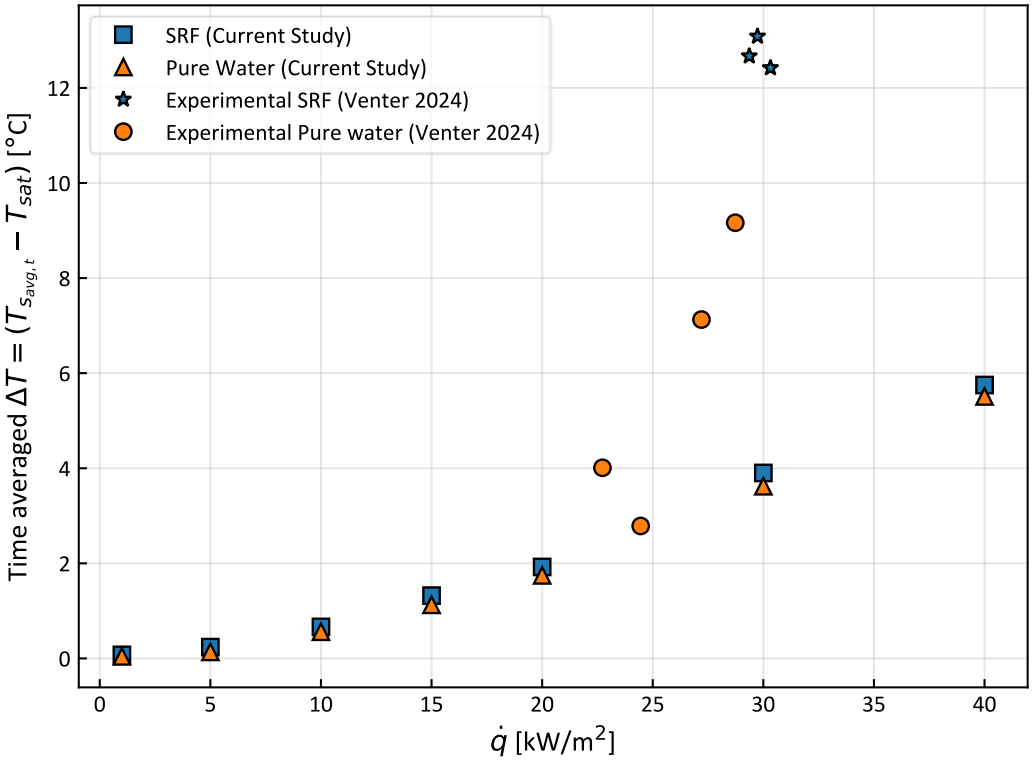

Figure 5-24: Time-averaged temperature difference between the wall temperature and saturation temperature comparing the current numerical results and experimental results by Venter [3] with G = 15 kg/m^{2}s.

From Figure 5-24, it shows that the SRF fluid experienced larger temperature differentials than the water for the experiments as observed in the numerical study. It was also noted that the experimental results were higher than those obtained in the current numerical study everywhere. This difference could be explained by the 2D nature of the numerical study compared to the 3D nature of the experiments, as well as the fact that the numerical study did not consider heat loss the environment. Furthermore, the numerical results were captured over a very short period of up to 20 ms whereas the experimental results were obtained and averaged over a 60 s period.

To understand why the numerical model predicted the above results, it is important to consider the way the VOF method works. The numerical simulations began with a steady-state single-phase simulation from which the fluid temperature and velocity profiles were obtained. This means that as the heat flux was increased, the temperature profile obtained had higher fluid temperatures, and thus higher wall temperatures. In the two-phase simulations, the hot liquid around the vapour bubble was evaporated, causing the bubble to grow. As the bubbles clogged the channel, a thin liquid film formed which contained the original hot fluid from the steady-state simulation. As discussed in 0, the SRF experienced thicker, thin film layers than the water due to its self-rewetting nature drawing the surrounding fluid in. Since the surface tension was the only property that differed between the two fluids, it could be said that the rate of evaporation was the same. Therefore, the only reason that the film thicknesses differed between the two fluids was because of the surface tension gradients influencing the thermocapillary flow. Since the SRF was drawing in the warmer surrounding fluid into the thin liquid film, it experienced larger surface temperatures than the water. By using Eq. (3-28), the higher surface temperatures resulted in lower heat transfer coefficients. This is particularly true at the leading edge of the bubble where the fluid drawn in by the SRF had very high temperatures. Additionally, the bubble growth rate was much greater than the free-stream velocity which meant that new, cooler fluid was not yet contributing to the cooling of the liquid film, and thus the heated surface. With a thicker liquid film, the hotter fluid near the surface remains hot while the fluid near the interface changes phase and cools (to saturation temperature). This also contributed to the higher surface temperatures in the SRF. This observation is confirmed by looking at the film thicknesses and heat transfer coefficient results in Figure 5-18 and Figure 5-23(a) respectively. At 40 kW/m² it showed that both the film thickness and the heat transfer coefficients were the closest between the two fluids. Because the simulations ran for such a short flow period, the hotter fluid near the surface was not transported towards the interface and was not evaporated.

The results indicate that in the absence of surface wettability and contact angles, the SRF does not provide heat transfer benefits over the water. Instead, the two fluids experienced similar surface temperatures, and at high heat fluxes, they experienced similar heat transfer coefficients. Looking back at the investigation by Li et al. [2], it was shown that when surface wettability is a factor, the SRF outperforms the water in terms of heat transfer capabilities. Considering that the current study observed similar fluid dynamics as that by Li et al. [2], the difference in heat transfer results is due to the surface wettability.

It is suggested that more simulations be conducted at higher heat fluxes to observe if a similar trend in the surface temperature and heat transfer coefficients still exist. Furthermore, it is expected that three dimensional (3D) simulations would better model the heat transfer characteristics as the surface tension and gravity forces would be better modelled.

5.6 Chapter Summary

This chapter discussed the results from the numerical investigations conducted in the study. The numerical investigation compared the microchannel flow boiling of pure water and a 5% v/v 1-butanol-water mixture as the self-rewetting fluid (SRF) using a 5 mm long and 0.3 mm high two-dimensional (2D) domain. A total of 14 tests were conducted using a mass flux of 15 kg/m²s and a range of heat fluxes from 1 kW/m² to 40 kW/m². The discussion was divided into two sections which covered the bubble behaviour, and the heat transfer characteristics.

The bubble growth rate, the bubble interfacial velocity, surrounding fluid velocity, and the film thickness was studied in the bubble behaviour section. The simulations started with an initial circular bubble along the centreline of the domain which grew and stretched throughout the domain as the simulation progressed. By recording the bubble lengths throughout the progression of the different cases, the growth rates were obtained. The growth rates were defined by the gradient of an exponential function fit to the progression of the bubble length data. The growth rates for each of the 14 cases were then compared. It was noticed that by increasing the heat flux, the bubble growth rate was also increased. This is explained by the higher heat flux increasing the rate of evaporation. When comparing the two fluids against each other, it was noticed that the water experienced greater bubble growth rates than the SRF for all heat fluxes. By looking at the interfacial velocities of the vapour slugs, the same was observed with the water having larger interfacial velocities than the SRF. This contradicts that observed by Li et al. [2], however their simulations included surface wettability and surface dry out whereas ours did not. It can be said that if only a vapour slug is present within a channel which has a constant liquid film separating it and the heated wall, then the growth rate of water is larger than that of the SRF. This is explained by the surrounding fluid being drawn into the heated region due to the Marangoni effect, restricting the growth of the bubble. This phenomenon was visually illustrated by looking at the surrounding fluid velocity vectors. The self-rewetting nature of the SRF drawing the surrounding fluid into the heated region meant that the SRF had thicker liquid films between the vapour slugs and the heated wall.

The heat transfer coefficient and surface temperatures were investigated to better understand the heat transfer characteristics. As mentioned above, the SRF had thicker liquid films between the vapour slugs and the heat surface than the water. This was because the warm surrounding fluid was being drawn in towards the warmer heated surface and thus resulted in a warmer liquid film than the water. Furthermore, the hotter fluid near the surface did not migrate to the interface and evaporate. This resulted in the heat transfer coefficients of the water being larger than that of the SRF cases. As the heat flux was increased, the surface temperatures increased due to how the simulation was solved. It was noticed that the surface temperatures increased drastically, and that the water experienced lower surface temperatures than the SRF fluid, everywhere. Venter [3] made similar observations in that

the pure water experienced higher heat transfer coefficients than the SRF for various heat fluxes. However, Venter observed that at a higher mass flux of G = 25 kg/m^{2}s, the opposite was true and that the SRF experienced higher heat transfer coefficients than the water.

6 CONCLUSION AND RECOMMENDATIONS

With electronics continually shrinking while concurrently producing higher heat fluxes, more effective cooling methods are required, such as microchannel flow boiling. Microchannel flow boiling uses latent heat to transfer heat from a hot surface to the working fluid through phase change. However, as these heat fluxes continue to increase, it has been observed that normal fluids, such as water, experience the formation of local dry-out regions which drastically reduce the heat transfer rate from the heated surface and causes component failure. A more recently developed fluid with the property of a non-linear surface tension dependency on temperature has emerged as a possibility to delay the formation of dry-out regions. Little to no research has been conducted on the heat transfer capabilities of these fluids in microchannel cooling applications. Of the available research on these fluids, a very small portion consists of numerical investigations. This study had aimed to contribute to this field with useful information on the bubble behaviour and heat transfer capabilities of these fluids in microchannel flow boiling with the use of numerical techniques.

The numerical study investigated the effects of surface tension in a long, thin microchannel using two-dimensional (2D) simulations. The domain was 5 mm long and 0.3 mm high, and the fluids used were pure water and a 5% v/v 1-butanol-water mixture as the self-rewetting fluid (SRF). The simulation made use of the VOF multiphase model with surface tension modelled using the CSF method and the modified Schrage model as the evaporation model. Heat fluxes from 1 kW/m² to 40 kW/m² were used at a mass flux of 15 kg/m²s during the study resulting in 14 simulations in total.

From the simulations it was observed that the water experienced higher bubble growth rates than the SRF. This was observed by looking at both the bubble growth rates and the interfacial velocities. Due to the self-rewetting nature of the SRF, the surrounding fluid was drawn in towards the heated surface as explained by the Marangoni effect. This meant that the growth of the vapour slugs when using SRFs was hindered by the surrounding fluid. A visual illustration of the surrounding fluid velocity vectors showed this drawing in of the fluid. It followed that the SRF experienced thicker liquid film layers between the vapour slug and the heated surface. These results illustrate the expected flow behaviour of SRFs which promise to increase heat transfer capabilities.

However, when comparing the difference in surface temperature and saturation temperature, and the heat transfer coefficients, it was found that the water outperformed the SRF. This was unexpected, especially after observing the bubble dynamics results. Because of how the simulations are solved and how they progressed, it was explained that the thicker film layer meant that more fluid was present causing the higher surface temperatures. The thicker liquid film meant that the hotter fluid near the surface remained hot while the fluid near the interface changed phase and cooled. This caused higher surface temperatures, and thus larger temperature differences, with the SRF than with the water. Unfortunately, because the simulations run for such a short flow period, the fluid nearest to the surface does not get transported towards the two-phase interface. This means that the ‘’cooling’’ effect of incoming fluid does not get represented well.

In summary, the numerical simulations over various heat fluxes observed that:

- The self-rewetting effect was present in the 5% v/v 1-butanol-water fluid by considering the fluid velocity vectors and the thin liquid film layer separating the vapour slug from the heated surface.
- The self-rewetting effect however did not predict lower surface temperatures and higher heat transfer coefficients.

A similar study by Li et al. [2] showed that the presence of surface wettability and contact angles resulted in almost completely different results. The observations made that were similar to the current study was the fluid velocity around the interface due to the Marangoni effect. This suggests that the self-rewetting fluid outperforms the water when there is contact between the heated surface and the bubble interface but does not provide many benefits when this is not the case.

Furthermore, a similar experimental study by Venter [3], who also investigated a 5% v/v 1-butanol-water mixture in horizontal mirochannels, observed similar heat transfer results to those obtained in this study. From Venter's [3] heat transfer coefficient results, it was observed that the pure water outperformed the 5% v/v 1-butanol-water mixture when a mass flux of G = 15 kg/m^{2}s was used. However, for a larger mass flux of G = 25 kg/m^{2}s, the opposite was observed, and the 5% v/v 1-butanol-water mixture outperformed the water.

Some recommendations for future studies are described below:

- Numerical investigations using higher heat fluxes should be conducted to investigate whether the surface temperature and heat transfer trends change between the two fluids, such as observed by Venter [3].
- Three-dimensional (3D) simulations should be conducted to better model the effects of surface tension and gravity. This should provide valuable information into the heat transfer characteristics of self-rewetting fluids.

7 REFERENCES

[1] Z. Zhang, X. Wang and Y. Yan, "A review of the state-of-the-art in electronic cooling," *e-Prime - Advances in Electrical Engineering, Electronics and Energy,* vol. 1, 2021.

[2] W. Li, Y. Lin and Y. Luo, "Numerical Investigation on Bubble Growth and Merger in Microchannel Flow Boiling With Self-Rewetting Fluid," *Journal of Heat Transfer,* vol. 143, 2021.

[3] M. Venter, "Experimental Investigation of Surface Tension and Inclination Effects for Flow Boiling in a Rectangular Micro/Mini-channel with Self-rewetting Mixtures.," 2024.

[4] A. Cebi, A. Celen, A. H. Donmez, Y. Karakoyun, P. Celen, M. S. Cellek, A. S. Dalkilic, T. Taner and S. Wongwises, "A review of flow boiling in mini and microchannel for enhanced geometries," *Journal of Thermal Engineering,* vol. 4, pp. 2037-2074, 2018.

[5] S. S. Mehendale, A. M. Jacobi and R. K. Shah, "Fluid Flow and Heat Transfer at Micro- and Meso-Scales with Applications to Heat Exchanger Design," *Applied Mechanics Review,* vol. 53, pp. 175-193, 2000.

[6] S. G. Kandlikar, "Fundamental issues related to flow boiling in minichannels and microchannels," *Experimental Thermal and Fluid Science,* vol. 26, no. 2, pp. 389-407, 2002.

[7] T. G. Karayiannis and M. M. Mahmoud, "Flow boiling in microchannels: Fundamentals and applications," *Applied Thermal Engineering,* vol. 115, pp. 1372-1397, 2017.

[8] K. A. Triplett, S. M. Ghiaasiaan, S. I. Abdel-Khalik and D. L. Sadowski, "Gas-liquid two-phase flow in microchannels Part 1: two-phase flow patterns," *International Journal of Multiphase Flow,* vol. 25, pp. 377-394, 1999.

[9] P. A. Kew and K. Cornwell, "Correlations for the prediction of boiling heat transfer in small-diameter channels," *Applied Thermal Engineering,* vol. 17, pp. 705-715, 1997.

[10] C. L. Ong and J. R. Thome, "Macro-to-microchannel transition in two-phase flow: Part 1 – Two-phase flow patterns and film thickness measurements," *Experimental Thermal and Fluid Science,* vol. 35, pp. 37-47, 2010.

[11] N. Brauner and D. Moalem-Maron, "Identification of the range of 'small diameters' conduits, regarding two-phase flow pattern transition," *Int. Comm. Heat Mass Transfer,* vol. 19, pp. 29-39, 1992.

[12] T. Harirchian and S. V. Garimella, "A comprehensive flow regime map for microchannel flow boiling with quantitative transition criteria," *International Journal of Heat and Mass Transfer,* vol. 53, pp. 2694-2702, 2010.

[13] Y. A. Cengel and A. J. Ghajar, Heat and Mass Transfer: Fundamentals and Applications, Sixth Edition ed., New York: McGraw-Hill Education, 2020.

[14] L. Cheng and G. Xia, "Fundamental issues, mechanisms and models of flow boiling heat transfer in microscale channels," *International Journal of Heat and Mass Transfer,* vol. 108, pp. 97-127, 2017.

[15] S. Halon, Z. Krolicki, R. Revellin and B. Zajaczkowski, "Local flow patterns distribution during flow boiling in micro channel array," *Experimental Thermal and Fluid Science,* vol. 141, 2023.

[16] A. Bordbar, A. Taassob, A. Zarnaghsh and R. Kamali, "Slug flow in microchannels: Numerical simulation and applications," *Journal of Industrial and Engineering Chemistry,* vol. 62, pp. 26-39, 2018.

[17] L. Chen, Y. S. Tian and T. G. Karayiannis, "The effect of tube diameter on vertical two-phase flow regimes in small tubes," *International Journal of Heat and Mass Transfer,* vol. 49, pp. 4220-4230, 2006.

[18] Z. Guo, D. F. Fletcher and B. S. Haynes, "Numerical simulation of annular flow hydrodynamics in microchannels," *Computers and Fluids,* vol. 133, pp. 90-102, 2016.

[19] R. Revellin and J. R. Thome, "Experimental investigation of R-134a and R-245fa two-phase flow in microchannels for different flow conditions," *International Journal of Heat and Fluid Flow,* vol. 28, pp. 63-71, 2007.

[20] R. Charnay, R. Revellin and J. Bonjour, "Flow boiling heat transfer in minichannels at high saturation temperatures: Part 1 - Experimental investigation and analysis of the heat transfer mechanisms," *International Journal of Heat and Mass Transfer,* vol. 87, pp. 636-652, 2015.

[21] R. Charnay, J. Bonjour and R. Revellin, "Experimental investigation of R-245fa flow boiling in minichannels at high saturation temperatures: Flow patterns and flow pattern maps," *International Journal of Heat and Fluid Flow,* vol. 46, pp. 1-16, 2014.

[22] R. Charnay, R. Revellin and J. Bonjour, "Flow pattern characterization for R-245fa in minichannels: Optical measurement technique and experimental results," *International Journal of Multiphase Flow,* vol. 57, pp. 169-181, 2013.

[23] Y. Kubo, S. Yamada, H. Murakawa and H. Asano, "Pressure drop and flow patterns of boiling flow in Mini-Channels with Semi-Circular Cross-Section," *Applied Thermal Engineering,* vol. 194, 2021.

[24] Z.-Q. Yang, G.-F. Chen, X.-R. Zhuang, Q.-L. Song, Z. Deng, J. Shen and M.-Q. Gong, "A new flow pattern map for flow boiling of R1234ze(E) in horizontal tube," *International Journal of Multiphase Flow,* vol. 98, pp. 24-35, 2018.

[25] C. Keepaiboon and S. Wongwises, "Two-phase flow patterns and heat transfer characteristics of R134a refrigeratn during flow boiling in a single rectangular micro-channel," *Experimental Thermal and Fluid Science ,* vol. 66, pp. 36-45, 2015.

[26] Y. K. Prajapati and P. Bhandari, "Flow boiling instabilities in microchannels and their promising solutions – A review," *Experimental Thermal and Fluid Science,* vol. 88, pp. 576-593, 2017.

[27] H. J. Lee, D. Y. Liu and S.-c. Yao, "Flow instability of evaporative micro-channels," *International Journal of Heat and Mass Transfer,* vol. 53, pp. 1740-1749, 2010.

[28] W. Qu and I. Mudawar, "Measurement and prediction of pressure drop in two-phase micro-channel heat sinks," *International Journal of Heat and Mass Transfer,* vol. 46, pp. 2737-2753, 2003.

[29] Y. W. Kuang, W. Wang, J. Y. Miao, X. G. Yu, H. X. Zhang and R. Zhaun, "Flow boiling of ammonia and flow instabilities in mini-channels," *Applied Thermal Engineering,* vol. 113, pp. 831-842, 2017.

[30] A. Megahed, "Experimental investigation of flow boiling characteristics in a corss-linked microchannel heat sink," *International Journal of Multiphase Flow ,* vol. 37, pp. 380-393, 2011.

[31] T. Alam, P. S. Lee and C. R. Yap, "Effects of surface roughness on flow boiling in silicon microgap heat sinks," *International Journal of Heat and Mass Transfer,* vol. 64, pp. 28-41, 2013.

[32] M. M. Mahmoud, T. G. Karayiannis and D. B. R. Kenning, "Surface effects in flow boiling of R134a in microtubes," *International Journal of Heat and Mass Transfer,* vol. 54, p. 3334–3346, 2011.

[33] T. Y. Liu, P. L. Li, C. W. Liu and C. Gau, "Boiling flow characteristics in microchannels with very hydrophobic surface to super-hydrophilic surface," *International Journal of Heat and Mass Transfer,* vol. 54, pp. 126-134, 2011.

[34] C. Choi, J. S. Shin, D. I. Yu and M. H. Kim, "Flow boiling behaviors in hydrophilic and hydrophobic microchannels," *Experimental Thermal and Fluid Science ,* vol. 35, pp. 816-824, 2011.

[35] S.-C. Wu, "Study of self-rewetting fluid applied to loop heat pipe," *International Journal of Thermal Sciences,* vol. 98, pp. 374-380, 2015.

[36] A. Sitar and I. Golobic, "Heat transfer enhancement of self-rewetting aqueous n-butanol solutions boiling in microchannels," *International Journal of Heat and Mass Transfer,* vol. 81, pp. 198-206, 2015.

[37] K. Hosseinzadeh, M. A. E. Moghaddam, M. Hatami, D. D. Ganji and F. Ommi, "Experimental and numerical study for the effect of aqueous solution on heat transfer characteristics of two phase close thermosyphon," *International Communications in Heat and Mass Transfer,* vol. 135, pp. 106-129, 2022.

[38] A. Sitar, M. Zupancic, M. Crivellari and I. Golobic, "The onset of nucleate boiling of self-rewetting fluids in microchannels," *IOP Conference Series: Earth and Environmental Science,* vol. 93, 2017.

[39] Z. Guo, D. F. Fletcher and B. S. Haynes, "Implementation of a height function method to alleviate spurious currents in CFD modelling of annular flow in microchannels," *Applied Mathematical Modelling,* vol. 39, pp. 4665-4686, 2015.

[40] C. W. Hirt and B. D. Nichols, "Volume of Fluid (VOF) Method for the Dynamics of Free Boundaries," *Journal of Computational Physics,* vol. 39, pp. 201-225, 1981.

[41] Q. Liu, W. Wang and B. Palm, "Numerical study of the interactions and merge of multiple bubbles during convective boiling in micro channels," *International Communications in Heat and Mass Transfer,* vol. 80, pp. 10-17, 2017.

[42] M. Sussman and E. G. Puckett, "A Coupled Level Set and Volume-of-Fluid Method for Computing 3D and Axisymmetrix Incompressible Two-Phase Flows," *Journal of Computational Physics,* vol. 162, pp. 301-337, 2000.

[43] D. L. Sun and W. Q. Tao, "A coupled volume-of-fluid and level set (VOSET) method for computing," *International Journal of Heat and Mass Transfer,* vol. 53, pp. 645-655, 2010.

[44] K. Ling, S. Zhang, P.-Z. Wu, S.-Y. Yang and W.-Q. Tao, "A coupled volume-of-fluid and level-set method (VOSET) for capturing interface of two-phase flows in arbitrary polygon grid," *International Journal of Heat and Mass Transfer,* vol. 143, 2019.

[45] K. Ling, G. Son, D.-L. Sun and W.-Q. Tao, "Three dimensional numerical simulation on bubble growth and merger in microchannel boiling flow," *International Journal of Thermal Sciences,* vol. 98, pp. 135-147, 2015.

[46] S. Hardt and F. Wondra, "Evaporation model for interfacial flows based on a continuum-field representation of source terms," *Journal of Computational Physics,* vol. 227, pp. 5871-5895, 2008.

[47] J. Potgieter, "Numerical investigation on the effect of gravitational orientation on bubble growth during flow boiling in a high aspect ratio microchannel," 2019.

[48] C. R. Kharangate and I. Mudawar, "Review of computational studies on boiling and condensation," *International Journal of Heat and Mass Transfer,* vol. 108, pp. 1164-1196, 2017.

[49] C. Kunkelmann, "Numerical Modeling and Investigation of Boiling Phenomena," Technische Universität Darmstadt, Darmstadt, 2011.

[50] I. Tanasawa, "Advances in Condensation Heat Transfer," *Advances in Heat Transfer,* vol. 21, pp. 55-133, 1991.

[51] ANSYS Inc., "Ansys Fluent User's Guide, 2023R1," 2023. [Online]. Available: https://ansyshelp.ansys.com/account/secured?returnurl=/Views/Secured/corp/v231/en/flu_ug/flu_ug_GridQuality.html. [Accessed 2023].

[52] R. Courant, K. Friedrichs and H. Lewy, "On the Partial Difference Equations of Mathematical Physics," *IBM Journal of Research and Development,* vol. 11, no. 2, pp. 215-234, 1967.

[53] M. Magnini, B. Pulvirenti and J. R. Thome, "Numerical investigation of the influence of leading and sequential," *International Journal of Thermal Sciences,* vol. 71, pp. 36-52, 2013.

[54] A. Ferrari, M. Magnini and J. R. Thome, "Numerical analysis of slug flow boiling in square microchannels," *International Journal of Heat and Mass Transfer,* vol. 123, p. 928–944, 2018.

[55] A. J. J. Straathof, A. Oudshoorn and L. A. M. van der Wielen, "Assessment of Options for Selective 1-Butanol Recovery from Aqueous Solution," *Industrial and Engineering Chemistry Research,* vol. 48, pp. 7325-7336, 2009.

[56] A. Mukherjee, S. G. Kandlikar and Z. J. Edel, "Numerical study of bubble growth and wall heat transfer during flow boiling," *International Journal of Heat and Mass Transfer,* vol. 54, pp. 3702-3718, 2011.

[57] S. K. Saha, G. Katiyar, S. Karagadde and A. Sharma, "Numerical modelling of bubble growth in microchannel using Level Set," *International Journal of Heat and Mass Transfer,* vol. 101, pp. 719-732, 2016.

[58] W. Li, J. Zhang and D. F. Fletcher, "Heat transfer and pressure drop characteristics of gas–liquid Taylor flow," *International Journal of Heat and Mass Transfer,* vol. 103, pp. 45-56, 2016.

[59] R. W. Schrage, A Theoretical Study of Interphase Mass Transfer, New York Chichester, West Sussex: Columbia Univertsity Press, 1953.

APPENDIX A – USER DEFINED FUNCTION (UDF)

The code below was used as the User Defined Function (UDF) to implement the modified Schrage evaporation model by Hardt and Wondra [46]. This code was developed by Potgieter [47] and includes the implementation of the adaptive mesh refinement.

```
/*(Hardt and Wondra, 2008) Evaporation Model.*/

#include "udf.h"
#include "prf.h"
#define domain_ID 2

static real NV=0.0; /*Vapour Normalisation Factor*/
static real NL=0.0;/*Liquid Normalisation Factor*/
static real mass_v=0;/*Vapour Creation per Cell*/
static real mass_l=0;/*Liquid Disappearance per Cell*/
static real enrg_s=0.0;/* Energy Change per Cell*/
static real T_SAT = 373.2;/*Saturation Temperature*/
static real ac= 1; /*Accomodation Coefficient*/
static real mgVOF=0.0; /*Magnitude of VOF Gradient*/
static real M=18.0152; /*Molecular Mass*/
static real h=2256052.8; /*Latent Heat*/
static real R=8314.0; /*Gas Constant*/
static real pi =3.1415259;/*pi*/
static real m_lg = 0.0;/*Mass Flux*/
static real m_nt=0.0;/*Temporal Gradient of Mass Flux*/
static real m_gr=0.0;/*Source term for Mesh Adaption*/
static real Ntop=0.0;/*Normalisation factor*/
static real Nbot=0.0;/*Normalisation factor denominator*/
static real Ntot=0.0;/*Normalisation factor numerator*/
static real RhoG=0.601038;/*Vapour Density*/
static real RhoL=958.249;/*Liquid Density*/
static real NVbot=0.0;/*Denomenator for Equation 17*/
static real NVLtop=0.0;/*Numerator for Equation 17 and Equation 18*/
static real NLbot=0.0;/*Denomenator for Equation 18*/
static real VCutV=1e-3;/*Vapour volume cut-off*/
static real VCutL=1e-1;/*Liquid volume cut-off*/
static real cpl=4215.835; /*Liquid Specific Heat*/
static real cpg=2080.596;/*Vapour Specific Heat*/

/*Scalars
uds-scalar-0: Volume Fraction
uds-scalar-1: Initial Mass Source Term Used for Smearing
uds-scalar-2: Smeared Mass Source Term
uds-scalar-3: Initial Mesh Source Term Used for Smearing
uds-scalar-4: Smeared Mesh Source Term
uds-scalar-5: Smeared and Bounded Mass Source Term
uds-scalar-6: Vapour Source Term
uds-scalar-7: Liquid Source Term
uds-scalar-8: Energy Source Term
uds-scalar-9: Gradient of Initial Source Term
*/

/*The purpose of the adjust_gradient function is to assign the volume fraction to a scalar quantity. Ansys Fluent does not automatically calculate the gradient of the volume fraction, but it does calculate it for scalar quantities, so this function forces Ansys Fluent to calculate the gradient of the volume fraction.*/
DEFINE_ADJUST(adjust_gradient, domain)
{
      Thread *t;
      cell_t c;
      face_t f;
      domain = Get_Domain(domain_ID);

      /* Fill UDS with the variable. */
      thread_loop_c (t,domain)
      {
```

```
59.                 if (THREAD_STORAGE(t,SV_UDS_I(0))!=NULL)
60.                         begin_c_loop (c,t)
61.                         {
62.                                 C_UDSI(c,t,0) = (C_VOF(c,t));
63.                         }
64.                         end_c_loop (c,t)
65.       }
66.
67.
68.       thread_loop_f (t,domain)
69.       {
70.                 if (THREAD_STORAGE(t,SV_UDS_I(0))!=NULL)
71.                         begin_f_loop (f,t)
72.                         {
73.                                 F_UDSI(f,t,0) = (F_VOF(f,t));
74.                         }
75.                         end_f_loop (f,t)
76.       }
77. }
78.
79. /*The in_s_term function calculates the initial source term that will later be smeared. First,
Ntot, which ensures that the total interfacial area remains constant once the scalar field is
skewed to the liquid side, is calculated. Next, the initial source term, as well as its gradient,
which is used to calculate the gradient of the energy source term, is calculated. Finally, the
mass flux is multiplied by the interfacial area and the normalisation factor to create the initial
source term. */
80. DEFINE_ADJUST(in_s_term, domain)
81. {
82.       Thread *t;
83.       cell_t c;
84.       m_lg=0;
85.       m_gr=0;
86.       Ntot=0;
87.       domain = Get_Domain(domain_ID);
88.
89.
90.       /* Calculate integrals and normalisation factor as N*/
91.       thread_loop_c(t,domain)
92.       {
93.
94.                 begin_c_loop(c,t)
95.                 {
96.                         Ntop += NV_MAG(C_UDSI_G(c,t,0))*C_VOLUME(c,t);
97.
98.                         if (C_VOF(c,t)<0.99 && C_VOF(c,t)>0.01)
99.                                 Nbot                                                    +=
C_UDSI(c,t,0)*NV_MAG(C_UDSI_G(c,t,0))*C_VOLUME(c,t);
100.                }
101.                end_c_loop(c,t)
102.      }
103.
104.      if (PRF_GRSUM1(Nbot)!=0)
105.      {
106.                Ntot=PRF_GRSUM1(Ntop)/PRF_GRSUM1(Nbot);
107.      }
108.
109.
110.      /* Calculate mass flux. */
111.      thread_loop_c (t,domain)
112.      {
113.                begin_c_loop (c,t)
114.                {
115.                        mgVOF = NV_MAG(C_UDSI_G(c,t,0));
116.                        if (mgVOF>=1 && C_VOF(c,t)<0.99 && C_VOF(c,t)>0.01)
117.                        {
118.                                m_lg   =  (2*ac/(2-ac))*sqrt(M/(2*pi*R))*RhoG*h*(C_T(c,t)-
T_SAT)/pow(T_SAT, 1.5);
119.                                m_gr=(2*ac/(2-ac))*sqrt(M/(2*pi*R))*RhoG*h/pow(T_SAT,
1.5);
120.                        }
```

```
121.
122.                         else
123.                         {
124.                                 m_lg=0;
125.                                 m_gr=0;
126.                         }
127.
128.                         if (mgVOF>=1)
129.                         {
130.                                 m_nt=(2*ac/(2-ac))*sqrt(M/(2*pi*R))*RhoG*h/pow(T_SAT,
1.5);
131.                         }
132.
133.                         else
134.                         {
135.                                 m_nt=0;
136.                         }
137.
138.                         C_UDSI(c,t,3)=m_nt*mgVOF;
139.                         C_UDSI(c,t,1)=Ntot*C_VOF(c,t)*m_lg*mgVOF;/* Initial Source term P0*/
140.                         C_UDSI(c,t,9)=Ntot*C_VOF(c,t)*m_gr*mgVOF;
141.                 }
142.                 end_c_loop (c,t)
143.         }
144. }
145.
146.
147. /*The mass_source and mesh_refine functions are unsteady terms that are used to smear the
source terms over a constant distance regardless of the size of the time step. */
148. DEFINE_UDS_UNSTEADY(mass_source,c,t,i,apu,su)
149. {
150.         real physical_dt, vol, rho, phi_old;
151.         physical_dt = 4e-9;
152.         vol = C_VOLUME(c,t);
153.         rho = C_R(c,t);
154.         *apu = -rho*vol / physical_dt;/*implicit part*/
155.         phi_old = C_UDSI(c,t,1);
156.         *su = rho*vol*phi_old/physical_dt;/*explicit part*/
157. }
158.
159. DEFINE_UDS_UNSTEADY(mesh_refine,c,t,i,apu,su)
160. {
161.         real physical_dt, vol, rho, phi_old;
162.         physical_dt = 4e-9;
163.         vol = C_VOLUME(c,t);
164.         rho = C_R(c,t);
165.         *apu = -rho*vol / physical_dt;/*implicit part*/
166.         phi_old = C_UDSI(c,t,3);
167.         *su = rho*vol*phi_old/physical_dt;/*explicit part*/
168. }
169.
170. /*The diffuse function takes the mass source term, which has been smeared by the Ansys Fluent
solver, and bounds it so that mass transfer will only occur within refined cells */
171. DEFINE_ADJUST(diffuse, domain)
172. {
173.         Thread *t;
174.         cell_t c;
175.         domain = Get_Domain(domain_ID);
176.
177.         /* Fill UDS with the variable. */
178.         thread_loop_c (t,domain)
179.         {
180.                 begin_c_loop (c,t)
181.                 {
182.                         if (C_UDSI(c,t,4)>=1e5)
183.                         {
184.                                 C_UDSI(c,t,5) = C_UDSI_M1(c,t,2);
185.                         }
186.
187.                         if (C_UDSI(c,t,4)<1e5 || C_UDSI_M1(c,t,2)<0)
```

```
                        {
                                C_UDSI(c,t,5) = 0;
                        }
                }
                end_c_loop (c,t)
        }
}

/* The norm_fct function creates normalisation factors by integrating the initial source term, and then integrating the bounded and smeared source terms to ensure the conservation of total mass transfer*/
DEFINE_ADJUST(norm_fct, domain)
{
        Thread *t;
        cell_t c;
        NVbot=0.0;
        NVLtop=0.0;
        NLbot=0.0;
        NL=0.0;
        NV=0.0;
        domain = Get_Domain(domain_ID);
        thread_loop_c (t,domain)
        {
                begin_c_loop (c,t)
                {
                        NVLtop += C_UDSI(c,t,1)*C_VOLUME(c,t);
                        if (C_VOF(c,t) <= VCutV)
                        {
                                NVbot += (1-C_VOF(c,t))*C_UDSI(c,t,5)*C_VOLUME(c,t);
                        }

                        if (C_VOF(c,t) >= (VCutL))
                        {
                                NLbot += C_VOF(c,t)*C_UDSI(c,t,5)*C_VOLUME(c,t);
                        }
                }
                end_c_loop (c,t)
        }

        if (PRF_GRSUM1(NVbot) !=0 && PRF_GRSUM1(NLbot) !=0)
        {
                NV=PRF_GRSUM1(NVLtop)/PRF_GRSUM1(NVbot);
                NL=PRF_GRSUM1(NVLtop)/PRF_GRSUM1(NLbot);
        }
}

/*The vap_src function uses the smeared and bounded source terms and the normalisation factor to explicitly create a source term for the vapour domain*/
DEFINE_SOURCE(vap_src,c,sec_th,dS,eqn)
{
        mass_v=0;
        Thread *mix_th, *pri_th;
        mix_th = THREAD_SUPER_THREAD(sec_th);
        pri_th = THREAD_SUB_THREAD(mix_th,0);
        if (C_VOF(c,pri_th)<=VCutV)
        {
                mass_v = NV*(1-C_VOF(c,pri_th))*C_UDSI(c,mix_th,5);/*explicit part*/
                dS[eqn] = 0;/*implicit part*/
        }

        else if (C_VOF(c,pri_th)>VCutV)
        {
                mass_v = 0;/*explicit part*/
                dS[eqn] = 0;/*implicit part*/
        }
        C_UDSI(c,mix_th,6)=mass_v;
        return mass_v;
}
```

```
/*The liq_src function uses the smeared and bounded source terms and the normalisation factor to explicitly create a source term for the liquid domain*/


DEFINE_SOURCE(liq_src,c,pri_th,dS,eqn)
{
      mass_l=0;
      Thread *mix_th, *sec_th;
      mix_th = THREAD_SUPER_THREAD(pri_th);
      if (C_VOF(c,pri_th)>=(VCutL))
      {
                mass_l = -NL*C_VOF(c,pri_th)*C_UDSI(c,mix_th,5);/*explicit part*/
                dS[eqn] = 0.0;/*implicit part*/
      }

      else if (C_VOF(c,pri_th)<(VCutL))
      {
                mass_l = 0;/*explicit part*/
                dS[eqn] = 0;/*implicit part*/
      }
      C_UDSI(c,mix_th,7)=mass_l;
      return mass_l;
}


/*The enrg_src funtction uses the initial source term, its gradient and the liquid and vapour source terms,
multiplied by their specific heats to implicitly create a source term for the mixture domain*/


DEFINE_SOURCE(enrg_src,c,t,dS,eqn)
{
      real enrg_s=0;
      enrg_s                  =                  -C_UDSI(c,t,1)*h+C_UDSI(c,t,7)*cpl*(C_T(c,t)-298.15)+C_UDSI(c,t,6)*cpg*(C_T(c,t)-298.15);/*explicit part*/
      dS[eqn] = -C_UDSI(c,t,9)*h+C_UDSI(c,t,7)*cpl+C_UDSI(c,t,6)*cpg;/*implicit part*/
      C_UDSI(c,t,8)=enrg_s;
      return enrg_s;
}

```

APPENDIX B – OBSERVATIONS MADE IN FAILED SIMULATIONS

1. EXAMPLE OF SIMULATION DIVERGENCE CAUSED BY TIME STEPS BEING TOO LARGE

The figure below illustrates the leading edge of the vapour slug when the time-step size was selected too large. The bubble progressed too rapidly for the adaptive mesh refinement, leaving the refined cells behind the interface and courser cells ahead of, and on-top of, it. With the interface running along the courser cells, a volatile pattern emerges with an eventual break-down of the interface. Once the bubble interface breaks down, the energy equation diverges resulting in significantly large fluid temperatures and velocities, leading to ANSYS Fluent errors.

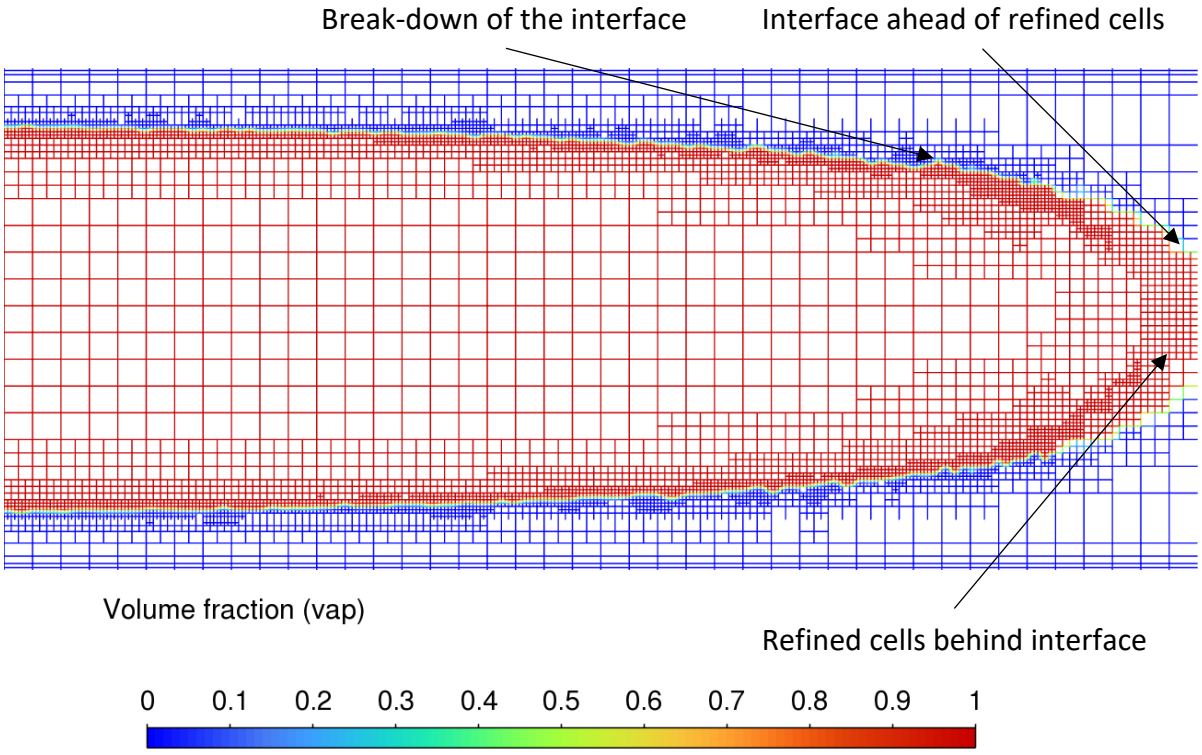

2. PLACING A VAPOUR BUBBLE IN A REGION BELOW SATURATION

As briefly mentioned in Section 4, placing the initial bubble in a region of saturated liquid is crucial to its development in such a low velocity domain. The Volume of Fluid (VOF) method requires that the surrounding fluid be above saturation to ensure mass transfer from the liquid phase to the vapour phase. In the current domain with a fluid velocity of 0.034 m/s, or mass flux of 15 kg/m^{2}s, and a time-step size of 2E-7s, the observed bubble motion is almost entirely attributed to its growth. It thus follows that if the growth is not modelled, the bubble is expected to remain virtually stationary.

Simulations were performed with various bubble starting shapes ranging from low, thin slugs to large circular bubbles. When patched into regions of saturated liquid, all bubbles expanded into a long slug clogging the channel. When the bubbles were patched into a region below saturation, the surface tension forces shrunk the vapour slugs into circular bubbles without

any expansion. An example of a long, thin vapour slug patched into a region below saturation is illustrated below.

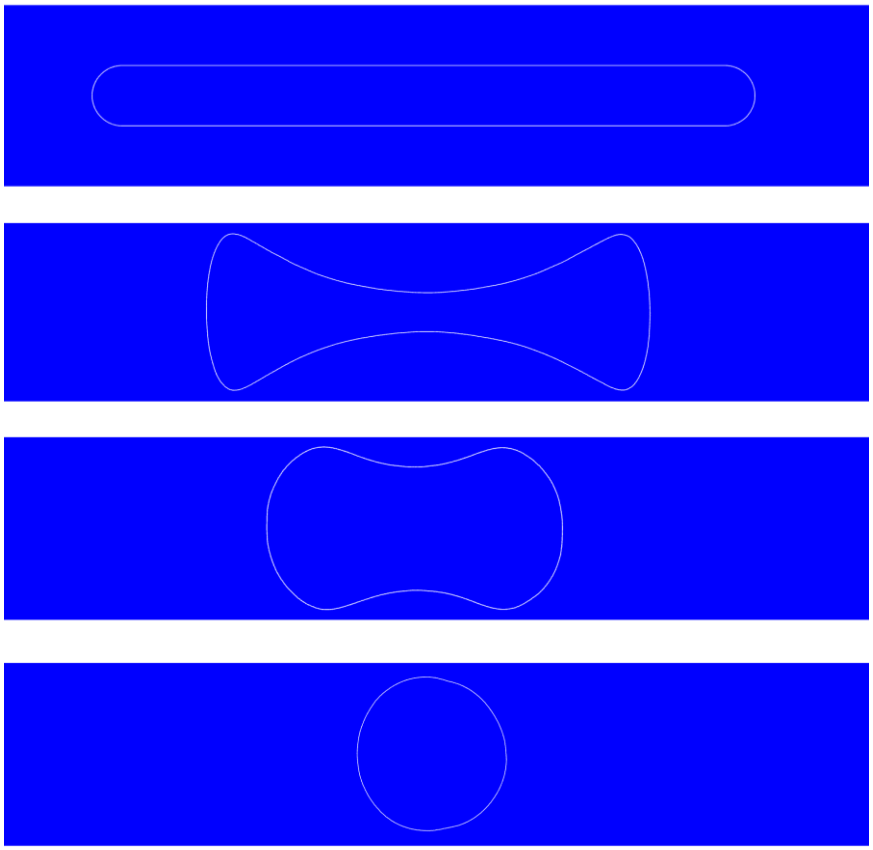

Once the circular shape was developed (t = 2.4 ms), the bubble remained mostly stationary for the remainder of the simulation with no expansion.

APPENDIX C – EXAMPLE OF ANSYS FLUENT JOURNAL SCRIPTS

With over 160 simulations performed, two ANSYS Fluent journal scripts were developed in Notepad++ which could be read to setup all the boundary conditions and fluid properties, as well as initialize the domain and perform the simulations.

The First journal script acted as an initial setup script which implemented all the fluid properties, boundary conditions, and necessary equations, as well as performed the single-phase, steady-state simulation. Once the steady-state simulation was run, this journal script setup the transient simulation and performed the tedious task of patching in the bubble and initializing the three mesh refinement levels. Lastly, this journal script created the bubble animation tracker and then exported the ANSYS case and data files to be solved.

The second journal script was developed such that the already setup and initialized domain could be issued to a high-performance computing center, like the CHPC in Cape Town, and the simulation be performed. This also allowed for a inspection step which allowed for the verification of the domain to be simulated. The second journal script performed the final initializing steps for the transient study such as turning the equations on one by as described in Section 3.3. Thereafter, the script specified the time-stepping information and performed the transient simulation.

The sub-sections below illustrate an example of the journal scripts used in this study for Case 5 in Section 5, which was pure water with a mass flux of 15 kg/m^{2}s and a heat flux of 20 kW/m^2.

1. SIMULATION SETUP JOURNAL SCRIPT (CASE 5 IN SECTION 5)

```
; This is the setup file for the fluent model to obtain the case and data files

; First we setup the general settings i.e.. steady or transient, planar or axisymmetric
define/models steady y
define/operating-conditions gravity y 0 -9.81
define/models/viscous laminar y
define/models energy y n n n y

; Create the material(s)
define/materials/change-create air water-liq y constant 958.249 y constant 4215.835 y constant 0.677263 y constant 0.281169e-03 y 18.0152 n n y
define/materials/change-create water-liq water-vap y constant 0.601038 y constant 2080.596 y constant 0.024584 y constant 0.0122373e-03 n n n n
define/materials/data-base data-type granta-mds
define/materials/copy solid glass-borosilicate
define/materials/data-base data-type fluent-database

; Set the fluid cell-zone, as well as the Boundary conditions
define/boundary-conditions/fluid fluid y water-liq n n n n 0 n 0 n n n
define/boundary-conditions/modify-zones/zone-type inlet mass-flow-inlet
define/boundary-conditions/mass-flow-inlet inlet y n y n 15 n 373.2 n 0 n y
define/boundary-conditions/wall top_heat 0 n 0 y glass-borosilicate n n 0 n n n 1
define/boundary-conditions/wall bot_heat 0.0003 n 0 y glass-borosilicate y heat-flux n 20000 n n n 1
define/materials/delete aluminum

; Set up the solution methods
solve/set/p-v-coupling 24
solve/set/gradient-scheme n y
solve/set/discretization-scheme pressure 14 mom 1 temperature 1
```

```
28.
29. ; Set convergence criteria, hybrid initialize, and run 300 iterations
30. solve/monitors/residual/convergence-criteria 1e-04 1e-04 1e-04 1e-06
31. solve/initialize hyb-initialization
32. solve iterate 300
33.
34. ; Set up VOF model - First we change to transient and then apply vof model, make sure energy
is correct! (no viscous energy dissipation)
35. define/models unsteady-1st-order y
36. define/models/multiphase/model "vof"
37. define/models/multiphase/volume-fraction-parameters formulation implicit volume-fraction-
cutoff 1e-06
38. define/models/multiphase/body-force-formulation y
39. define/models/multiphase/interface-modeling-options 0 y 0.75
40. define/models energy y n n n y
41.
42. ; Add the additional material properties for multiphase calcs
43. define/materials/change-create water-liq water-liq n n n n n y 7562001.992 y 373.2 n n
44. define/materials/change-create water-vap water-vap n n n n n y 48205244.4 y 373.2 n n
45.
46. ; Assign the correct fluids to the correct phases and apply phase interactions
47. define/phases/set-domain-properties/change-phase-names? vap liq
48. define/phases/set-domain-properties/phase-domains liq material y water-liq q vap material y
water-vap
49. define/phases/set-domain-properties/interaction-domain/forces/surface-tension sfc-tension-
coeff y polynomial 3 0.0963688379 -0.0000073453 -0.0000002491 sfc-modeling y wall-adhesion y
50.
51. ; Ensure inlet BC allows only liq entry
52. define/boundary-conditions/mass-flow-inlet inlet mixture y n 373.2 n 0 n y
53. define/boundary-conditions/mass-flow-inlet inlet liq n y n 15
54. define/boundary-conditions/mass-flow-inlet inlet vap n y n 0
55.
56. ; Correct Solution method
57. solve/set/p-v-coupling 22
58. solve/set/gradient-scheme n y
59. solve/set/discretization-scheme pressure 14 mom 1 mp 28 temperature 1
60. solve/monitors/residual/convergence-criteria 1e-04 1e-04 1e-04 1e-06 1e-04
61.
62. ; Create the cell reigsters for the bubble
63. solve/cell-registers/add bubble_left type sphere inside? y center 0.001 0.00015 radius 0.00005
q q
64.
65. ; Patch in the bubble
66. solve/patch vap () bubble_left () mp 1
67.
68. ; Create the vof, temp, vel contours
69. display/objects/create contour vof field vap vof node-values? n surfaces-list interior-fluid
mid_horiz inflation () q
70. display/objects/create contour temp field mixture total-temperature node-values? n q
71. display/objects/create contour vel field mixture velocity-magnitude node-values? n q
72.
73. ; Create refine and coaresen field variables for the interface refinement
74. solve/cell-registers/add refine type field-value field vap vof option more-than 0.01
derivative gradient q q
75. solve/cell-registers/add coarsen type field-value field vap vof option less-than 0.01
derivative gradient q q
76.
77. ; Perform mesh refinement
78. mesh/adapt/set maximum-refinement-level 4
79. mesh/adapt/set maximum-refinement-level 3
80. mesh/adapt/manual-refinement-criteria "refine" manual-coarsening-criteria "coarsen" adapt-
mesh
81.
82. solve/patch vap fluid () () mp 0
83. solve/patch vap () bubble_left () mp 1
84.
85. mesh/adapt/manual-refinement-criteria "refine" manual-coarsening-criteria "coarsen" adapt-
mesh
86. solve/patch vap fluid () () mp 0
87. solve/patch vap () bubble_left () mp 1
```

```
 88.
 89. mesh/adapt/set maximum-refinement-level 4
 90. mesh/adapt/manual-refinement-criteria "refine" manual-coarsening-criteria "coarsen" adapt-
mesh
 91. mesh/adapt/set maximum-refinement-level 3
 92. solve/patch vap fluid () () mp 0
 93. solve/patch vap () bubble_left () mp 1
 94.
 95. solve/patch mixture () bubble_left () temperature 373.2
 96. solve/patch mixture () bubble_left () x-velocity cancel 0.0234
 97.
 98. file/auto-save/data-frequency 1000 case-frequency each-time append-file-name-with flow-time
6
 99.
100. ;turn off outputs
101. /solve/monitors/residual plot n print n
102.
```

2. SIMULATION EXECUTION JOURNAL SCRIPT (CASE 5 IN SECTION 5)

```
; Compile and load the UDF "udf_w-0-15-225.c"
/define/user-defined/compiled-functions compile libudf y udf_w-0-15-225.c "" ""
/define/user-defined/compiled-functions load libudf

; Create 10 scalars and assign scalar 2 & 4
/define/user-defined/user-defined-scalars 10 y n mixture y "mass flow rate" "default" mixture y "mass flow rate" "default" mixture y "none" "mass_source::libudf" mixture y "mass flow rate" "default" mixture y "none" "mesh_refine::libudf" mixture y "mass flow rate" "default" mixture y "mass flow rate" "default" mixture y "mass flow rate" "default" mixture y "mass flow rate" "default"

; Hook the adjust functions from the udf
/solve/set/equations flow n mp n temperature n uds-0 n uds-1 n uds-2 n uds-3 n uds-4 n uds-5 n uds-6 n uds-7 n uds-8 n uds-9 n
/define/user-defined/function-hooks adjust "adjust_gradient::libudf" ""
/solve/set/time-step 1e-12
/solve dti 1 1
/define/user-defined/function-hooks adjust "adjust_gradient::libudf" "in_s_term::libudf" ""
/solve dti 1 1
/define/user-defined/function-hooks adjust "adjust_gradient::libudf" "in_s_term::libudf" "diffuse::libudf" ""
/solve dti 1 1
/define/user-defined/function-hooks adjust "adjust_gradient::libudf" "in_s_term::libudf" "diffuse::libudf" "norm_fct::libudf" ""
/solve dti 1 1

; Add the automatic mesh refinement and update the material properties for the refinement
/mesh/adapt/manage-criteria/add "adaption_criteria_0" frequency 5 q
/solve/set/equations flow n mp n temperature n uds-0 n uds-1 n uds-2 n uds-3 n uds-4 y uds-5 n uds-6 n uds-7 n uds-8 n uds-9 n
/define/materials/change-create water-liq water-liq n n n n n n n n y defined-per-uds 2 constant 1.916498 4 constant 1.916498 -1 n
/define/materials/change-create water-vap water-vap n n n n n n n n y defined-per-uds 2 constant 0.0012021 4 constant 0.0012021 -1 n
/solve dti 1 10
; Finally, create the animations, turn on energy, flow, volume fraction and uds-4 equations. Run the adaptive simulation for total 4.5ms
/solve/animate/objects/create animation-1 animate-on vof frequency 500 storage-dir "Insert your storage directory (C:\Users\Documents..)" q
/solve/set/equations flow y mp y temperature y uds-0 n uds-1 n uds-2 y uds-3 n uds-4 y uds-5 n uds-6 n uds-7 n uds-8 n uds-9 n
/define/boundary-conditions/fluid fluid liq y 1 n y liq_src::libudf n n 0 n 0 n n
/define/boundary-conditions/fluid fluid vap y 1 n y vap_src::libudf n n 0 n 0 n n
/define/boundary-conditions/fluid fluid mixture y 0 0 1 n y enrg_src::libudf 0 0 0 0 0 0 0 0 0 n n n 0 n 0 n n n
/solve/monitors/residual/convergence-criteria 1e-04 1e-04 1e-04 1e-06 1e-04 1e-04 1e-04
/solve time-step 2e-07
/solve dti 20 40

/solve time-step 2e-07
/solve dti 120000 20

/parallel/timer/usage
/file/write-case-data/Users/Documents../Test128_fin.cas.h5
/exit y

```